Electron Scattering and Static Field Effects in High-order Harmonic Generation in Solid Systems

Dissertation
zur Erlangung des Doktorgrades
an der Fakultät für Mathematik, Informatik und Naturwissenschaften
Fachbereich Physik
der Universität Hamburg

vorgelegt von
Chang-Ming Wang

Hamburg
2021

Gutachter/innen der Dissertation:	Prof. Dr. Angel Rubio
	Prof. Dr. Nina Rohringer
Zusammensetzung der Prüfungskommission:	Prof. Dr. Angel Rubio
	Prof. Dr. Nina Rohringer
	Prof. Dr. Michael Potthoff
	Prof. Dr. Nils Huse
	Prof. Dr. Shunsuke Sato
Vorsitzender der Prüfungskommission:	Prof. Dr. Michael Potthoff
Datum der Disputation:	29.09.2021
Vorsitzender Fach-Promotionsausschusses PHYSIK:	Prof. Dr. Wolfgang Hansen
Leiter des Fachbereichs PHYSIK:	Prof. Dr. Günter Hans Walter Sigl
Dekan der Fakultät MIN:	Prof. Dr. Heinrich Graener

Abstract

The strong non-linear light emission induced by a high-intensity laser in solid systems has become a research topic of immense interest over the last few years. Under such a strong laser, electrons from the material will generate photons with energy being integer multiple of that of the input laser photon. This specific light emission process is addressed as high-order harmonic generation (HHG) and has been widely studied in systems of atomic or molecular gas. With the great understanding of the mechanisms of the photon emission process, several powerful applications based on the gas-phase HHG are developed, enabling the generation of isolated short pulses [1], atomic or molecular orbital tomography [2], and real-time observation of electron dynamics [3]. Recently HHG has also been observed in solid systems using a semiconductor as a target. Considering many useful applications utilizing HHG from gas systems have been developed and widely utilized in various scientific fields, adaptation of the applications based on gas-phase HHG to the realm of solid-phase HHG has been pursued by many researchers. Whether the adaptation could be carried out highly depends on what physicists know about solid-phase HHG. As a result, a deep understanding of the dynamics and development of theoretical models are highly demanded in the community of solid-phase HHG.

In this thesis we investigate solid-phase HHG under the influence of electron scattering or an additional static field in an attempt to achieve a better understanding of the underline dynamics. For the studies of electron scattering, we integrate Umklapp scattering into the generalized three-step model [4, 5] and compare the results from this modified model with those from *ab initio* quantum simulations. This leads to our publication [6] showing that in HHG power spectra each of the multi-plateau, which originates from the band climbing [7], is dominated by the light emission from electron-hole pairs experiencing a specific number of scattering; An electron-hole pair with zero, one, and two scattering before emitting a photon mainly contributes to the first, second, and third plateaus of an HHG power spectrum, respectively. In addition, we also consider another simple modification to the generalized three-step model for treating general scattering effects in solids based on a mean-free-path approach. We find that such a simple modification could reproduce the wavelength independence of cutoff energy for solid-phase HHG, suggesting such behavior is directly related to scattering processes in solids. As for the studies on the effect of an additional static field, we add a static electric field on top of a driving laser for HHG based on a simple two-band parabolic quantum model. The

resulting HHG power spectra yield an overall lower emission intensity and static-field-dependent cutoff energy. When increasing the static field from zero, the cutoff energy will increase, reach a maximum, and then decrease to the band gap when the static field becomes as strong as the oscillating driving laser. This static-field-dependence of the cutoff energy could be described by the two competing mechanisms induced by a static field: reduced probability for overall electron-hole recombination and increased chances for recombination for some high-energy electron-hole pairs when the static field happens to align with the driving laser pushing the pairs together.

In addition to the studies on dynamics of solid-phase HHG, we also present a preliminary investigation of the core electron absorption for bulk aluminum under X-ray by time-dependent density functional theory (TDDFT). The aim was to verify whether the underline theoretical model could capture the well-known absorption saturation in aluminum [8] so as to estimate the applicability of the simulation framework for solid-phase HHG driven by X-ray pulses. From our simulations, the absorption saturation is indeed reproduced qualitatively. This suggests the first step of solid-phase HHG in the three-step model, namely the excitation of electrons, could be captured by *ab initio* simulations based on TDDFT.

Abstraktum

Die starke nichtlineare Lichtemission eines hochintensiven Lasers in Festkörpersystemen ist in den letzten Jahren zu einem Forschungsthema von immensem Interesse geworden. Unter einem so starken Laser erzeugen Elektronen aus dem Material Photonen mit einer Energie, die ein ganzzahliges Vielfaches der des eingegebenen Laserphotons ist. Dieser spezifische Lichtemissionsprozess wird als harmonische Erzeugung hoher Ordnung (HHG) bezeichnet und wurde in Systemen aus atomaren oder molekularen Gasen umfassend untersucht. Mit dem großen Verständnis der Mechanismen des Photonenemissionsprozesses werden mehrere leistungsstarke Anwendungen basierend auf dem HHG in der Gasphase entwickelt, die die Erzeugung isolierter kurzer Pulse [1], Atom- oder Molekülorbitaltomographie [2] und Echtzeitbeobachtung der Elektronendynamik [3]. Kürzlich wurde HHG auch in festen Systemen mit einem Halbleiter als Target beobachtet. In Anbetracht vieler nützlicher Anwendungen, die HHG aus Gassystemen verwenden, wurden entwickelt und auf verschiedenen wissenschaftlichen Gebieten weit verbreitet verwendet, eine Anpassung der Anwendungen basierend auf Gasphasen-HHG an den Bereich von Festphasen-HHG wurde von vielen Forschern verfolgt. Ob die Anpassung durchgeführt werden könnte, hängt stark davon ab, was Physiker über Festphasen-HHG wissen. Aus diesem Grund sind in der Gemeinschaft der Festphasen-HHG ein tiefes Verständnis der Dynamik und Entwicklung theoretischer Modelle sehr gefragt.

In dieser Arbeit werden wir Festphasen-HHG unter dem Einfluss von Elektronenstreuung oder einem zusätzlichen statischen Feld untersuchen, um ein besseres Verständnis der Unterstreichungsdynamik zu erreichen. Für die Untersuchungen der Elektronenstreuung integrieren wir die Umklapp-Streuung in das verallgemeinerte dreistufige Modell [4, 5] und vergleichen die Ergebnisse dieses modifizierten Modells mit denen eines *ab initio* Quantensimulationen. Dies führt zu unserer Publikation [6], die zeigt, dass in HHG-Leistungsspektren jedes der Multiplateaus, die aus dem Bandanstieg stammen, [7] , wird von der Lichtemission von Elektron-Loch-Paaren dominiert, die eine bestimmte Anzahl von Streuungen erfahren; Ein Elektron-Loch-Paar mit einer Streuung von Null, Eins und Zwei vor der Emission eines Photons trägt hauptsächlich zum ersten, zweiten und dritten Plateau eines HHG-Leistungsspektrums bei. Darüber hinaus betrachten wir eine weitere einfache Modifikation des verallgemeinerten dreistufigen Modells zur Behandlung allgemeiner Streueffekte in Festkörpern auf der Grundlage eines Mean-Free-Path-Ansatzes. Wir stellen fest, dass eine solch einfache Modifikation

die Wellenlängenunabhängigkeit der Abschaltenergie für Festphasen-HHG reproduzieren könnte, was darauf hindeutet, dass ein solches Verhalten direkt mit der Streuung in Festkörpern zusammenhängt. Für die Studien zur Wirkung eines zusätzlichen statischen Feldes fügen wir ein statisches elektrisches Feld über einem treibenden Laser für HHG hinzu, basierend auf einem einfachen parabolischen Zwei-Band-Quantenmodell. Die resultierenden HHG-Leistungsspektren ergeben eine insgesamt geringere Emissionsintensität und statikfeldabhängige Abschaltenergie. Wenn ein statisches Feld von Null erhöht wird, steigt die Abschaltenergie an, erreicht ein Maximum und nimmt dann bis zur Bandlücke ab, wenn das statische Feld so stark wird wie der oszillierende Antriebslaser. Diese statische Feldabhängigkeit der Abschaltenergie könnte durch die beiden konkurrierenden Mechanismen beschrieben werden, die durch ein statisches Feld induziert werden: verringerte Wahrscheinlichkeit für die gesamte Elektron-Loch-Rekombination und erhöhte Chancen für die Rekombination für einige hochenergetische Elektron-Loch-Paare im statischen Feld richtet sich zufällig mit dem treibenden Laser aus und drückt die Paare zusammen.

Zusätzlich zu den Untersuchungen zur Dynamik von Festphasen-HHG präsentieren wir hier auch eine vorläufige Untersuchung der Kernelektronenabsorption für Aluminium in großen Mengen unter Röntgenstrahlung mittels time-dependent density functional theory (TDDFT). Ziel ist es hier zu überprüfen, ob das unterstrichene theoretische Modell die bekannte Absorptionssättigung in Aluminium erfassen kann [8], um die Anwendbarkeit des Simulationsgerüsts für durch Röntgenpulse angetriebenes Festphasen-HHG abzuschätzen. Aus unseren Simulationen geht hervor, dass die Absorptionssättigung tatsächlich reproduziert wird. Dies legt nahe, dass der erste Schritt von Festphasen-HHG im dreistufigen Modell, nämlich die Anregung von Elektronen, durch auf TDDFT basierende *ab initio* -Simulationen erfasst werden könnte.

Contents

List of Figures viii

List of Abbreviations xiii

List of Publications xiv

1 Introduction 1
- 1.1 High-order Harmonic Generation . . . 2
- 1.2 The Roles of Scattering and Static Field in HHG . . . 8
- 1.3 Light Absorption of Core Electrons . . . 11
- 1.4 Purposes and Conclusions of this Thesis . . . 12
- 1.5 Structure of the Thesis . . . 13

2 Theoretical Models for the Quantum Systems 15
- 2.1 Quantum Model . . . 16
  - 2.1.1 Hamiltonian and the Ground State . . . 16
  - 2.1.2 Time Propagation and HHG Power Spectrum . . . 18
  - 2.1.3 Time-Frequency Analysis . . . 19
  - 2.1.4 Numerical Implementation . . . 20
- 2.2 The Parabolic Two-Band Model . . . 23
  - 2.2.1 The Dynamical Equation and Approximations . . . 23

3 Semi-Classical Models and Umklapp Scattering 28
- 3.1 Semi-classical Model for the HHG in Gases and Solids . . . 29
- 3.2 Semi-classical Model with Umklapp Scattering . . . 32
  - 3.2.1 Implementation of the Model with Umklapp Scattering . . . 35

4 The Effects of Scattering and a Static Field on the HHG in Solids 38
- 4.1 The Effect of Umklapp Scattering on Solid HHG . . . 39
  - 4.1.1 Setup of the Quantum System under a Model Potential . . . 39
  - 4.1.2 The Cutoff Energy Dependence in the Semi-classical Models . . . 40
  - 4.1.3 The HHG Spectrum from Quantum Simulations . . . 43
  - 4.1.4 Time-frequency Analysis . . . 45
  - 4.1.5 Extension to General Scattering Effects in Solids . . . 50

4.2 The Effect of a Static Electric Field on Solid HHG 53
4.2.1 Setup of the Parabolic Two-band System 53
4.2.2 The HHG Spectrum under a Static Field 53
4.2.3 Splitting of the Cutoff by the Broken Symmetry 56

5 Light Absorption of Core Electrons 62
5.1 Saturable Absorption in Aluminum and its Mechanism 63
5.2 Theoretical Framework 64
5.2.1 Time-dependent Density Functional Theory 66
5.2.2 Calculation of Transmission 67
5.3 Absorption of Core Electrons 68
5.3.1 Saturable Absorption 68
5.3.2 Corrections to Transmission from Theoretical Calculation 71

6 Conclusion and Outlook 75

A Proof of the Equation 80

Bibliography 83

Code References 89

Acknowledgments 90

Declaration on Oath 92

List of Figures

1.1 (a) A typical power spectrum for gas-phase HHG and (b) a schematic illustration of the three-step model. In (a), the spectrum shows several strong peaks in the low-energy region. In the high-energy region there are many weaker peaks with similar intensity, forming a plateau-like structure. The emission intensity drops quickly after a threshold defined as cutoff energy. In (b), the first, second, and third steps are marked by the process I, II, and III, respectively. The dark-blue circle describes a bounded electron and the light-blue one describes an energetic electron. The red curves represent the potential energy from the ion core and the laser. The orange sinusoidal curve is an analogy of a emitted photon. . . 3

1.2 A schematic illustration for the HHG in gas (left) and solid (right) systems. The three steps for the two kind of HHG are marked by the procedure I, II, and II with different colors (red for gas and blue for solid). The energy diagram in the middle merges two kinds of energy dispersion of the gas and solid systems into one band structure. For the gas system, the energy of an atomic orbital is denoted by a horizontal line and that of the continuum is described by the parabola. For the solid system, the energy of the conduction band and the valence band are described by the parabola and inverse parabola, respectively. 6

1.3 Possible scattering of charged particles with ions. The trajectories of an electron(red curve) and a hole(blue curve) may pass ions (gray circles) several times and therefore scattering of the electron and hole with the lattice is generally expected. The trajectories shown in the figure ignore scattering and the electron and hole successfully recombine to emit a photon (orange sinusoidal curve). However, if the scattering is considered, the blue and red trajectory will change when making contact with the ions, the recombination of this electron-hole pair and the corresponding emission of a photon would become very unlikely. This indicates HHG could be altered by scattering between charged particles and the lattice. 7

1.4 A comparison for the second step of the generalized three-step model and generalized three-step model with Umklapp scattering (our model) in crystal-momentum space. The energy bands are depicted as black curves. The red- and blue-dotted arrows describe the non-scattered and scattered paths, respectively. The left-hand side of the figure shows how the generalized three-step model treats an electron moving through a scattering point (the point where the bands cross) in the crystal-momentum space: the electron moves through a scattering point as if the neighboring band does not exist and ignores any chance to move to the neighboring band. On the other hand, the right-hand side of the figure shows that the trajectory where the electron remains in the same band (non-scattered path) and the trajectory where the electron moves to the neighboring band (scattered path) are both taken into account in our model. 9

2.1 Some examples of numerical calculations for HHG in a solid system based on the one-dimensional quantum model introduced in this section. The electric field of an applied laser as a function of time is described in (a). The current density generated from the system as a response to the applied laser field shown in (a) is also described in (b) as a function of time. The HHG power spectrum calculated from the current density in (b) is shown in (c). 19

2.2 An example for the time-frequency analysis. The spectrum of the current density from the short-time Fourier transformation is shown as the color map in the background, and the emission timing and energy from a semi-classical model is marked by black circles. 21

3.1 A schematic illustration for the generalized three-step model. The blue and red curves describe a valence band and a conduction band. The steps of excitation, acceleration, and recombination are marked by I, II and III, respectively. 31

3.2 A sketch for the two possible paths for an electron which undergoes Umklapp scattering in the crystal-momentum space. The process I indicates an electron moving towards the scattering point located at zone boundary. The process II and II' describe the non-scattered and scattered paths, respectively. 34

4.1 (a) Electronic band structure of the one-dimensional model with the lattice potential described in Eq. 4.1 is shown. The valence bands and conduction bands are described by the blue-solid lines and the red-dotted lines, respectively. (b) Comparison of the electron-hole band (red-solid lines) and the Kane's band (blue-dotted lines). This figure is taken directly from our publication [6]. 41

4.2 Cutoff energy U_c calculated from the generalized three-step model versus the square root of ponderomotive energy $U_p^{\frac{1}{2}}$. Both of the energy is normalized with respect to the band gap. The semi-classical predictions for the parabolic band and the Kane's band are shown as green-dashed line and red-solid line, respectively. The analytical expression for the strong-field approximation, $U_c/\epsilon_g = 3(U_p/\epsilon_g)^{1/2}$, is described as the blue-dotted line. This figure is taken from our publication [6]. 42
4.3 The power spectrum of HHGs from quantum simulations with the electric field amplitude $F_0 = 0.165$ V/Å. Several plateaus are visible and their corresponding cutoff energy is marked by black arrows around 13, 28, 44, and 68 eV. This figure is taken from our publication [6]. 44
4.4 The color map shows the calculated high-order harmonic generation (HHG) power spectra from the one-dimensional quantum simulations versus the electric field amplitude F_0 of the laser. The cutoff energy computed by our semi-classical model using the Kane's band is described as different lines: The cutoff from trajectories without scattering is shown as the black-solid line. The cutoff from trajectories with single scattering is described as the blue-dashed line. The cutoff from trajectories with double scattering is shown by the red-dotted line. This figure is taken from our publication [6]. 46
4.5 Time-frequency analysis of the HHG calculated from quantum simulations are shown as the color map. The emission energy and timing predicted from the generalized three-step model with Umklapp scattering are represented as black dots, and their contribution for no scattering, single scattering, and double scattering are indicated in panel (a), (b), and (c) respectively. This figure is taken from our publication [6]. 47
4.6 The comparison for semi-classical predictions for recombination occurring (a) at zero separation distance and (b) within a separation distance of 40 a.u. between an electron and a hole. The purple circles describe the semi-classical predictions and the color map describes the time-frequency analysis of HHG. The setup for quantum simulations is the same as Fig. 4.5. 49
4.7 The comparison for semi-classical predictions for excitation occurring (a) at exactly Γ point and (b) in a region within 0.1 a.u. from Γ point. The purple circles describe the semi-classical predictions and the color map describes the time-frequency analysis of HHG. The setup for quantum simulations is the same as Fig. 4.5. 50
4.8 Wavelength dependence of the cutoff energy of HHG from the generalized three-step model with general scattering effects. The cutoff energy with l_{MFP} equal to 3, 5, and 7 nm are described as red-dashed, green-dotted, and blue-dashed-and-dotted lines. The result without scattering is also depicted as the black-solid line. The wavelength independence can be clearly observed in cases with finite l_{MFP}. This figure is taken from our publication [6]. 52

4.9 The power spectra of HHGs under an additional static electric field, with various colors indicating different static field strength. The blue, light-blue, pink, red, and brown lines are results with the static electric field E_s being 0.04, 0.08, 0.12, 0.16, and 0.20 V/Å, respectively. Also, the power spectrum of HHGs without an additional static field is represented as the black line. . . . 54

4.10 The time-frequency analysis of HHG (color map) and its semi-classical prediction(pink circles) with the electric field amplitude of the oscillatory laser $E_0 = 0.4$ V/Å and the electric field amplitude of the static field $E_s = 0.12$ V/Å. . . . 55

4.11 The power spectrum of the HHG as a function of the electric field amplitude of the static field E_s is shown as the color map. The observed upper and lower cutoffs from the semi-classical model are both shown as purple lines. Moreover, the band gap energy of the system $E_g = 9$ eV is denoted by the black-dotted line. . . . 56

4.12 The energy gained by electron-hole pairs at recombination as a function of return time is shown. The results with the static electric field amplitude E_s being 0, 0.1, and 0.2 V/Å are described as black-, red-, and blue-circle curves, respectively. One can clearly observe the gained energy for the case without a static field splits from one curve to two curves when E_s is increased. . . . 58

4.13 The cutoff energy predicted by the generalized three-step model as a function of the electric field strength ratio E_s/E_0 with $E_0 = 0.4$ V/Å. The upper and lower cutoffs are designated by the red and the blue lines. The band gap energy $E_g = 9$ eV is also shown for reference as black-dashed line. . . . 59

5.1 A schematic view for the mechanism of saturable absorption under a soft X-ray in aluminum. The conduction band is represented by a parabola and the core energy level for 2p orbitals is described by a flat line. Also, an incoming X-ray photon is depicted by the yellow lightning. The energy bands (a) before and (b) after excitation of core electrons are shown in the upper section. In (a) the positive core ion is electronically shielded by core electrons. In (b), the electronic shielding of the core ion is attenuated since some core electrons are excited, and the energy bands are now bounded more tightly, which is indicated by the energy shift of the bands. The interaction between photon and a core electron (c) before and (d) after the bands are shifted is also described in the lower section. (c) Before the energy shift, core electrons can absorb the soft X-ray photon and be excited to the Fermi surface. (d) After the energy shift, the photon energy of the soft X-ray is not large enough to make the excitation possible. . . 65

5.2 Comparison of the transmission as a function of laser fluence between our theoretical calculation (blue curve) and the experimental data (purple curve) taken from the study [8]. Note that, since only the laser intensity is altered in the pulse and the laser fluence is proportional to the intensity, the axis of fluence can be seen as the axis of intensity. 68
5.3 The absorption spectrum of aluminum near the $\mathrm{L}_{\mathrm{II,III}}$ absorption edge from theoretical calculation (red curve) and experimental data (blue curve) taken from the previous study [58]. The vector potential of the soft X-ray used in this chapter is also shown as a sharp yellow peak to illustrate its position in the absorption spectrum. The full-width at half-maximum (FWHM) of the laser is around 0.27 eV. Additionally, we also mark the energy difference of 19 eV between the absorption edge and the laser in the case of our simulation and the experiment. We select a soft X-ray with photon energy of 85.5 eV instead of 92 eV used in the experiment because it has the same distance from the edge in the absorption spectrum. 69
5.4 The decrease in energy as a function of fluence for the core level (blue curve) and a conduction band (red curve) compared to their original energy in the ground state. The arrow indicates the fluence around 5 $\mathrm{J/cm^2}$ where the core level has huge energy shift. Note that at this large energy shift in the core level the energy shift in the conduction band is negligible. This makes the photon energy of the soft X-ray off-resonance and thereby saturable absorption occurs. 70
5.5 Transmission as a function of laser fluence from theoretical calculation for the case with focal-spot average (red curve) and the case without focal-spot average (blue curve). Transmission from the experimental data is also shown as the purple curve for comparison. 72
5.6 Transmission as a function of laser fluence from theoretical calculation for the case with surface oxidation (red curve) and the case without surface oxidation (blue curve). Transmission from the experimental data is also shown as the purple curve for comparison. 73

List of Abbreviations

HHG high-order harmonic generation

TDDFT time-dependent density-functional theory

FWHM full-width at half-maximum

FEL free-electron laser

List of Publications

Chang-Ming Wang, Nicolas Tancogne-Dejean, Massimo Altarelli, Angel Rubio, and Shunsuke A. Sato,
Role of electron scattering on the high-order harmonic generation from solids, [6],
Physical Review Research, **2**, 033333 (2020)

Chapter 1

Introduction

Light enables us to see material world. Through light humans perceive and understand the world around us. At home, we see scenes via a window from the light transmitted through the material glass. In gatherings, we identify our friends by the light reflected from their faces. On a train, we read the information on a cell phone by the light radiated from the electronic screen. It is through light-matter interaction that we humans come to know the world. This concept is no exception in the realm of science, either. The very fundamental of scientific research is typically composed of four key steps: (1) observation of a phenomenon, (2) making a hypothesis to describe the observation, (3) verifying and reformulating the hypothesis to build up a theory, and (4) making predictions based on the theory. The very first step of all science, namely to see a phenomenon, is typically carried out by light-matter interaction. That is, scientists use light as a probe to see specific phenomena of interest. As a result, it is very important to understand the light-matter interaction so as to identify what are actually seen in the observation. And thereby one could establish solid ground truth for the following scientific investigation to carry on. This is the reason why optical and electron spectroscopy are among the most experimentally and theoretically studied topics, and many questions in the fields are still waiting to be answered.

For a long time, physicists had set up a framework to describe light-matter interaction based on perturbation theory. In linear optics, the response of a dielectric material to light is simply formulated by electric permittivity. That is, the polarization of the material induced by the light is merely proportional to the electric field of the light by a scaling constant. To go beyond that, physicists also consider non-linear optics where the induced polarization is further expanded to some higher-order function of the electric field of the light. In either linear and non-linear optics, the light-matter interaction is always treated in the sense of a small perturbation: the influence of the light on the materials is assumed to be tiny. To be more precise, it is taken as given the electric field or intensity of the light is small compared to the electric field binding the electrons in the materials. Generally speaking, this is indeed true in many cases then and the light-matter interaction is well understood and described by linear and non-linear optics. Nevertheless, such a successful perturbative approach eventually has to be revised and reconsidered when the first laser was created in 1960 [9, 10]. Unlike typical light, a laser is characterized by its narrow bandwidth and strong intensity, which renders in many cases the perturbative approach to light-matter interaction in linear and non-linear optics inapplicable. At the same time, with lasers being widely harnessed into experiments after its creation, many novel phenomena are observed and proposals for new applications are advocated. Because of these new observations and promising utilities, a new theory to describe the light-matter interaction is in great need in many scientific fields. One of the very interesting new subjects enabled by the creation of lasers in strong-field physics is the high-order harmonic generation (HHG).

1.1 High-order Harmonic Generation

HHG is a photon up-conversion process at extreme occurring in a material when a sufficiently strong laser is applied. It is characterized by that the photon energy of the generated light is integer multiples, namely harmonics, of that of the input laser shining on the specimen. When such generated light is received by a detector and the intensity of different energy, or harmonics, is measured, it typically yields a power spectrum featuring strong peaks in the low-energy region and many weaker peaks with roughly equal intensity in the high-energy region, followed by a sharp drop in intensity at certain threshold energy (see Fig. 1.1 (a)). The region with weak peaks of similar intensity in the power spectrum is generally called the plateau of the spectrum and the end of this plateau the cutoff. The energy marking the cutoff is denoted as the cutoff energy and is a crucial property of a power spectrum of harmonic generations. People use the term HHG simply to indicate the high-energy photon emissions in the plateau region since they are of high interest in most of the cases. Such HHG was first observed in 1987 using rare gases as target specimens [11].

HHG involves light-matter interaction beyond the description of linear or perturbative non-linear optics due to the strong nonlinearity induced by the large intensity of the laser, and thereby several different approaches are proposed to describe how electrons in the target, typically gas molecules in a chamber at the time, respond to the strong laser. One of the most successful models describing the dynamics of the HHG using gas targets is the so-called three-step model [12, 13]. In this semi-classical model the whole process of the HHG is explained by three distinctive steps: (1) An electron is ionized by the strong laser and escapes from its mother molecule. (2) The strong laser pushes the electron away from the ionized molecule and supplies it with energy. (3) When the electron is pushed back to the ionized mother molecule due to the oscillatory force of the laser, it recombines with the molecule and releases the extra kinetic energy gained during the second step by emitting a high-energy photon. These three steps are illustrated in Fig. 1.1 (b) as the process I, II, and II. This insightful semi-classical model provides an extremely simple physical picture for the HHG in gas while at the same time making several successful predictions on some important properties of a HHG power spectrum for atomic and molecular systems. For example, the cutoff energy of the spectrum could be estimated by the three-step model and its parabolic dependence on the electric field

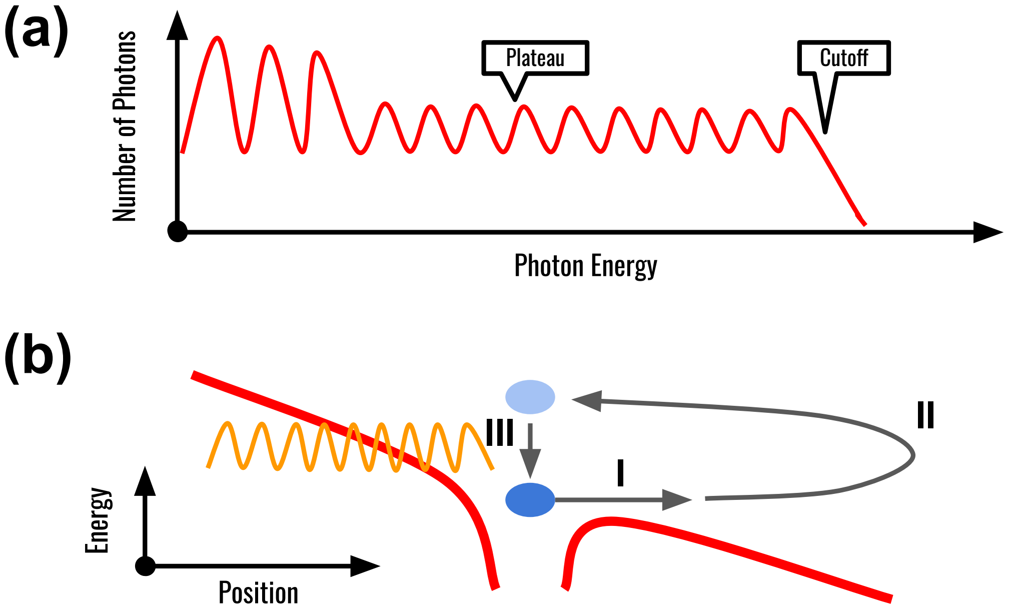

Figure 1.1: (a) A typical power spectrum for gas-phase HHG and (b) a schematic illustration of the three-step model. In (a), the spectrum shows several strong peaks in the low-energy region. In the high-energy region there are many weaker peaks with similar intensity, forming a plateau-like structure. The emission intensity drops quickly after a threshold defined as cutoff energy. In (b), the first, second, and third steps are marked by the process I, II, and III, respectively. The dark-blue circle describes a bounded electron and the light-blue one describes an energetic electron. The red curves represent the potential energy from the ion core and the laser. The orange sinusoidal curve is an analogy of a emitted photon.

amplitude of the driving laser could also be retrieved from the model.

The understanding of the dynamics of the HHG brings forward several powerful applications based on these emitted high-energy photons. One of the most important applications for the HHG is the creation of ultra-short pulses [14, 15, 16]. Physicists have been utilizing the HHG photons from the plateau region to generate pulses with subfemtosecond duration [1, 17], which is a typical time scale for the motion of electrons. This means one could use the ultra-short pulse synthesized from the HHG to observe electron motion in time and enhance our understanding of the corresponding processes. In practice, by utilizing ultra-short pulses researchers could perform real-time observation on electron transitions between atomic orbitals and electron tunneling through an atomic potential barrier with subfemtosecond temporal resolution [3, 18]. In addition, similar techniques are also applied to reconstruct the highest-occupied molecular orbitals to understand the chemical properties of the molecules, and observe the attosecond dynamics of these orbitals, enabling the inspection of chemical reactions [2]. In short, the HHG from gas systems has become a new source of light and a deep understanding of its dynamics has enabled us to create ultra-short pulses from the HHG, which acts as a new light probe for matters and phenomena. With the gas-phase HHG the idea of ”seeing the matter through light” has advanced to a whole new level - into the world of electrons. Physicists now can utilize light beyond the description of linear or non-linear optics to see the material world in the natural length and time scale of an electron.

The development of HHG is not limited to gas systems but advances to the world of condensed matters. In 2011 HHG from solid systems was discovered and this solid-phase HHG is observed to possess some similar properties like the gas-phase HHG [19, 20, 21]. For the radiation power spectrum, the solid-phase HHG also starts with high-intensity radiation peaks in the low-order region, follows a plateau region where peaks have lower and overall similar intensity, and then ends up at the cutoff energy. Likewise, the intensity of the solid-phase HHG cannot be described by perturbative non-linear optics. Considering the similarities, physicists have also been attempting to adapt techniques and applications for HHG from gas systems to solid systems. A successful extension would expand the field of strong-field physics and attosecond science into solid systems [22]. For instance, if the same technique for real-time observation of electronic transitions could be applied in solid systems, one would be able to obtain the dynamical involvement of each electronic bands and improve the understanding of the quantum interference between each excitation channel. In addition, the real-time observation of the HHG process in a solid system may also allow us to understand the role of other complicate mechanisms like scattering, which is actually one of the mechanisms we have studied in this thesis, in the making of solid-phase HHG. On the other hand, despite their similarity in radiation spectra for gas- and solid-phase HHG, there are indeed several key differences between the two systems. In gas systems, the cutoff energy of a power spectrum has a quadratic dependence on the electric field amplitude of the laser while in solid systems it has linear dependence. Not only that, the cutoff energy in solid systems appears to be independent of the wavelength of the laser instead of inverse quadratic dependence in gas systems. Besides, unlike single plateau in a gas-phase HHG spectrum, some theoretical simulations for solid-phase HHG show several plateau [23, 24, 25, 7], and a second plateau is observed in experiments using solids formed from rare gases [26]. Moreover, in most gas-phase HHG only electrons in the highest-occupied shell take part in the dynamics of photon emissions, while in solid-phase HHG the electrons lying in top-few valence bands could affect the radiation indirectly through quantum interference, leading to unconventional behavior like cancellation of radiation for certain polarization direction of the driving field [27]. All of these interesting properties and great prospects for applications call for the microscopic understanding of underlying dynamics and establishing a new model or theory for HHG from solid systems.

Several theoretical approaches have been proposed to describe and reproduce solid-phase HHG. Direct *ab initio* simulations using modeled crystal potentials reasonably capture the general structure of the HHG power spectra from solid systems [5, 23, 24]. Also, by performing *ab initio* simulations based on semiconductor Bloch equations [28, 29], one could obtain HHG power spectra directly comparable to experiments [30]. Besides reproducing numerical results with experiments, many simple semi-classical models are also proposed to describe the key essence of the dynamics. One of the very important models for solid-phase HHG is the three-step model generalized from gas systems. This generalized three-step model substitutes the parabolic energy dispersion in gas systems with complex band structures in solid systems [4, 5]. In this model, the solid-phase HHG is characterized by the following three steps: (1) An electron is excited from the top of the top valence band to the bottom of the lowest conduction band, creating an electron-hole pair. (2) The created electron and hole are pushed by the external laser force and move in the conduction band and the valence band, respectively. (3) When the electron and the hole meet each other in real space, they recombine and emit a photon with energy equal to the energy difference between the conduction band and the valence band where they locate at that moment. A direct comparison of this generalized three-step model for solid-phase HHG and the original three-step model for gas-phase HHG is shown in Fig. 1.2. Although this generalized three-step model is limited to certain band structure of solid systems and intensity of the input laser, it does provide a simple description for the dynamics of HHG and connects the idea of HHG from gas and solid systems by a mere difference in the energy dispersion excited charged particles follow [31].

Despite the simple picture of solid-phase HHG by the generalized three-step model, the model still bears some non-intuitive assumptions that need to be revisited, quantified, and understood in details when one takes a closer look. Note that, within this semi-classical model the created electrons and holes are assumed to be effectively-free particles in the sense of effective mass. That is, they possess time-dependent effective mass and are only subjected to the force of the external laser. Such an assumption is suitable in the case of gas-phase HHG as the separation between an ionized electron and its parent ion is extremely large. So, the attractive force from the ion acting on a ionized electron could be neglected. However, in solids created electrons and holes are expected to still reside in the crystal and surrounded by a sea of positively-charged ions. In this situation, interaction with ions, like scattering between the charged particles and ions,

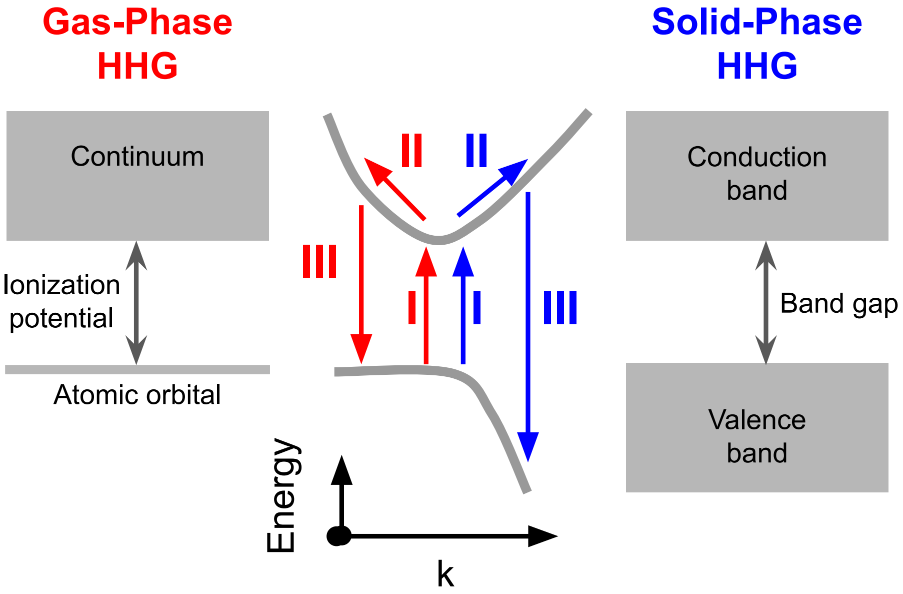
Gas-Phase
HHG
Continuum
Ionization
potential
Atomic orbital
II
II
III
I
I
III
Energy
k
Solid-Phase
HHG
Conduction
band
Band gap
Valence
band

Figure 1.2: A schematic illustration for the HHG in gas (left) and solid (right) systems. The three steps for the two kind of HHG are marked by the procedure I, II, and II with different colors (red for gas and blue for solid). The energy diagram in the middle merges two kinds of energy dispersion of the gas and solid systems into one band structure. For the gas system, the energy of an atomic orbital is denoted by a horizontal line and that of the continuum is described by the parabola. For the solid system, the energy of the conduction band and the valence band are described by the parabola and inverse parabola, respectively.

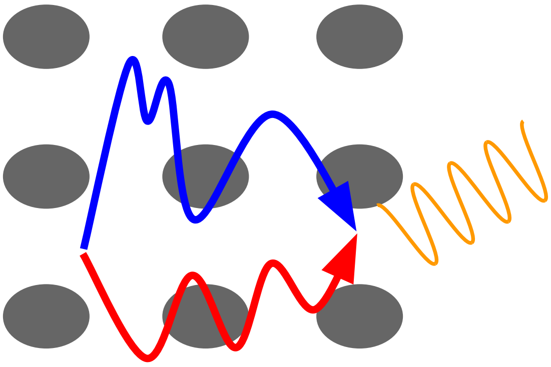

Figure 1.3: Possible scattering of charged particles with ions. The trajectories of an electron(red curve) and a hole(blue curve) may pass ions (gray circles) several times and therefore scattering of the electron and hole with the lattice is generally expected. The trajectories shown in the figure ignore scattering and the electron and hole successfully recombine to emit a photon (orange sinusoidal curve). However, if the scattering is considered, the blue and red trajectory will change when making contact with the ions, the recombination of this electron-hole pair and the corresponding emission of a photon would become very unlikely. This indicates HHG could be altered by scattering between charged particles and the lattice.

could be expected in general (see Fig. 1.3). As trajectories of electrons and holes in the second step will very likely be modified, the chances of recombination between them could become questionable. As a consequence, the corresponding photon emission and HHG might also be altered by the scattering. In addition, one would anticipate not just one but many scattering events when an electron or a hole is propagating in the lattice, because the charged particle generally travels several cells before recombination, indicating chances of multiple collisions with the lattice. Moreover, in real solid systems scattering is not only limited to the scattering between electrons and ions but also those between electrons and defects or phonons. Following the same argument that a trajectory could be modified by scattering, negligence of them impedes a proper description of the dynamics. As a result, it is important to understand the effect of and the role played by scattering for HHG in solid systems.

In addition to the issue of scattering in solids mentioned above, we would also like to investigate how a solid-phase HHG power spectrum changes under an additional static field. For gas-phase HHG, physicists have been proposing to append a static electric field on the top of a main strong driving laser to enhance certain properties of the resulting spectrum. For example, theoretical simulations show a larger plateau region induced by a weak static field can be utilized to generate ultra-short pulses shorter than that from a laser driver without a static field [32]. Also, it is shown the harmonic yield near cutoff energy could be significantly increased through a better phase-matching induced by an additional weak static field [33]. Theoretically, the effect of an extra static field on gas-phase HHG has been studied by a modified saddle-point analysis and its direct consequences are the emergence of multiple plateaus and increased cutoff energy [34, 35]. Other studies suggest that the addition of a static field could lead to HHG with elliptical dichroism(namely intensity dependence on helicities of an input laser) and elliptical polarization from a linearly polarized input laser [36]. Considering all these possible applications and studies, it is worthy of investigating the effect of a static field in solid-phase HHG and gaining a basic understanding of the system for adaptation of these results from gas-phase HHG to solid-phase HHG in the future.

1.2 The Roles of Scattering and Static Field in HHG

In this thesis, we investigate in detail the two aspects of solid-phase HHG: the role of scattering and the effect of an additional static field on a HHG power spectrum by comparing results from quantum simulations and semi-classical models.

For the understanding of scattering processes, we construct a generalized semi-classical model that contains the scattering effect and compare its results with those from complete quantum-mechanical simulations. The model, which we addressed as the generalized three-step model with Umklapp scattering, is based on the generalized three-step model and the incorporation for the specific scattering, Umklapp scattering, is carried out by considering different paths an electron-hole pair would take when it undergoes Umklapp scattering. In practice, a classical trajectory in the sense of the generalized three-step model is branched into two trajectories whenever the electron-hole pair crosses a scattering point, which is defined as the point in reciprocal space where the energy difference of neighboring bands is tiny or zero. At the scattering points, an electron-hole pair could go up or down from its current band as by definition the current band and the neighboring band almost touch each other. Therefore in this model, we branch the current trajectory into two to incorporate the effect of Umklapp scattering occurring at this point. All of these trajectories are calculated in both reciprocal and real space, and photon emission is recorded once the electron and the hole meet each other in real space. In Fig. 1.4, we compare the major difference of our model with the original generalized three-step model which neglects the scattering effect. Note that only the second step is shown in the figure as this is the only step where the difference occurs.

As a summary of the process for the generalized three-step model with Umklapp scattering, the solid-phase HHG with scattering is consists of the following three distinctive steps: (1) Excitation of an electron from the top of a valence band to the bottom of a conduction band, creating an electron-hole pair. (2) The electron-hole pair is moved in the bands by the external laser, and its trajectory is branched into two different trajectories whenever it passes a branching point. (3) When the paired electron and hole meet each other in real space, they recombine and emit a photon with energy being the

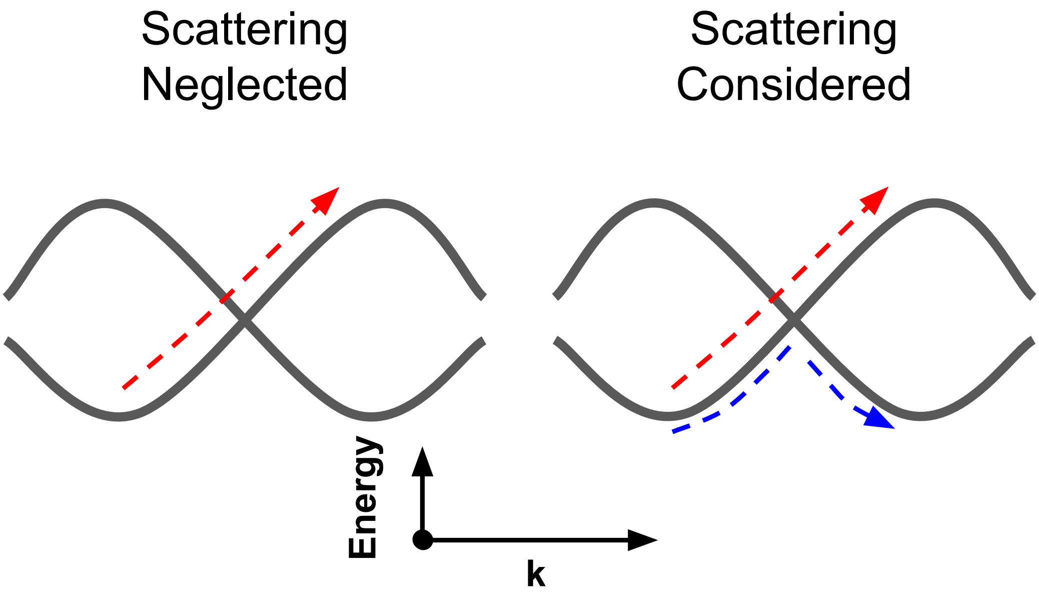

Figure 1.4: A comparison for the second step of the generalized three-step model and generalized three-step model with Umklapp scattering (our model) in crystal-momentum space. The energy bands are depicted as black curves. The red- and blue-dotted arrows describe the non-scattered and scattered paths, respectively. The left-hand side of the figure shows how the generalized three-step model treats an electron moving through a scattering point (the point where the bands cross) in the crystal-momentum space: the electron moves through a scattering point as if the neighboring band does not exist and ignores any chance to move to the neighboring band. On the other hand, the right-hand side of the figure shows that the trajectory where the electron remains in the same band (non-scattered path) and the trajectory where the electron moves to the neighboring band (scattered path) are both taken into account in our model.

difference of their corresponding band energy. From the quantum simulations, multiple plateaus are observed, which is in accordance with a previous study [7]. Using our generalized three-step model with Umklapp scattering, we found that the cutoff energy of each plateau is characterized with a specific number of scattering. The cutoff energy of the first plateau can be predicted by the trajectories experience no scattering. The cutoff energy of the second plateau is predicted by trajectories with one scattering, and the cutoff energy of the third plateau is predicted by trajectories with two scattering. This observation indicates that a photon emission in a higher plateau mainly originates from an electron-hole pair experiences more scattering. Such a phenomenon can be described by the idea of "band climbing" [7], which suggests the scattering could open up a new channels for electron-hole pairs to reach higher bands and thereby emit high-energy photons.

A model with a similar idea of trajectory branching has also been proposed in a previous study [7]. One of the major differences between the previous studies and our current work is the condition for recombination of electrons and holes. In the previous work, paired electrons and holes are assumed to recombine at any time irrespective of their separation in real space. However, in our model, an electron-hole pair is allowed to recombine only when the separation between them in real space is zero, namely when they meet. The two approaches could be considered as two extreme cases on the idea about how local the wavepacket of an electron or a hole is. If an electron and a hole have wavepackets of infinitely large spreading in real space, then they can recombine no matter how large their separation is. This equivalently leads to the recombination of electrons and holes at any time. On the other hand, if an electron and a hole have wavepackets of infinitely small spreading in real space, namely they are point particles, recombination is only possible as they locate at the same place. As a result, our work could be seen as a complementary study to provide a more complete view for Umklapp scattering in solid-phase HHG.

In addition to Umklapp scattering, we also apply a simple modification based on the concept of the mean-free path to the generalized three-step model so as to have a quick investigation for general scattering effects in solids like impurity scattering , phonon scattering, or any other form of scattering. There are two major assumptions in this simple approach. First, the possibility for an electron-hole pair to be scattered depends on the absolute distance it has traveled. The physical reason behind is that, in general, the longer the pair has traveled in solids, the more likely it will meet an impurity, a phonon, or any others and get scattered. Second, if an electron-hole pair is scattered, we just assume it would not have any chance for recombination due to its strongly-altered path by the scattering event. Combining these two simple assumptions one could therefore neglect the contribution of an electron-hole pair to solid-phase HHG with a long travel distance. For the practical implementation of this simple modification, photon emissions from an electron-hole pair predicted from the generalized three-step model are just neglected after the electron-hole pair traveled an absolute distance longer than a specified threshold. Despite how simple this model is, we can actually reproduce wavelength-independence of cutoff energy for solid-phase HHG. This result again emphasizes the importance of scattering effects in the dynamics of HHG in solid systems.

For the investigation of the effect of a static field on solid-phase HHG, we perform quantum simulations based on a simple parabolic two-band model [37] and gain insights by comparing the results with those from the generalized three-step model. The quantum system is much simplified here such that we could focus on the effect induced by the addition of a static field. From the quantum simulations, the power spectra of HHG show a tendency of decreased intensity but increased cutoff energy. Also, two plateaus are observed as a result of the broken symmetry induced by the static field, and the cutoff energy of the two plateaus depends differently on the strength of the static electric field. The cutoff energy of the higher plateau increases with a stronger static field, reaches a maximum, and then decreases to the bandgap energy when the static field is as strong as the driving laser. On the other hand, the cutoff energy of the lower plateau just decreases gradually to the bandgap energy with the increasing static field.

The behavior of the higher cutoff could be understood as a result of two competing mechanisms induced by a static field. In principle, the force of an additional static field would tend to separate electrons and holes so their probability of recombination will decrease, implying lower emission intensity. This is intuitive as no recombination is possible when an infinitely large static field is supplied. On the contrary, an extra static field could lead to higher cutoff energy because it enables the recombination of high-energy electron-hole pairs which are not able to recombine in the case without a static field. When an electron-hole pair has a longer trajectory, it generally carries high energy and therefore can emit high-energy photon if the said electron and hole could meet each and recombine. In the case when there is no static field, the force from the oscillating laser may not be strong enough to bring the electron and the hole back together. However, in the case of a static field, the chance for the electron and the hole to recombine will become higher if the force of the static field happens to be in the direction to bring them back together. The recombination channel for these high-energy electron-hole pairs opened up by the static field creates high-energy photons and thereby the cutoff energy is increased. When we consider the two mechanisms together, the second mechanism extends the cutoff energy but eventually is suppressed by the first mechanism that decreases the overall emission intensity. The results from our calculations could provide a basic understanding of the behavior of solid-phase HHG in the presence of an extra static field.

1.3 Light Absorption of Core Electrons

In attosecond science, physicists have been applying X-ray driver to invoke HHG in gas systems and synthesizing ultra-short pulses [38]. With the development of solid-phase HHG, the same idea is also introduced into solid systems. Due to the high energy of X-ray photons, it is the core electron that is involved in the process of HHG. Theoretical simulations for the core-electrons in solid systems could be quite challenging because of the complexity of the physical process and demanding computation power. To access the applicability of theoretical simulations for such core-electron excitations under a strong field, we perform a preliminary study on the absorption of X-ray by core electrons in bulk aluminum using theoretical simulations based on time-dependent density-functional theory (TDDFT) [39]. The aim here is to see whether the model system could capture the electron excitation process, which is crucial for the appropriate description of HHG, by observing how the well-known phenomenon of absorption saturation is reproduced in the model [8]. From our TDDFT simulations it is shown that the absorption coefficient could be calculated and absorption saturation of bulk aluminum under soft X-ray can indeed be reproduced. The results after focal-spot average can even be compared directly with data from experiments. As a result, it is verified that *ab initio* simulations based on TDDFT could qualitatively capture the process of photon absorption for core electrons in bulk aluminum. This preliminary study is the first step to the attempt for establishing a simulation framework for HHG from core electrons in solid systems.

1.4 Purposes and Conclusions of this Thesis

In summary, the purposes of the research carried out in this thesis are:

- To understand how scattering in the solid system affects the dynamics of solid-phase HHG and its consequences in HHG power spectra.
- To investigate the impact of a static field upon solid-phase HHG.
- To achieve a preliminary understanding about the validity of theoretical simulations based on TDDFT for X-ray absorption of core electrons in a solid system.

Through our studies, we have reached the following fundamental conclusions:

- Umklapp scattering plays an important role for HHG in solids. Our semi-classical model integrated with Umklapp scattering successfully reproduces the multi-plateau structure in HHG power spectra from quantum simulations, conforming to the previously proposed concept of band climbing and new photon emission channels.
- The wavelength independence of cutoff energy in solid-phase HHG could be reproduced by the semi-classical model neglecting electron-hole pairs with a large absolute travel distance.
- A static field could leads to splitting of cutoff energy into two for HHG in solids. One of the split cutoff energy grows with the increased strength of the static field while the other diminishes to the bandgap energy. This behavior can be understood by the broken symmetry introduced by and opposite response to the static field.
- The core-electron absorption could indeed be numerically reproduced by TDDFT and the saturable absorption of X-ray photon in bulk aluminum could be captured.

1.5 Structure of the Thesis

This thesis is organized as follows: Chapter 2 introduces the theoretical framework for *ab initio* quantum simulations and the simple parabolic two-band model for the studies of scattering effect and a static field, respectively. The semi-classical model for solid-phase HHG, namely generalized three-step model, is described in details together with its numerical implementation in Chapter 3. Within the same chapter, the integration of Umklapp scattering into the generalized three-step model is also elaborated. The results for the role of scattering and the effect of a static field are shown in Chapter 4. The investigation of core-electron absorption is presented in Chapter 5. Finally, the conclusion of this thesis is given in Chapter 6.

Chapter 2

Theoretical Models for the Quantum Systems

The investigation on the effects of electron scattering and an extra static field in this thesis are made by performing quantum simulations and verify the physical consequences of the simulated HHG by semi-classical models. The quantum models are specifically chosen such that they are simple enough for us to focus on the effects under studies. On the other hand, they are at the same time complex enough to reasonably capture some behaviors of the HHG observed in experiments. Here, we will introduce the models for quantum simulations and describe how HHG power spectra are calculated.

Two different quantum models are implemented for studying the effects of electron scattering and an extra static field. For the former case, we consider a one-dimensional non-interacting many-electron system formulated in the velocity gauge. First, the time-independent Schrödinger's equation with a given crystal model potential is solved to obtain its ground state. The state is then propagated over time under the influence of the external laser field to obtain its current density as a function of time. The HHG power spectrum is then calculated from the current density by performing Fourier transformation. As for the case investigating an extra static field, a simple parabolic two-band model is implemented [37]. This model is based on a three-dimensional non-interacting many-electron system in the velocity gauge and simplified by assuming parabolic valence and conduction bands and applying uniform matrix-element approximation. The system assumes an occupied valence band as the initial state and is propagated to calculate the current density at different time, which is then again Fourier transformed to obtain the corresponding HHG power spectrum. This much-simplified quantum model not only greatly reduces the computation cost but also ensures clear time-frequency analysis of the HHG signal, allowing for direct observation and investigation of the effect of an extra static field on spectra.

There are two main sections in this chapter and they are dedicated to the two models mentioned above: In the first section, the Hamiltonian of the quantum model, time propagation of a state, and the calculation of the current density and thereby the HHG power spectrum are introduced. Additionally, we also explicitly show the numerical implementation for each of the key steps in this model. In the second section, we introduce the parabolic two-band model and discuss the significance of the simplifications and how they are applied. The time propagation of a state and calculation of a HHG spectrum are also described shortly.

2.1 Quantum Model

Here we present the quantum model for the study on the effect of Umklapp scattering to the HHG in solids. The model considered here is a one-dimensional, non-interacting, and many-electron system formulated in velocity gauge. We only consider a one-dimensional system here because in this study only linearly-polarized laser pulse is applied, which generally suggests that the major HHG signals also lies in one axis. However, the derivation in this section will still be presented in a general three-dimensional case so as to reuse the results here and simplify the derivation in the next section introducing the parabolic two-band model. In addition, we also assume electrons are independent with each others in the model. This independent-particle approximation was examined by the previous study based on TDDFT, in which almost the same HHG power spectra are reproduced with the independent-particle approximation, where the time-dependence of Kohn-Sham potential is ignored, describing the system as non-interacting particles in a mean-field potential [40]. The reduction of dimension and the neglect of interaction greatly reduce the cost of simulations.

We also assume the laser field applied has no spatial variation, namely it is a homogeneous field, because the typical wavelength of the laser for generating HHG in solid systems is much larger than the length scale of a lattice cell. This assumption is commonly known as dipole approximation, and it enables us to reduce our simulation space to just one cell of the lattice, which again minimizes the computation cost.

2.1.1 Hamiltonian and the Ground State

In a crystal, consider an N-electron system with Hamiltonian $H^{[N]}$. The electron-electron Coulomb interaction is neglected so $H^{[N]}$ is simply a summation of N one-electron Hamiltonian:

$$H^{[N]} = \Sigma_{j=1}^{N} H_{[j]} \tag{2.1}$$

with $H_{[j]}$ being the Hamiltonian of the jth electron in the N-electron Hilbert space

$$H_{[j]} = I \otimes \cdots \otimes \underset{\uparrow \quad j\text{th term}}{H} \otimes \cdots \otimes I \quad , j \in [1, N]. \tag{2.2}$$

Here, H is the one-electron Hamiltonian in the velocity gauge

$$H = \frac{(\boldsymbol{P} - q\boldsymbol{A})^2}{2M} + U \tag{2.3}$$

where q and M are the charge (sign included) and the mass of an electron and $\boldsymbol{P} = -i\hbar\nabla$ is the momentum operator. The vector potential of the external homogeneous laser field is designated as $\boldsymbol{A} = \boldsymbol{A}(t)$ and the crystal potential is represented by $U = U(\boldsymbol{r})$. The crystal potential has a translational symmetry with a primitive lattice vector $\boldsymbol{L}$, namely $U(\boldsymbol{r} + \boldsymbol{L}) = U(\boldsymbol{r})$.

From the fact that the Hamiltonian of this N-electron system is merely a summation of N one-particle Hamiltonian (namely, electrons are not coupled) and the observable we are interested in is just a single-particle operator, we can describe the whole system with just one single Slater determinant. That is, the electrons in the system could be dealt with one by one instead of all together at the same time. In other words, this N-electron system can be effectively reduced to N one-electron systems. Therefore, we will consider a one-electron system with Hamiltonian H from here on.

The calculation of energy eigenvalue problem for the ground state can be simplified by applying Bloch's theorem. According to the theorem, an energy eigenstate $\psi(\boldsymbol{r}) = \langle \boldsymbol{r}|\psi\rangle$ in a crystal could be described by the form

$$\psi(\boldsymbol{r}) = \psi_{\boldsymbol{k}}(\boldsymbol{r}) = u_{\boldsymbol{k}}(\boldsymbol{r})e^{i\boldsymbol{k}\cdot\boldsymbol{r}} \tag{2.4}$$

with $u_{\boldsymbol{k}}(\boldsymbol{r})$ being the Bloch function with a translational symmetry of $\boldsymbol{L}$ and $\boldsymbol{k}$ being the crystal momentum. Now let $\langle \boldsymbol{r}|\psi_{n\boldsymbol{k}}\rangle = \langle \boldsymbol{r}|n\boldsymbol{k}\rangle = \psi_{n\boldsymbol{k}}(\boldsymbol{r}) = u_{n\boldsymbol{k}}(\boldsymbol{r})e^{i\boldsymbol{k}\cdot\boldsymbol{r}}$ be an energy eigenstate with the band index n and the crystal momentum $\boldsymbol{k}$ and its corresponding energy be $E_{n\boldsymbol{k}}$. By applying $|n\boldsymbol{k}\rangle$ and $\langle \boldsymbol{r}|$ on the right and left of Eq. 2.3, we have:

$$\begin{aligned}\langle \boldsymbol{r}|H|n\boldsymbol{k}\rangle &= \frac{e^{i\boldsymbol{k}\cdot\boldsymbol{r}}}{M}\Big[\frac{-\hbar^2}{2}\nabla^2 - i\hbar(\hbar\boldsymbol{k} - q\boldsymbol{A})\cdot\nabla + \frac{|\hbar\boldsymbol{k}|^2}{2} + \frac{|q\boldsymbol{A}|^2}{2} - \hbar q\boldsymbol{k}\cdot\boldsymbol{A}\Big]u_{n\boldsymbol{k}}(\boldsymbol{r}) + e^{i\boldsymbol{k}\cdot\boldsymbol{r}}U(\boldsymbol{r})u_{n\boldsymbol{k}}(\boldsymbol{r})\\ &= E_{n\boldsymbol{k}}e^{i\boldsymbol{k}\cdot\boldsymbol{r}}u_{n\boldsymbol{k}}(\boldsymbol{r})\end{aligned}$$

or, after canceling the same terms for the two equations on the right:

$$\begin{aligned}E_{n\boldsymbol{k}}u_{n\boldsymbol{k}}(\boldsymbol{r}) &= \Big[\frac{-\hbar^2}{2M}\nabla^2 - \frac{i\hbar}{M}(\hbar\boldsymbol{k} - q\boldsymbol{A})\cdot\nabla + \frac{|\hbar\boldsymbol{k}|^2}{2M} + \frac{|q\boldsymbol{A}|^2}{2M} - \frac{\hbar q}{M}\boldsymbol{k}\cdot\boldsymbol{A} + U(\boldsymbol{r})\Big]u_{n\boldsymbol{k}}(\boldsymbol{r})\\ &= \Big[\frac{(-i\hbar\nabla + \hbar\boldsymbol{k} - q\boldsymbol{A})^2}{2M} + U\Big]u_{n\boldsymbol{k}}(\boldsymbol{r})\\ &= H^{[\boldsymbol{k}]}u_{n\boldsymbol{k}}(\boldsymbol{r}).\end{aligned} \tag{2.5}$$

This eigenvalue problem without external laser, namely $\boldsymbol{A}(t) = 0$, is then solved numerically for each $\boldsymbol{k}$ to form the ground state of the system. In this model, we will consider an N-electron ground state with fully occupied valence bands and completely empty conduction bands. This ground state also serves as the initial state of the many-electron system. The corresponding single-electron state at crystal momentum $\boldsymbol{k}$ lying in a valence band ν at the beginning of the time $t = 0$ will be designated by

$$\phi_{\nu\boldsymbol{k}}(\boldsymbol{r}; t = 0) = \langle \boldsymbol{r}|\phi_{\nu\boldsymbol{k}}(t = 0)\rangle = \langle \boldsymbol{r}|\psi_{\nu\boldsymbol{k}}\rangle. \tag{2.6}$$

This state will be propagated over time for the calculation of HHG power spectra.

2.1.2 Time Propagation and HHG Power Spectrum

In this model, the time evolution of the single-electron state $|\phi(t)\rangle$ is governed by Schrödinger's equation:

$$i\hbar\frac{\partial}{\partial t}\phi_{\nu\boldsymbol{k}}(\boldsymbol{r};t) = \langle\boldsymbol{r}|H|\phi_{\nu\boldsymbol{k}}(t)\rangle \tag{2.7}$$

or, after applying Bloch's theorem with $\phi_{\nu\boldsymbol{k}}(\boldsymbol{r};t) = u_{\boldsymbol{k}}(\boldsymbol{r};t)e^{i\boldsymbol{k}\cdot\boldsymbol{r}}$, we have

$$i\hbar\frac{\partial}{\partial t}u_{\boldsymbol{k}}(\boldsymbol{r};t) = \frac{(-i\hbar\nabla + \hbar\boldsymbol{k} - q\boldsymbol{A}(t))^2}{2M}u_{\boldsymbol{k}}(\boldsymbol{r};t) + U(\boldsymbol{r})u_{\boldsymbol{k}}(\boldsymbol{r};t). \tag{2.8}$$

Note that, at the beginning of the time the Bloch function is just the one of a valence band specified by ν, namely $u_{\boldsymbol{k}}(\boldsymbol{r};t=0) = u_{\nu\boldsymbol{k}}(\boldsymbol{r})$. Eq. 2.8 will be the actual dynamical equation implemented in our numerical simulations.

Once we have the state at any given time, the current density $\boldsymbol{J}(t)$ could then be calculated by

$$\begin{aligned}\boldsymbol{J}(t) &= \sum_{\nu}\frac{1}{\Omega_B}\int_{\Omega_B}\boldsymbol{J}_{\nu\boldsymbol{k}}(t)d\boldsymbol{k} \\ \boldsymbol{J}_{\nu\boldsymbol{k}}(t) &= \frac{q}{M}\langle\phi_{\nu\boldsymbol{k}}(t)|\boldsymbol{P} - q\boldsymbol{A}(t)|\phi_{\nu\boldsymbol{k}}(t)\rangle \\ &= \frac{q}{M}\frac{1}{\Omega_C}\int_{V_C}d\boldsymbol{r}u^*_{\nu\boldsymbol{k}}(\boldsymbol{r};t)(-i\hbar\nabla + \hbar\boldsymbol{k} - q\boldsymbol{A})u_{\nu\boldsymbol{k}}(\boldsymbol{r};t)\end{aligned} \tag{2.9}$$

where Ω_B and Ω_C are the volume of the first Brillouin zone and the volume of a primitive cell. And the $\int_{\Omega_B} d\boldsymbol{k}$ and $\int_{\Omega_C} d\boldsymbol{r}$ indicate integration over the first Brillouin zone and one primitive cell, respectively. Note that $\boldsymbol{J}_{\nu\boldsymbol{k}}(t)$ is the contribution from one electron to the total current density $\boldsymbol{J}(t)$ of the N-electron system. Here we would like to address that ν and $\boldsymbol{k}$ in the above equations merely indicate what the band index and crystal momentum a state $\phi_{\nu\boldsymbol{k}}(t)$ have at the initial time and they do not suggest the corresponding state is always in the valence band denoted by ν over time.

As the electric field of the light emission is proportional to the acceleration of charged particles, we could extract the HHG power spectrum through the Fourier transformation of the current. Therefore, the emission power spectrum $P(\omega)$ can be calculated by

$$P(\omega) = \omega^2|\mathcal{FT}\{\boldsymbol{J}(t)W(t)\}(\omega)|^2 \tag{2.10}$$

with $\mathcal{FT}$ being Fourier transformation and $W(t)$ a window function. The application of a window function onto current density before Fourier transformation allows for a smoother spectrum. Here we will simply use the envelop of the laser field as the window function. An example for the HHG power spectrum is given in Fig 2.1, together with the electric field of the corresponding driving laser and the current density the laser creates.

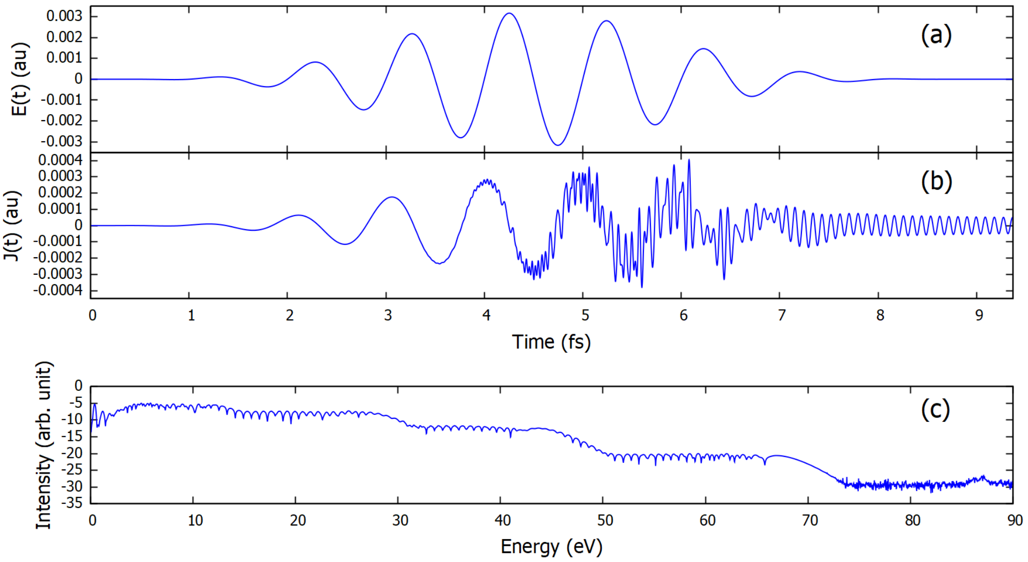

Figure 2.1: Some examples of numerical calculations for HHG in a solid system based on the one-dimensional quantum model introduced in this section. The electric field of an applied laser as a function of time is described in (a). The current density generated from the system as a response to the applied laser field shown in (a) is also described in (b) as a function of time. The HHG power spectrum calculated from the current density in (b) is shown in (c).

2.1.3 Time-Frequency Analysis

To study the dynamics of the HHG, we will perform time-frequency analysis to extract the emission time and energy of the generated photons. This analysis involves superimposing the predictions from a semi-classical model onto the results from a quantum simulation. Therefore, one can trace the origin of the emission and understand how they are affected by scattering. The details of the semi-classical models will be described in the next chapter. For the quantum signals, we perform the short-time Fourier transformation, specifically the Gabor transform, to the current density to obtain its emission strength as a function of emission time τ and emission energy (or equivalently photon frequency ω):

$$G(\tau,\omega) = \left|\mathcal{FT}\{\boldsymbol{J}(t)e^{\frac{-(t-\tau)^2}{2\sigma^2}}\}(\omega)\right|^2 \tag{2.11}$$

with σ being the standard deviation of the Gaussian. Note that this Gabor transformation is nothing but Fourier transform of the current density sampled by Gaussian function near a specified time τ, and therefore one can interpret the result $G(\tau,\omega)$ as the emission spectrum from the system around time τ. How closely this spectrum is related to the emission time τ is determined by the standard deviation σ. Small σ suggests the Gaussian window vanishes very quickly with time t moving away from τ and thereby current density at time far away from τ will take little part in the final spectrum $G(\tau, \omega)$.

Note that the value of this σ should be smaller than the time scale of an emission event, otherwise such events can not be resolved in the time domain and the information for the time of recombination is lost. As an emission event, which consists of the motion of an electron moving away from and coming back to a core ion, is mainly controlled by the driving laser, we can roughly estimate the time scale of an emission event to be one optical cycle of the laser. Therefore, σ is always smaller than one optical cycle. However, σ should not be too small so as to avoid large uncertainty in frequency domain (or equivalently, energy domain). In practice, one would typically tune σ to make sure the signal in the energy range of interest has good resolution in both time and frequency.

The short-time Fourier transformation allows us to extract the emission time τ and emission energy $\hbar\omega$ of HHG from the quantum system. On the other hand, we can also calculate the timing and energy from a semi-classical model. When the two signals are plotted together and match each other to a reasonable degree, one could then attribute the origin of a photon emission to a specific classical trajectory in the semi-classical model. This procedure is commonly addressed as time-frequency analysis. If an HHG event is successfully characterized to a trajectory in the procedure, this analysis could provide crucial information for the HHG like time of excitation, motion of the corresponding electron-hole pair, and interaction between the pair and the external laser. Therefore, time-frequency analysis could allow for a deeper understanding of the quantum signal and dynamics of HHG.

In Fig. 2.2, we demonstrate a simple example of the time-frequency analysis. The short-time Fourier transformation of the current density from a quantum simulation $G(\tau, \omega)$ is plotted as the color map in the background of the figure, and the classical predictions are marked by black circles. The classical predictions from a semi-classical model will be introduced and connected to the time-frequency analysis here in the next chapter. One can see that, in the energy domain of 7 to 14 eV and time domain of 35 to 65, the structure of the major time-frequency signals of $G(\tau, \omega)$ (colored in red) are reasonably reproduced by the classical results. We can than connect this major emission with the specific trajectory and investigate its dynamics.

2.1.4 Numerical Implementation

Here we will describe the numerical implementation on solving the energy eigenvalue problem in Eq. 2.5 for the ground state and propagating the wavefunction of an electron over time according to Eq. 2.8 for the current density. As we are actually dealing with a one-dimensional system, the corresponding Hamiltonian, dynamical equation, and other quantities shown here will be reduced to their one-dimensional versions, e.g., $\boldsymbol{k} \rightarrow k$, $\boldsymbol{r} \rightarrow r$, $\boldsymbol{A}(t) \rightarrow A(t)$, $\boldsymbol{L} \rightarrow L$ *etc.*

Evenly-distributed grids are employed to discretize both real-space (r-space) and

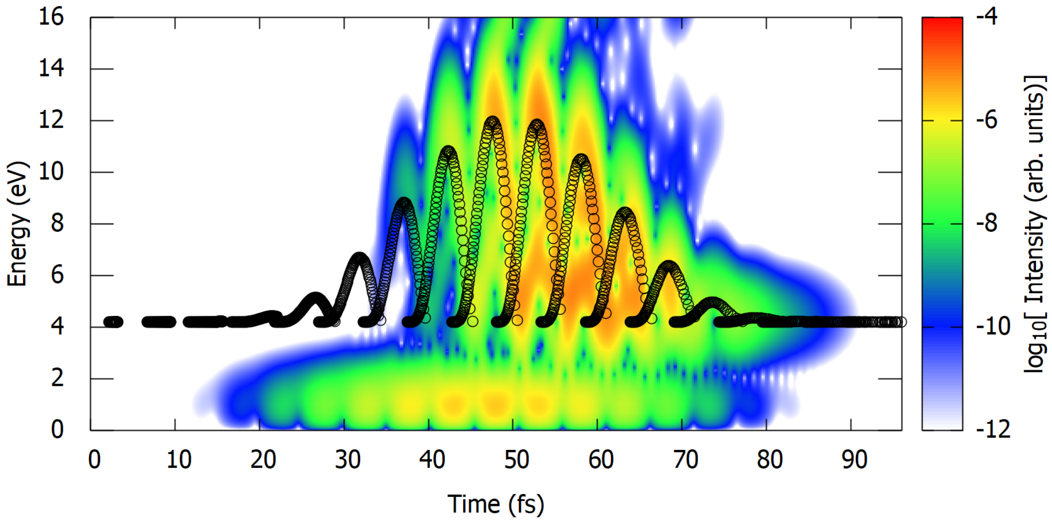

Figure 2.2: An example for the time-frequency analysis. The spectrum of the current density from the short-time Fourier transformation is shown as the color map in the background, and the emission timing and energy from a semi-classical model is marked by black circles.

crystal-momentum space (k-space). For r-space, we have:

$$r_j = \Delta r \times (j - 0.5) - \frac{L}{2} \quad , j \in \{1, 2, \cdots, N_r\} \tag{2.12}$$

where N_r is the number of grid points and $\Delta r = \frac{L}{N_r}$ is the grid spacing. Note that the choice of shift here guarantee inversion symmetry for the grids. For k-space, the grid points are also defined in the similar way as:

$$k_j = \Delta k \times (j - 0.5) - \frac{\pi}{L} \quad , j \in \{1, 2, \cdots, N_k\} \tag{2.13}$$

where N_k and $\Delta k = \frac{2\pi}{LN_k}$ are the number of grid points and the grid spacing, respectively.

The numerical calculation of derivatives is carried out simply by finite difference method to the 4th-order (using 5 grid points). The first and second derivatives of the Bloch function $u_{nk}(r)$ with respect to r at $r = r_j$ can be calculated by (let $u_j = u_{nk}(r_j)$ for simplicity):

$$\left.\frac{\partial u_{nk}(r)}{\partial r}\right|_{r=r_j} \approx \sum_{l=-2,\cdots,2} \frac{D_l^{[1]} u_{j+l}}{\Delta r} \quad , (D_0^{[1]}, D_{\pm1}^{[1]}, D_{\pm2}^{[1]}) = (0, \pm\frac{2}{3}, \mp\frac{1}{12}) \tag{2.14}$$

$$\left.\frac{\partial^2 u_{nk}(r)}{\partial r^2}\right|_{r=r_j} \approx \sum_{l=-2,\cdots,2} \frac{D_l^{[2]} u_{j+l}}{\Delta r^2} \quad , (D_0^{[1]}, D_{\pm1}^{[1]}, D_{\pm2}^{[1]}) = (\frac{5}{2}, \frac{4}{3}, -\frac{1}{12}). \tag{2.15}$$

Keep in mind that the space is periodic so the index $j = N+1$ and $j = N+2$ correspond to $j = 1$ and $j = 2$ and $j = 0$ and $j = -1$ correspond to $j = N$ and $j = N-1$.

With the numerical form of the derivatives, the one-dimensional version of Eq. 2.5 can be written in the form $E_{nk}u_\alpha = \sum_\beta h_{\alpha\beta}u_\beta$ as shown by the following:

$$\begin{aligned}
E_{nk}u_\alpha &= H^{[k]}u_\alpha \\
&= \frac{-\hbar^2}{2M}\sum_\gamma \frac{D^{[2]}_\gamma}{\Delta r^2}u_{\alpha+\gamma} - \frac{i\hbar}{M}(\hbar k - qA)\sum_\gamma \frac{D^{[1]}_\gamma}{\Delta r}u_{\alpha+\gamma} + \big[\frac{|\hbar k|^2}{2M} + \frac{|qA|^2}{2M} - \frac{\hbar q}{M}kA + U(r_\alpha)\big]u_\alpha \\
&= \sum_\beta \Big\{\frac{-\hbar^2}{2M}\sum_\gamma \frac{D^{[2]}_\gamma}{\Delta r^2}\delta_{\beta,\alpha+\gamma} - \frac{i\hbar}{M}(\hbar k - qA)\sum_\gamma \frac{D^{[1]}_\gamma}{\Delta r}\delta_{\beta,\alpha+\gamma} \\
&\qquad + \delta_{\alpha\beta}\big[\frac{|\hbar k|^2}{2M} + \frac{|qA|^2}{2M} - \frac{\hbar q}{M}kA + U(r_\alpha)\big]\Big\}u_\beta \\
&= \sum_\beta h_{\alpha\beta}u_\beta
\end{aligned} \tag{2.16}$$

with γ an integer running from -2 to 2. After setting $A = 0$, the eigenvalues and eigenfunctions of the matrix h will then be solve with conventional numerical solver.

In the time domain, the time axis is discretized evenly with a time step Δt from $t = 0$ to a specified time. A Bloch state at the next time grid is calculate through the application of time propagator on the corresponding state at present time grid according to the one-dimensional version of Eq. 2.8. Therefore, we have $u_k(t+\Delta t) = e^{\frac{H^{[k]}(t)}{i\hbar}\Delta t}u_k(t)$. For the time propagator, Taylor expansion to the 4th order is implemented so the Bloch state at next time is numerically calculated by:

$$u_k(t+\Delta t) \approx \big[1 + \sum_{j=1,\cdots,4}\frac{1}{j!}(\frac{(H^{[k]}(t))\Delta t}{i\hbar})^j\big]u_k(t). \tag{2.17}$$

The actual operation for applying multiple $H^{[k]}$ on the Bloch state can be done by utilizing the right-hand side of Eq. 2.16 repeatedly.

Finally, the evaluation of the current density $J(t)$ at any given time grid is numerically carried out by the discretized form of one-dimensional version of Eq. 2.9:

$$J(t) = \frac{1}{\Omega_B}\sum_{\nu,\alpha} J_{\nu k_\alpha}\Delta k \tag{2.18}$$

$$J_{\nu k_\alpha} = \frac{q}{M\Omega_C}\sum_\beta \Big[(\hbar k - qA(t))|u_{\nu k_\alpha}(r_\beta;t)|^2\Delta r - i\hbar\sum_{\gamma=-2,\cdots,+2} u^*_{\nu k_\alpha}(r_\beta;t)D^{[1]}_\gamma u_{\nu k_\alpha}(r_{\beta+\gamma};t)\Big].$$

To have reliable numerical results, simulations are verified by gradually using smaller Δr, Δk, and Δt and observe the converging behavior for the current density and the corresponding HHG spectrum.

2.2 The Parabolic Two-Band Model

The addition of a static electric field to the laser invokes various changes in electron dynamic, altering the corresponding HHG in a very complex and intertwined way. Therefore, we would like to really simplify the quantum model so as to focus on the mechanism of interest and understand the impact of the static field. The specific mechanism we would like to investigate here is how the change of the trajectory of an electron by the extra static field makes its way to the corresponding HHG power spectrum. To achieve this, we consider a non-interacting, many-electron model like the one introduced in the previous section but reduce the number of bands to just one conduction band and one valence band. Additionally, we avoid solving the energy structure of the system and just explicitly assign parabolic bands to the model. After these major reductions, various minor approximations are made to further reduce the complexity of the system and facilitate simulations of the model.

2.2.1 The Dynamical Equation and Approximations

Here we first introduce the Houston's state [41] as they will be utilized as a basis set to expand the dynamical equation in Eq. 2.8 for a Bloch wavefunction. The Houston state $\eta_{n\boldsymbol{k}}(\boldsymbol{r};t)$ could be define as the instantaneous energy eigenstates at time t with a phase accumulated over its trajectory $\boldsymbol{K}(t)$ in crystal-momentum space [41]:

$$\eta_{n\boldsymbol{k}}(\boldsymbol{r};t) = e^{\int_0^t \frac{E_{n\boldsymbol{K}(t')}}{i\hbar}dt'} u_{n\boldsymbol{K}(t)}(\boldsymbol{r}) \tag{2.19}$$

where $u_{n\boldsymbol{K}(t)}(\boldsymbol{r})$ is the instantaneous energy eigenstate at time t with $E_{n\boldsymbol{K}(t)}$ being the corresponding energy:

$$E_{n\boldsymbol{K}(t)} u_{n\boldsymbol{K}(t)}(\boldsymbol{r}) = H^{[\boldsymbol{K}(t)]} u_{n\boldsymbol{K}(t)}(\boldsymbol{r}). \tag{2.20}$$

The trajectory in crystal-momentum space $\boldsymbol{K}(t)$ here can be calculated by the acceleration theorem:

$$\boldsymbol{K}(t) = \boldsymbol{k} - \frac{q}{\hbar}\boldsymbol{A}(t) \tag{2.21}$$

where $\boldsymbol{k}$ is the initial crystal momentum of the state. Notice that, by performing time derivative on Eq. 2.21, one could obtain the Newton-like equation:

$$\frac{d\hbar\boldsymbol{K}(t)}{dt} = q\boldsymbol{E}(t) = \boldsymbol{F}_{laser}(t) \tag{2.22}$$

with F_{laser} being the force of the laser exerted on an electron. The laser applied within this model will be composed of an oscillating field and a static field. The oscillating part is a typical linearly-polarized laser. The electric fields from both components are assumed to lie in the z direction.

Now we can expand the Bloch function of an electron using a basis formed from the Houston's states:

$$u_{\boldsymbol{k}}(\boldsymbol{r};t) = \sum_n C_{n\boldsymbol{k}}(t)\eta_{n\boldsymbol{k}}(\boldsymbol{r};t) \tag{2.23}$$

with $C_{n\boldsymbol{k}}(t)$ being the expansion coefficients and n the index of a band involved. Feeding this expansion into the dynamical equation in Eq. 2.8 for the general model shown in the previous section, we would have on the left-hand side Eq. 2.8:

$$\begin{aligned}
i\hbar\frac{\partial}{\partial t}u_{\boldsymbol{k}}(\boldsymbol{r};t) &= i\hbar\frac{\partial}{\partial t}\sum_n C_{n\boldsymbol{k}}(t)\eta_{n\boldsymbol{k}}(\boldsymbol{r};t)\\
&= i\hbar\sum_n \frac{\partial C_{n\boldsymbol{k}}(t)}{\partial t}\eta_{n\boldsymbol{k}}(\boldsymbol{r};t) + i\hbar\sum_n C_{n\boldsymbol{k}}(t)\frac{\partial \eta_{n\boldsymbol{k}}(\boldsymbol{r};t)}{\partial t}\\
&= i\hbar\sum_n \frac{\partial C_{n\boldsymbol{k}}(t)}{\partial t}\eta_{n\boldsymbol{k}}(\boldsymbol{r};t) + \sum_n C_{n\boldsymbol{k}}(t)i\hbar\frac{\partial}{\partial t}\left[e^{\int_0^t \frac{E_{n\boldsymbol{K}(t')}}{i\hbar}dt'}u_{n\boldsymbol{K}(t)}(\boldsymbol{r})\right]\\
&= i\hbar\sum_n \frac{\partial C_{n\boldsymbol{k}}(t)}{\partial t}\eta_{n\boldsymbol{k}}(\boldsymbol{r};t) + \sum_n C_{n\boldsymbol{k}}(t)\left[E_{n\boldsymbol{K}(t)}\eta_{n\boldsymbol{k}}(\boldsymbol{r};t) + e^{\int_0^t \frac{E_{n\boldsymbol{K}(t')}}{i\hbar}dt'}i\hbar\frac{\partial u_{n\boldsymbol{K}(t)}(\boldsymbol{r})}{\partial t}\right]\\
&= i\hbar\sum_n \frac{\partial C_{n\boldsymbol{k}}(t)}{\partial t}\eta_{n\boldsymbol{k}}(\boldsymbol{r};t) + \sum_n C_{n\boldsymbol{k}}(t)E_{n\boldsymbol{K}(t)}\eta_{n\boldsymbol{k}}(\boldsymbol{r};t) +\\
&\qquad \sum_n C_{n\boldsymbol{k}}(t)iF_{laser}(t)e^{\int_0^t \frac{E_{n\boldsymbol{K}(t')}}{i\hbar}dt'}\frac{\partial u_{n\boldsymbol{K}(t)}(\boldsymbol{r})}{\partial \boldsymbol{K}(t)}.
\end{aligned} \tag{2.24}$$

Note that we have utilized the relation $i\hbar\frac{\partial u_{n\boldsymbol{K}(t)}}{\partial t} = i\hbar\frac{\partial u_{n\boldsymbol{K}(t)}}{\partial \boldsymbol{K}(t)}\frac{d\boldsymbol{K}(t)}{dt} = i\frac{\partial u_{n\boldsymbol{K}(t)}}{\partial \boldsymbol{K}(t)}F_{laser}(t)$ in the last line. As for the the right-hand side of Eq. 2.8, we have:

$$\begin{aligned}
H^{[\boldsymbol{K}(t)]}u_{\boldsymbol{k}}(\boldsymbol{r};t) &= \sum_n C_{n\boldsymbol{k}}(t)H^{[\boldsymbol{K}(t)]}\eta_{n\boldsymbol{k}}(\boldsymbol{r};t)\\
&= \sum_n C_{n\boldsymbol{k}}(t)e^{\int_0^t \frac{E_{n\boldsymbol{K}(t')}}{i\hbar}dt'}H^{[\boldsymbol{K}(t)]}u_{n\boldsymbol{K}(t)}(\boldsymbol{r})\\
&= \sum_n C_{n\boldsymbol{k}}(t)e^{\int_0^t \frac{E_{n\boldsymbol{K}(t')}}{i\hbar}dt'}E_{n[\boldsymbol{K}(t)]}u_{n\boldsymbol{K}(t)}(\boldsymbol{r})\\
&= \sum_n C_{n\boldsymbol{k}}(t)E_{n[\boldsymbol{K}(t)]}\eta_{n\boldsymbol{k}}(\boldsymbol{r};\boldsymbol{t}).
\end{aligned} \tag{2.25}$$

The equivalence of the two sides of then yields (note that $\sum_n C_{n\boldsymbol{k}}(t)E_{n[\boldsymbol{K}(t)]}\eta_{n\boldsymbol{k}}(\boldsymbol{r};\boldsymbol{t})$ on both sides cancel out each other):

$$i\hbar\sum_n \frac{\partial C_{n\boldsymbol{k}}(t)}{\partial t}\eta_{n\boldsymbol{k}}(\boldsymbol{r};t) = -\sum_n C_{n\boldsymbol{k}}(t)iF_{laser}(t)e^{\int_0^t \frac{E_{n\boldsymbol{K}(t')}}{i\hbar}dt'}\frac{\partial u_{n\boldsymbol{K}(t)}(\boldsymbol{r})}{\partial \boldsymbol{K}(t)} \tag{2.26}$$

For simplicity, we would let $\int_0^t \frac{E_{n\boldsymbol{K}}(t')}{i\hbar}dt' = \theta_n(t)$. Multiplying $\eta_{m\boldsymbol{k}}(\boldsymbol{r};t)$ on both sides of Eq. 2.26 and integrate over one cell in real space, one would have:

$$\begin{aligned} & i\hbar\sum_n \frac{\partial C_{n\boldsymbol{k}}(t)}{\partial t} e^{(\theta_n(t)-\theta_m(t))}\frac{1}{\Omega_C}\int_\Omega u^*_{m\boldsymbol{K}(t)}(\boldsymbol{r})u_{n\boldsymbol{K}(t)}(\boldsymbol{r})d\boldsymbol{r} \\ & = -iF_{laser}\sum_n C_{n\boldsymbol{k}}(t)e^{(\theta_n(t)-\theta_m(t))}\frac{1}{\Omega_C}\int_{\Omega_C} u^*_{m\boldsymbol{K}(t)}(\boldsymbol{r})\frac{\partial u_{n\boldsymbol{K}(t)}(\boldsymbol{r})}{\partial \boldsymbol{K}(t)}d\boldsymbol{r} \end{aligned} \tag{2.27}$$

or, after using the orthonormality of $u_{n\boldsymbol{K}(t)}(\boldsymbol{r})$:

$$i\hbar\frac{\partial C_{m\boldsymbol{k}}(t)}{\partial t} = -iF_{laser}\sum_n C_{n\boldsymbol{k}}(t)e^{(\theta_n(t)-\theta_m(t))}\boldsymbol{\chi}^{[\boldsymbol{K}(t)]}_{mn} \tag{2.28}$$

$$\boldsymbol{\chi}^{[\boldsymbol{K}(t)]}_{mn} = \frac{1}{\Omega_C}\int_{\Omega_C} u^*_{m\boldsymbol{K}(t)}(\boldsymbol{r})\frac{\partial u_{n\boldsymbol{K}(t)}(\boldsymbol{r})}{\partial \boldsymbol{K}(t)}d\boldsymbol{r}.$$

Note that Eq. 2.28 describes the Schrödinger's equation in the basis formed by Houston's states. We will apply several approximation based on this equation to reduce the complexity of the system.

The major simplification is to consider only two bands in the expansion of the Bloch function in Eq. 2.23. One of them is the conduction band $n = c$ and the other is the valence band $n = \nu$. Another simplification is that we would directly assign band energy to the system instead of solving the energy eigenvalue problem starting from a model potential in the previous section. The energy bands are simply modeled in the parabolic form:

$$E_{\nu\boldsymbol{k}} = -\frac{|\hbar\boldsymbol{k}|^2}{2M_\nu} \tag{2.29}$$

$$E_{c\boldsymbol{k}} = E_g + \frac{|\hbar\boldsymbol{k}|^2}{2M_c} \tag{2.30}$$

with E_g being the band gap and M_ν and M_c being the effective mass in the valence band and conduction band, respectively.

In addition, for the elements of $\chi(t)$ in Eq. 2.28, we set the diagonal components $\boldsymbol{\chi}^{[\boldsymbol{K}(t)]}_{cc}$ and $\boldsymbol{\chi}^{[\boldsymbol{K}(t)]}_{\nu\nu}$ to zero for simplicity. For the off-diagonal terms $\boldsymbol{\chi}^{[\boldsymbol{K}(t)]}_{\nu c}$ (and its complex conjugate), it could be written as

$$\boldsymbol{\chi}^{[\boldsymbol{K}(t)]}_{\nu c} = \frac{-\hbar}{M}\frac{1}{E_{\nu\boldsymbol{K}(t)} - E_{c\boldsymbol{K}(t)}}\frac{1}{\Omega_C}\int_{\Omega_C} u^*_{\nu\boldsymbol{K}(t)}(\boldsymbol{r})(-i\hbar\nabla)u_{c\boldsymbol{K}(t)}(\boldsymbol{r})d\boldsymbol{r} \tag{2.31}$$

by evoking the relation:

$$\int_{\Omega_C} u^*_{m\boldsymbol{K}(t)}(\boldsymbol{r})\frac{\partial}{\partial\boldsymbol{K}(t)}u_{n\boldsymbol{K}(t)}(\boldsymbol{r})d\boldsymbol{r} = \frac{-\hbar}{E_{m\boldsymbol{K}(t)} - E_{n\boldsymbol{K}(t)}}\int_{\Omega_C} u^*_{m\boldsymbol{K}(t)}(\boldsymbol{r})\frac{-i\hbar\nabla}{M}u_{n\boldsymbol{K}(t)}(\boldsymbol{r})d\boldsymbol{r}. \tag{2.32}$$

See Appendix A for the proof of this relation. Now we assume the dependence of the integral on crystal momentum $\boldsymbol{K}(t)$ is negligible, namely the uniform-matrix element approximation, to further ease the calculation:

$$\frac{1}{\Omega_C}\int_{\Omega_C} u^*_{c\boldsymbol{K}(t)}(\boldsymbol{r})(-i\hbar\nabla)u_{\nu\boldsymbol{K}(t)}(\boldsymbol{r})d\boldsymbol{r} \approx \boldsymbol{p}_{c\nu}, \tag{2.33}$$

The projection of $\boldsymbol{p}_{c\nu} = \boldsymbol{p}^*_{\nu c}$ along the laser direction $p_{c\nu}$ is approximated according to Kane's two-band model [42]:

$$p_{c\nu} = \frac{M}{2}\sqrt{\frac{E_g}{M_r}} \tag{2.34}$$

where $M_r = (M_c^{-1} + M_\nu^{-1})^{-1}$ is the reduced effective mass. With all these approximations, now we have the original dynamical equation of the system in Eq. 2.28 reduced to:

$$i\hbar\frac{\partial C_{\nu\boldsymbol{k}}(t)}{\partial t} = C_{c\boldsymbol{k}}(t)e^{(\theta_c(t)-\theta_\nu(t))}\frac{-i\hbar\boldsymbol{F}_{laser}(t)\cdot\boldsymbol{p}_{\nu c}}{M_r[E_{c\boldsymbol{K}(t)} - E_{\nu\boldsymbol{K}(t)}]}. \tag{2.35}$$

This is the dynamical equation for our parabolic two-band model.

The initial state of the many-electron system is a state with a fully occupied valence band and a completely empty conduction band, namely $C_{\nu\boldsymbol{k}} = 1$ and $C_{c\boldsymbol{k}} = 0$ for each $\boldsymbol{k}$ at initial time. The state will be propagated by the dynamical equation in Eq. 2.35, and the current density in the direction of the laser, $J_z(t)$ will be calculated at each time step. This current density is the summation of the corresponding intra-band current density $J_z^{Intra}(t)$ and the inter-band current density $J_z^{Inter}(t)$:

$$J_z(t) = J_z^{Intra}(t) + J_z^{Inter}(t) \tag{2.36}$$

$$J_z^{Intra}(t) = \frac{q}{\Omega_B}\int_{\Omega_B}[v_z^\nu|C_{\nu\boldsymbol{k}}|^2 + v_z^c|C_{c\boldsymbol{k}}|^2]d\boldsymbol{k} \tag{2.37}$$

$$J_z^{Inter}(t) = \frac{qp_{c\nu}}{\Omega_B}\int_{\Omega_B} 2Re\Big\{C^*_{c\boldsymbol{k}}C_{\nu\boldsymbol{k}}\Big\}d\boldsymbol{k} \tag{2.38}$$

where $v_z^\nu = \frac{k_z}{M_\nu}$ and $v_z^c = \frac{k_z}{M_c}$ are group velocity of the valence band and the conduction band, respectively. Note that the idea of decomposing the current density into intra- and inter-band components is only defined within the Houston's states so one could naturally have different intra- or inter-band components if different basis functions for expansion are utilized.

To obtain the HHG spectrum of the system, we perform Fourier transformation on $J_z(t)$ only and neglect components in other directions. As electrons are not subjected to the external laser force in these direction, it could be expected the current density perpendicular to the laser polarization would be negligible.

For the simulations of the system, we run the program PANDA which is dedicated for investigating non-linear electron dynamics using the two-band-model [43]. In addition, the output data is considered converged if the results in current density and HHG power spectrum remain essentially the same when the number of grid points in $\boldsymbol{k}$-space and time are gradually increased.

Chapter 3

Semi-Classical Models and Umklapp Scattering

Semi-classical models play an indispensable role in understanding the mechanisms of the HHG in solid or gas systems as they provide simple and clear physical pictures for the corresponding dynamics. From time to time, the power spectrum of the HHG from experiments or theoretical quantum simulations could yield very complex pattern and thereby are quite difficult to understand its formation. On the other hand, a semi-classical model for the HHG is generally formulated based on classical mechanics with additions of quantum excitation and recombination. The simplicity of a semi-classical model enables us to understand the dynamics of the HHG and provides a clear physical picture while at the same time reproduces the experiments or theoretical quantum simulations to some reasonable degree. As a result, it is a common and useful approach to analyze the quantum or experimental data by comparing them with a corresponding semi-classical model and distill the key ingredient of the physical process.

In addition to capturing the mechanism of the HHG, a semi-classical model could also serve as a foundation for making predictions for experimentalists on some crucial properties of the HHG. For example, the three-step model for gas-phase HHG can actually provide a formula for the cutoff energy of the HHG and reproduce the quadratic dependence of the energy on the electric field amplitude observed in experiments. With the quantitative and qualitative description of the cutoff energy accurate to this degree, physicists could estimate how far a plateau could extend under different laser strength and evaluate the applicability of the gaseous HHGs under the different setup of a laser. This ability to make predictions also signifies the need to construct a semi-classical model for HHG in solid systems.

One of the very important semi-classical model for solid-phase HHG is proposed by Vampa *at al.*, who has extended the idea of a parabolic energy dispersion of a free electron in the gas-phase HHG to the complex energy dispersion in solid systems [4]. This extended semi-classical model also describes the solid-phase HHG in three steps similar to the original three-step model. Based on this model, an approximated formula for the cutoff energy is proposed, albeit under very strong simplification of the band structure

[5]. The complex structure of the energy bands in solids really poses a huge obstacle for a simple picture so a well-accepted model like the three-step model in gas-phase HHG has not yet been achieved in the realm of solid-phase HHG.

The semi-classical model for the solid-phase HHG could be further improved by including other mechanisms in solids. The specific factor we want to investigate here is the of Umklapp scattering. When an electron-hole pair is created by a strong laser and move inside a crystal, it is natural to expected that the pair would have chances to undergo scattering with the lattice. The scattering events should, in principle, modify the trajectory of the pair and its possibility to recombine. The HHG power spectrum from photons emitted from the recombination then should also altered to some degree by the scattering. We would show that this kind of scattering could be integrated into Vampa's semi-classical model by creating a new scattered trajectory in addition to the conventional non-scattered trajectory whenever such a scattering event occurs. This idea has been proposed in previous studies and the appearance of multiple plateaus in the HHG power spectrum is attributed to such a scattering effect [7].

In the first section of this chapter, we will briefly discuss the three-step model for gas-phase HHG and introduce the generalized three-step model proposed by Vampa *et al.* in details for the solid-phase HHG. Also, the actual procedures for the calculations are explicitly shown. In the second section, the adaptation of the model to incorporate Umklapp scattering is introduced, together with its implementation.

3.1 Semi-classical Model for the HHG in Gases and Solids

The HHGs from gas systems have been well-studied by the semi-classical model known as the three-step model [13, 12], and attempts to generalize the model to the HHG in solid systems has also been made over the years [**yue˙imperfect˙2020**, 4, 5, 7]. Here we will briefly introduce the three-step model and then describe one of the important generalization proposed by Vampa *et al.* from gaseous to solid systems [4].

The three-step model, as its name suggests, describes the HHG in a gas system as three distinctive steps:

- Ionization of a molecule by the laser, creating ions and effectively free electrons.
- Acceleration of the free electrons in vacuum, gaining energy from the laser.
- Recombination of the electrons with the ions, releasing the gained energy as high-energy photons.

In the first step, a high-intensity laser shining on gas molecules (generally inert gas mono-atomic molecules like He) in a gas chamber produces ionized molecules and ionized electrons. These electrons responsible for the HHG could be effectively seen as free electrons as they are very far away from the ionized parent molecule and thereby unaffected by the attractive force of the ions. To be more precise, the travel distances of these electrons are much larger than the length scale of the molecule so the laser force dominates the motion of the electrons. As for the ionized molecule, it is considered stationary compared to the motion of the ionized electrons during the whole process of the HHG due to its much-larger mass. In the second step, the ionized electron now is driven by the external laser and move in place far from the ionized parent molecule. The motion of the electron at this stage can be accurately captured by classical mechanics simply with a free electron accelerated by the laser. The electron gains energy from the laser and accumulates it in terms of its kinetic energy. Finally, in the third step, the force of the oscillating laser changes its direction and pushes the electron back to the ionized parent molecule. If the electron recombines with the parent ion, it releases its high kinetic energy by emitting a high-energy photon. This completes one cycle of the HHG in a gas system.

The most important consequence of the three-step model is that it gives the whole process of the gas-phase HHG a very simple physical picture. One could intuitively estimate the change of the HHG when the laser is altered by the classical mechanics in the second step instead of complicate quantum dynamics. Furthermore, by simulating the classical trajectories of the model and compare the signals from experiments or quantum simulations, one could analyze the source of the HHG and distinguish the major contributor of the process. This analysis is then the time-frequency analysis which we have already discussed about in Chapter 2.1.3. In addition to the simple picture, the model also allows for prediction of the cutoff energy U_c of the corresponding power spectrum:

$$U_c = I_p + 3.17 U_p \tag{3.1}$$

where I_p is the ionization potential and $U_p = \frac{q^2 F_0^2}{4M\omega_0^2}$ is the ponderomotive energy with F_0 and ω_0 the electric field amplitude and angular frequency of the laser, respectively. Although the actual value of the cutoff energy could deviate from Eq. 3.1, its quadratic dependence on electric field amplitude (through U_p) is indeed in accordance with experiments for gas-phase targets. This ability to estimate the cutoff energy is crucial for developing applications based on the HHG.

The very success of the three-step model in gas systems inspires the adaption of the model to the HHG in solid systems. And one of the very important adaptation is made by Vampa *et al.* through the incorporation of the band structure[4]. In the second step of the three-step model, the motion of a free electron driven by a laser can be equivalently treated as an electron resides in a parabolic band and move under the influence of the laser. For solid-phase HHG, the idea of this parabolic band is extended to the actual band structure of the solid system. The generalized three-step model describes the HHG in solid systems by the following three characteristic steps:

- Excitation of an electron from a valence band to a conduction band, creating an electron-hole pair.
- Acceleration of the electron-hole pair by the laser force, gaining energy prescribed by the band structure.
- Recombination of the electron-hole pair, emitting a photon with energy of the band energy difference.

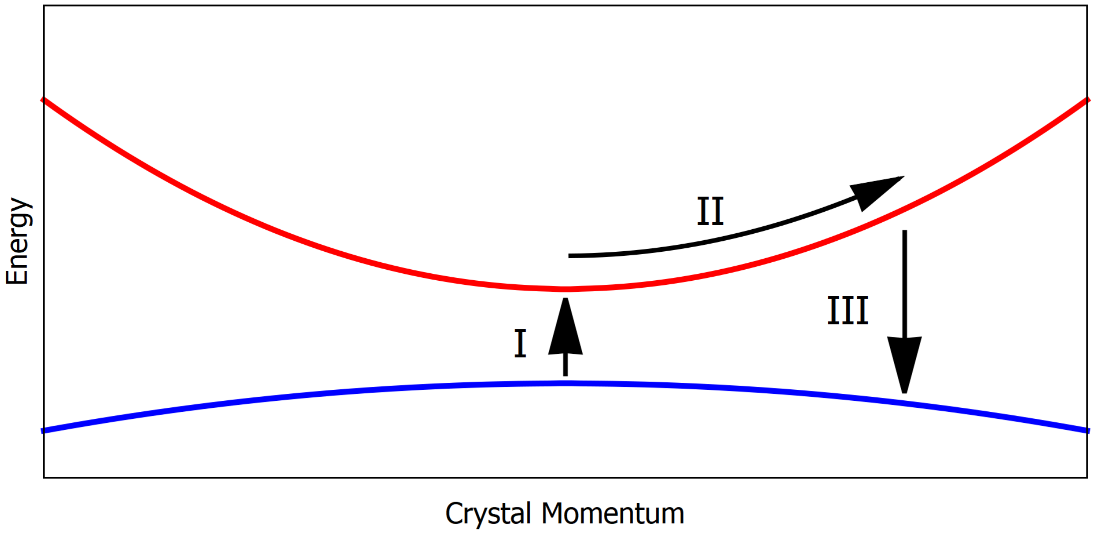

Figure 3.1: A schematic illustration for the generalized three-step model. The blue and red curves describe a valence band and a conduction band. The steps of excitation, acceleration, and recombination are marked by I, II and III, respectively.

These three steps are illustrated schematically in Fig. 3.1. For the first step, laser excites an electron from the top of a valence band to the bottom of a conduction band and an electron-hole pair is created, as shown by the process I in Fig. 3.1. In the real space, the electron and the hole are assumed to be in the same position at this instance. In the second step (process II in Fig. 3.1), the electron and the hole will be driven by the laser and move in $\boldsymbol{k}$-space according to the acceleration theorem with their crystal momentum over time being $\boldsymbol{K}(t)$. In the real space, the electron and the hole also propagate with their instantaneous velocity specified by the corresponding group velocity $v_n^g(\boldsymbol{k}) = \frac{1}{\hbar}\nabla_{\boldsymbol{k}} E_{n\boldsymbol{k}}$, $(n \in \{c, \nu\})$. For the final step, during the motion of the electron and the hole, they are considered to collide with each other and recombine if they move to the same position in real space. The electron in the conduction band then drops down to the valence band as shown in process III of Fig. 3.1 and releases its extra energy, namely the energy difference between the two bands, by creating a photon of that energy. These three steps complete a cycle of photon emission for solid-phase HHG.

Now we will explicitly show the procedures for implementing the three-step model for solid-phase HHG. The description here will be limited to a one-dimensional system since the semi-classical model for both of the quantum models described in the previous chapter effectively reduces to such a one-dimensional model. In addition, we also consider only the solid systems of direct band gap with its band gap locates at Γ point $(k = 0)$ and has zero group velocity at this point.

We should first define the physical quantities involved in the calculation. After an electron is excited by a laser, or equivalently an electron-hole pair is created, at time t_{ex}, we can calculate the relative position between the electron and the hole

$x(t) = x_e(t) - x_h(t)$ where $x_e(t)$ and $x_h(t)$ are the displacement of the electron and the hole, respectively. Note that the relative velocity of the electron and the hole $v(t) = \frac{dx(t)}{dt}$ is equivalent to their corresponding relative group velocity, namely $v(t;t_{ex}) = v_c^g(K(t;t_{ex})) - v_\nu^g(K(t;t_{ex}))$ where $K(t;t_{ex})$ is the displacement in crystal momentum for the electron-hole pair created at time t_{ex}:

$$K(t;t_{ex}) = -\frac{q}{\hbar}[A(t) - A(t_{ex})] \quad , \quad t \geq t_{ex}. \tag{3.2}$$

The calculation of the semi-classical model is carried out by the following procedures:

1. Choose an excitation time t_{ex} in the duration of the laser pulse.
2. Set up the initial condition in real space: $x(t = e_{ex}) = 0$ and $v(t = t_{ex}) = 0$.
3. Calculate the trajectory in the real space by one time step according to $x(t) = \int_{t_{ex}}^{t} v(t';t_{ex})dt'$.
4. If $x(t_r) = 0$ at certain time t_r, a recombination has occurred. The time is then designated as recombination time t_r.
5. Calculate the energy of emitted photon $\hbar\omega$ from this recombination by:

$$\hbar\omega = E_{cK(t_r;t_{ex})} - E_{\nu K(t_r;t_{ex})}. \tag{3.3}$$

6. Go back to step 3 and repeat for $x(t)$ at another time step until reaching the end of the pulse.
7. Go back to the first step and repeat with a new excitation time t'_{ex} until the excitation time reaches the end of the pulse.

The numerical calculation of $x(t)$ is carried out by Runge-Kutta method to the 4th order with time step Δt_{RK}. Also, the deterministic condition $x(t_r) = 0$ is substituted by the condition $x(t_r - \Delta t_{RK}) \times x(t_r + \Delta t_{RK}) \leq 0$ because absolute zero is unattainable in the numerical calculation. Note that with the substituted condition the program may fail to detect a recombination when the trajectory $x(t)$ just touches the time axis in the $x - t$ plane without passing it. This kind of scenario could be reduced by using a smaller Δt_{RK}. As a result, when checking the convergence of the time step, one should make sure not only the trajectory $x(t) = \int_{t_{ex}}^{t} v(t';t_{ex})dt'$ but also the condition $x(t_r) = 0$ reach convergence.

3.2 Semi-classical Model with Umklapp Scattering

Despite the direct analogy between the three-step model and the generalized one from gas systems to solid systems, there are many mechanisms not included in the generalized three-step model. One of them is the scattering between electrons and the lattice (sea of positively-charged ions). In the second step of the generalized three-step model, an electron is treated as an effectively-free electron driven by a laser and moves in the energy landscape, namely energy dispersion, formed according to the lattice potential. That is, a parabolic energy dispersion meant for a free electron is distorted to a complicate band structure to reflect the energy structure created by the lattice force. And this energy structure is taken in the semi-classical model to account for the force of the lattice implicitly so as to treat the electron as an effectively-free particle only subjected to the force of the external laser. As a result, this effectively-free electron picture in the second step of the generalized three-step model ignores any scattering with the lattice.

The neglect of such scattering could be questionable as it might make a difference for the solid-phase HHG. Under a typically setting for generating high-order photons in a solid system, electron-hole pairs responsible for the light emission would generally travel a distance of several lattice cells. Therefore, one would expect the electron-hole pairs have chances to scatter with some ions during the process. If such scattering does occur, the scattered electron-hole pair should have quite different speed and direction compared to those before the scattering. This suggests the trajectory of the electron-hole pair would be altered to a great extent, leading to a modified chance of recombination and photon emission in the future. As a consequence, it is natural to think the HHG power spectrum would be altered by the scattering in a crystal.

The scattering could be integrated into the generalized three-step model by a small modification in the second step. We will demonstrate this here by first looking at the scattering process in the $\boldsymbol{k}$-space. In principle, as an electron passes a point, which is addressed as a scattering point in our context, in a band where a neighboring band has very similar or even the same energy, the electron would have chances to move to this neighboring band by shifting its crystal momentum by a reciprocal lattice vector. This process is typically known as Bragg scattering or Umklapp scattering. In Fig. 3.2, such a process is illustrated with a conduction band (solid curve) and the shifted ones (dotted curves) of a one-dimensional system. Note that the scattering points for this specific band structure is found at the cross points of the band and the shifted ones. Before the scattering, an electron driven by a laser happens to be moving toward a scattering point as indicated by the process I in Fig. 3.2. After passing the scattering point, there are two possible paths: the non-scattered path and the scattered path, which are represented by the process II and II' in Fig. 3.2, respectively. The idea and the effect of the scattering would become more clear when we observe the two different paths in the real-space. For path II, the velocity of the electron will change continuously with time so the corresponding trajectory $x_e(t)$ will be a smooth curve without abrupt bending. On the other hand, for path II' the discontinuous group velocity of the electron when going from the conduction band to the shifted conduction band leads to a abrupt bending in $x_e(t)$ at the time of scattering. The trajectory will not look smooth due to this scattering. The behavior of the electron of the path II' then looks like a classical particle hitting an obstacle and scattered off. This reestablishes the familiar idea of scattering. From this example in one-dimensional system, it is clear that we need to consider not only the conventional non-scattered path but also the scattered path in order to take account for the effect of Umklapp scattering. Therefore, we can incorporate Umklapp scattering into

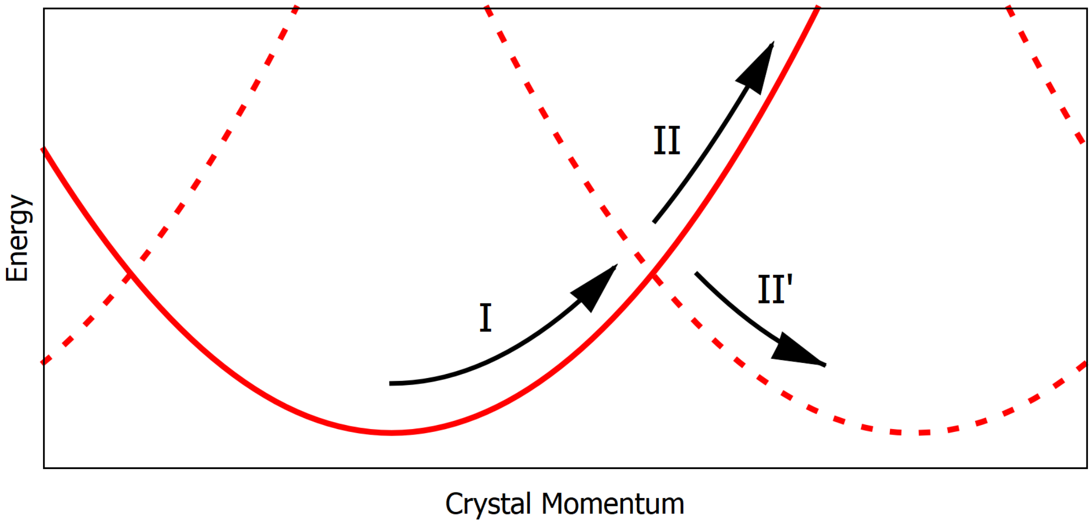

Figure 3.2: A sketch for the two possible paths for an electron which undergoes Umklapp scattering in the crystal-momentum space. The process I indicates an electron moving towards the scattering point located at zone boundary. The process II and II' describe the non-scattered and scattered paths, respectively.

the generalized three-step model by creating a scattered trajectory whenever a scattering point is traveled through by an electron-hole pair. In other words, in the second step of the generalized three-step model, a trajectory will branch into two trajectories, one for the non-scattered and the other for the scattered, at the time of scattering.

In summary, our semi-classical model with Umklapp scattering describes the HHG in solid systems by the following three steps:

- Excitation of an electron from a valence band to a conduction band, creating an electron-hole pair.
- Acceleration of the electron-hole pair by the laser force, gaining energy prescribed by the band structure. The trajectory of the pair branches into one scattered trajectory and one non-scattered trajectory if a scattering point is passed.
- Recombination of the electron-hole pair, emitting a photon with energy of the band energy difference.

Note that step one and three remain exactly the same as those in the generalized three-step model, and step two is modified by the addition of trajectory branching. We will see in Chapter 4 our model can reproduce the quantum result and describes the structure of multiple plateaus, which is unavailable in the three-step model without scattering.

3.2.1 Implementation of the Model with Umklapp Scattering

The implementation of the semi-classical model with Umklapp scattering deserves a bit more attentions because of the possible exponential growth of branching trajectories. Notice that the number of trajectories is doubled every time an electron passes through a scattering point and it depends sensitively on the setup of the laser pulse. For example, increasing laser intensity would lead to larger span in the crystal-momentum space for an electron-hole pair and enable the pair to reach more scattering points. Additionally, using a longer pulse with more optical cycle will also increase the repetition of an electron-hole pair passing a scattering point. Due to the large number of trajectories from the complex scattering process, it would not be computationally efficient to fully simulate the new semi-classical model to the end of the pulse.

A simple solution is to stop branching or just terminate the simulation of a trajectory once it becomes less important. For example, we can disregard scattered trajectories if the current trajectory has already undergone Umklapp scattering for several times, because in general a multi-scattered electron-hole pair are very unlikely to meet and recombine in the future. In practice, this is carried out by stopping branching at scattering points for doubly-scattered trajectories. Also, we can neglect the photon emission beyond first recombination due to the nature of quantum spreading of the electron-hole wave packets in real-space. This allows us to terminate a trajectory at the time of first recombination.

The implementation of the model could be listed in the following steps:

1. Choose an excitation time t_{ex} in the duration of the laser pulse.
2. Set up the initial condition in real space: $x(t = t_{ex}) = 0$ and $v(t = t_{ex}) = 0$.
3. Calculate the trajectory in the real space by one time step according to $x(t) = \int_{t_{ex}}^{t} v(t'; t_{ex})dt'$.
4. In each time step, designate a recombination event and recombination time $t = t_r$ if the condition $x(t) = 0$ is satisfied. Then:
    - Calculate the energy $\hbar\omega$ of emitted photon by $\hbar\omega = E_{cK(t_r;t_{ex})} - E_{\nu K(t_r;t_{ex})}$.
    - Jump to the last step.
5. In each time step, designate a scattering event and scattering time t_s if the condition $K(t; t_{ex}) - k_s = 0$, where k_s is one of the scattering points, is satisfied. Then:
    - Create a scattered trajectory if the total number of scattering is no more than two.
    - Stay with the current trajectory if the total number of scattering is larger than two.
6. Go back to step 3 and repeat for $x(t)$ at another time step until reaching the end of the pulse.

7. Go back to the first step and repeat with a new excitation time t'_{ex} until the excitation time reaches the end of the pulse.

For the same reason in the previous section, the deterministic condition $K(t; t_{ex}) - k_s = 0$ is substituted by the condition $[K(t - \Delta t_{RK}; t_{ex}) - k_s] \times [K(t + \Delta t_{RK}; t_{ex}) - k_s] \leq 0$. Again, this substituted condition is sensitive to the time step Δt_{RK} and its convergence should be verified.

Chapter 4

The Effects of Scattering and a Static Field on the HHG in Solids

We study the dynamics of solid-phase HHG with the effects of scattering and a static field through the comparison between quantum and semi-classical models. As data from experiments or *ab initio* quantum simulations is generally a result of intricate dynamics, it is very difficult to delineate the mechanisms involved. In this study, to clarify a connection between the HHG in the energy range of interest and the external laser, we employ simplified quantum models, namely the one-dimensional quantum model and the parabolic two-band model introduced in Chapter 2. Furthermore, in order to develop microscopic insight into the phenomena, we follow the conventional approach in the community of HHG studies, namely a comparison between quantum and semi-classical models. To be more precise, we will use the semi-classical models to retrace the HHG signal from quantum simulations and establish its characteristics in the aspect of the scattering and a static field.

In the investigation of scattering effects, we begin by briefly looking at the different dependence of the cutoff energy on the electric field amplitude of the external laser between a parabolic band and a non-parabolic band, which is the Kane's band in our case, within the generalized three-step model. The empirical formula of the cutoff for the non-parabolic band is also proposed, which could serve as a quick estimation for experiments on solids with band structure in the form of the Kane's band. With a basic understanding of the behavior of the cutoff, we then move to the main investigation. Quantum simulations based on the one-dimensional quantum model using a model potential formulated in Sec. 2.1 are performed and their quantum data is compared with the predictions from the generalized three-step model with Umklapp scattering described in Sec. 3.2. Multiple plateaus are observed in quantum simulations, and the semi-classical model successfully captures the cutoff energy for each plateau. In addition, with the help of the time-frequency analysis, we show that the major contribution to each plateau comes from the recombination of electron-hole pairs undergo a different number of scattering. Finally, we present a semi-classical approach extended by using the concept of the mean-free path to incorporate the general scattering effects in solid.

From this semi-classical model, the wavelength independence of the cutoff energy in solid-phase HHG could be reproduced.

For the effect of a static field, we use the parabolic two-band model derived in Sec. 2.2 and compare the results with the predictions from the generalized three-step model in Sec. 3.1. It is observed that the cutoff energy of the HHG power spectrum splits into two by the static field. The two cutoffs depend on the static electric field amplitude in the opposite way: one increases and the other decreases with the increasing static field. However, the increasing cutoff will saturate at maximum energy at a certain electric field amplitude and starts to decrease with the stronger static field. From the semi-classical model, it could be shown that the splitting of the cutoff energy is a result of broken symmetry induced by the static field, which removes the two-fold degeneracy of trajectories for the electron-hole pairs.

This chapter consists of two major parts corresponding to the two subjects mentioned above. In section 4.1, we present our studies on the effect of Umklapp scattering on the solid-phase HHG. Additionally, the alternative approach to general scattering effects in solids is also presented at the end of this section. In section 4.2, the effect of a static field on solid-phase HHG are demonstrated and discussed. In both of the two sections, the setup of the related models and numerical parameters are also given at the start of each section.

4.1 The Effect of Umklapp Scattering on Solid HHG

4.1.1 Setup of the Quantum System under a Model Potential

We would specify the actual numerical setup of the quantum system for studying scattering effects and briefly discuss the substitution of the band structure in the semi-classical calculation. In quantum simulations, the model potential $V(x)$ of the Matthieu-type in the following form are utilized:

$$V(x) = V_0 \cos(\frac{2\pi}{L}x) \tag{4.1}$$

with $V_0 = 0.37$ a.u. and $L = 8$ a.u. These specific values are taken from the previous study [7] since we will make several comparisons with their results. The corresponding band structure is computed by diagonalizing the Hamiltonian and yields a band gap of $\epsilon_g = 4.18$ eV and reduced electron-hole effective mass of $\mu = 0.083$ electron mass. The band structure is shown in Fig. 4.1 (a). For simplicity, in the calculation of semi-classical models, this numerically solved band structure is substituted by the Kane's band to reduce the complication induced by tunneling between bands. Notice that, in principle, one can employ the numerically evaluated band structure shown in Fig. 4.1 (a), by taking account of the quantum transitions between different bands with a non-zero energy gap. To comply with the definition of non-scattered trajectories discussed in Chapter 3 and neglect the complication in the states due to tunneling processes, we substitute the band structure solved numerically from the potential in Eq. 4.1 with the Kane's band, which always has zero energy gap between the current band and shifted bands. As a result, the effect of tunneling processes could be neglected in the semi-classical model. The comparison between the electron-hole band structure $E_{Diff}(k) = E_{ck} - E_{\nu k}$ solved from the quantum system and the Kane's band is shown in Fig 4.1 (b). The Kane's band takes the form:

$$\epsilon_{Kane}(k) = \epsilon_g \sqrt{1 + \frac{|k|^2}{\mu \epsilon_g}} \tag{4.2}$$

with the band gap energy ϵ_g and the reduced electron-hole effective mass μ taking the values directly from the numerically solved band structure in Fig. 4.1 (a).

As for the laser pulse used in the simulations, its vector potential $A(t)$ has the following form:

$$A(t) = \frac{F_0}{\omega_0} \sin^4\left(\frac{\pi}{\tau} t\right) \sin(\omega_0 t) \tag{4.3}$$

and 0 if $t \notin [0, \tau]$. The photon energy is set to $\hbar\omega_0 = 387$ meV and the pulse duration is chosen to be $\tau = 96.1$ fs. We will investigate the electron dynamics by changing the peak amplitude F_0.

For the numerical simulations of the one-dimensional quantum system, the number of grid points in a unit cell N_r is set to 30 and the number of grid points in the first Brillouin zone N_k is set to 352. In the time propagation of the Schrödigner's equation, the time step Δt is set to 1 attosecond. As for the semi-classical calculations, the total number of excitation time t_{ex}considered within the full pulse duration is set to 3000 and the time step Δt_{RK} is set to 0.01 fs.

4.1.2 The Cutoff Energy Dependence in the Semi-classical Models

We first examine the difference in the cutoff energy dependence on the electric field amplitude between a conventional parabolic band and the Kane's band using the generalized three-step model. A general one-dimensional parabolic band ϵ_{Para} takes the form:

$$\epsilon_{Para}(k) = \frac{|k|^2}{2\mu} + \epsilon_g \tag{4.4}$$

where μ and ϵ_g are the reduced effective mass of an electron-hole pair and band gap. By employing the same effective electron-hole mass and band gap like those in the Kane's band and perform the generalized three-step model described in Chapter 3, one could obtain the cutoff energy U_c for various electric field amplitude F_0. Their relation is described in Fig. 4.2. Note that the square root of ponderomotive energy is proportional to F_0. Also, both of the axes are in the dimension-less form through the normalization with band gap ϵ_g.

From Fig. 4.2, it is clear that in the weak-field region (U_p/ϵ_g being around 0 to 1) the cutoff energy from either the parabolic band or the Kane's band is essentially the

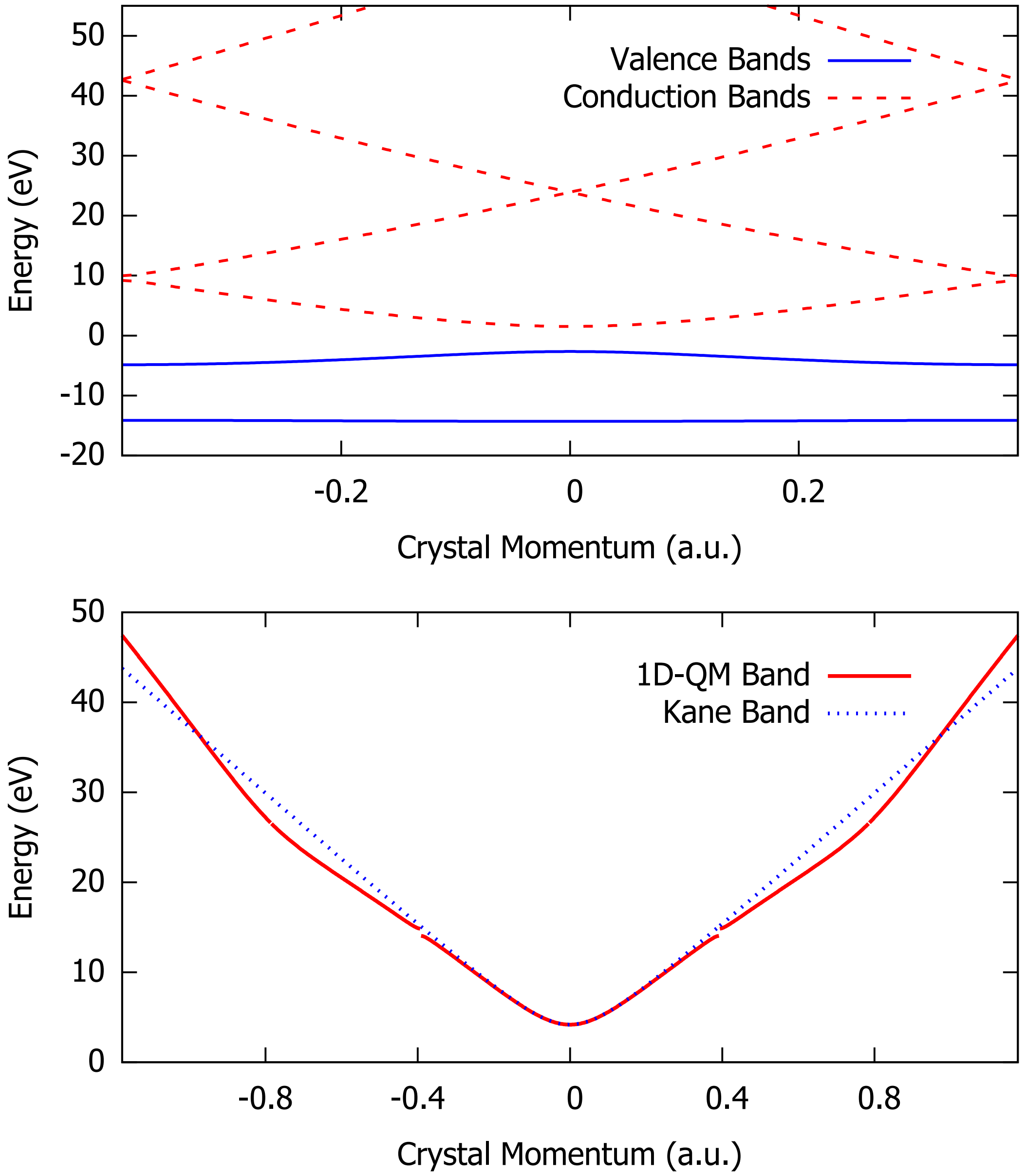

Figure 4.1: (a) Electronic band structure of the one-dimensional model with the lattice potential described in Eq. 4.1 is shown. The valence bands and conduction bands are described by the blue-solid lines and the red-dotted lines, respectively. (b) Comparison of the electron-hole band (red-solid lines) and the Kane's band (blue-dotted lines). This figure is taken directly from our publication [6].

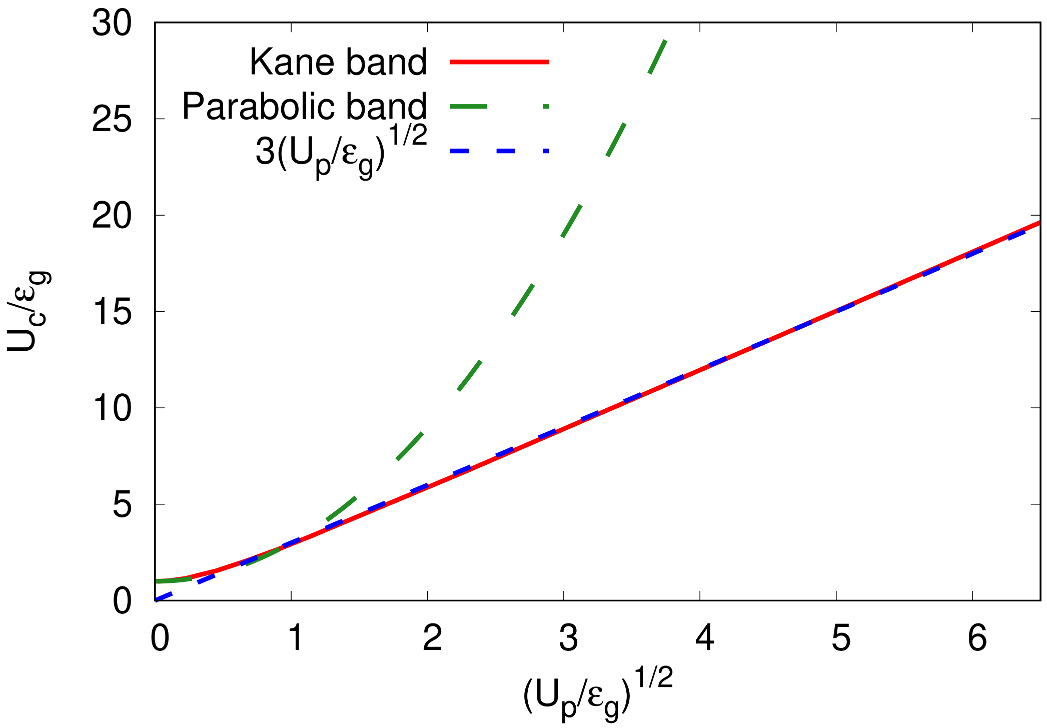

Figure 4.2: Cutoff energy U_c calculated from the generalized three-step model versus the square root of ponderomotive energy $U_p^{\frac{1}{2}}$. Both of the energy is normalized with respect to the band gap. The semi-classical predictions for the parabolic band and the Kane's band are shown as green-dashed line and red-solid line, respectively. The analytical expression for the strong-field approximation, $U_c/\epsilon_g = 3(U_p/\epsilon_g)^{1/2}$, is described as the blue-dotted line. This figure is taken from our publication [6].

same. This is of no surprise as the Kane's band approaches the parabolic band near Γ point. That is,

$$\lim_{k\to 0} \epsilon_{Kane}(k) = \epsilon_{Para}(k). \tag{4.5}$$

On the other hand, we see huge differences in the strong-field region ($U_p/\epsilon_g \geq 3$) where the parabolic band shows quadratic dependence on electric field amplitude while the Kane's band yields linear dependence. The quadratic dependence of the cutoff energy for the parabolic band can be understood by a direct analogy with the gas-phase HHG so the cutoff energy would admit the form:

$$U_c^{Para} = \epsilon_g + 3.17U_p. \tag{4.6}$$

To obtain a similar and simple expression for the case of the Kane's band, we fit the cutoff energy predicted from Kane's band in the strong-field region to a linear function and obtain the analytical expression:

$$U_c^{Kane} \approx 3\epsilon_g \sqrt{\frac{Up}{\epsilon_g}}. \tag{4.7}$$

This analytical expression is also shown in Fig. 4.2 as blue-dotted line. This analytical expression of cutoff energy is different from previous studies using linear bands, of which cutoff energy $U_c^{k-space}$ is estimated to have the expression

$$U_c^{k-space} = 4\epsilon_g \sqrt{\frac{Up}{\epsilon_g}} \tag{4.8}$$

which is larger than the cutoff energy in Eq. 4.7 by one-third. The difference is a result of different consideration in the semi-classical model: For Eq. 4.8 one consider only k-space trajectories, which allows for electron-hole recombination at any time; For Eq. 4.7 we consider not only k-space trajectories but also real-space trajectories, which adds additional constraint that an electron and a hole is allowed to recombine only when they are in the same place in the real space. This means the possible recombination energy from model considering both real-space and k-space trajectories is a subset of that considering only k-space trajectories. As a result, by construction the cutoff energy in Eq. 4.7 can only be smaller or equal to that in Eq. 4.8.

4.1.3 The HHG Spectrum from Quantum Simulations

Now we start to examine the effect of Umklapp scattering in HHG by observing the features in the HHG power spectrum. Fig. 4.3 shows the power spectrum from the one-dimensional quantum simulations under the electric field amplitude $F_0 = 0.165$ V/Å. Clearly, one could identify multiple plateaus with cutoffs locates at around 13, 28, 44, and 68 eV. This feature of multiple plateaus is also observed in previous theoretical studies, and described as the result of band-climbing [7].

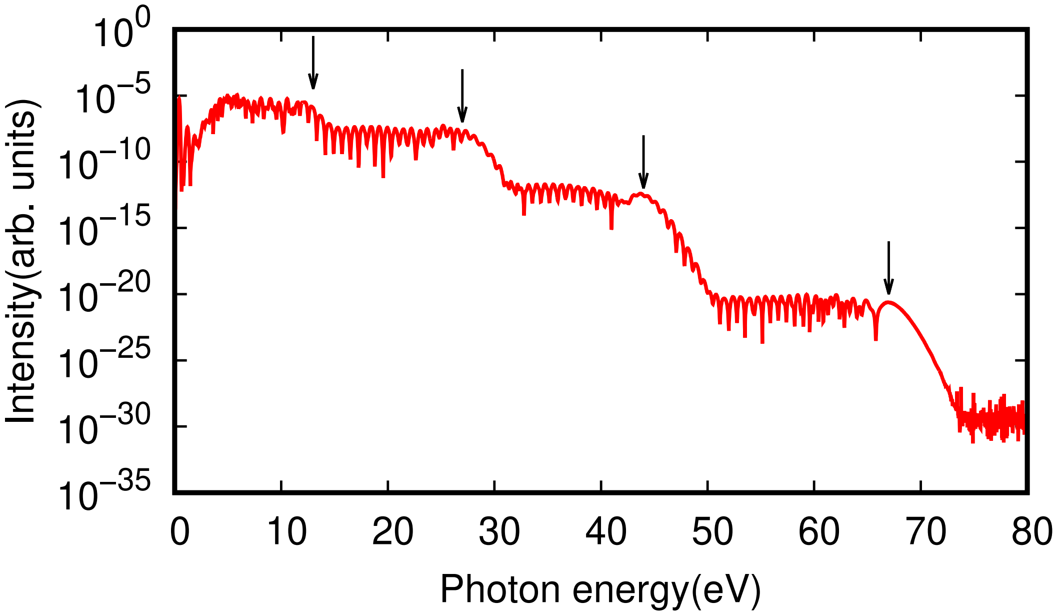

Figure 4.3: The power spectrum of HHGs from quantum simulations with the electric field amplitude $F_0 = 0.165$ V/Å. Several plateaus are visible and their corresponding cutoff energy is marked by black arrows around 13, 28, 44, and 68 eV. This figure is taken from our publication [6].

In Fig. 4.4, the power spectra of HHG are depicted as a function of electric field amplitude in the range of 0 to 0.25 V/Å. The cutoff energy calculated from the generalized three-step model with Umklapp scattering is also described in the same figure. Here we show the cutoff energy with respect to different numbers of scattering an electron-hole pair experienced before the recombination. The maximum energy emitted from an electron-hole pair undergoes zero, one, and two scattering processes are represented as solid-black, blue-dashed, and red-dotted lines, respectively. From Fig. 4.4, it is clear that the cutoff of the first plateau could be predicted by the conventional generalized three-step model. However, for the cutoff of the second and the third plateaus, they can only be captured by our generalized three-step model with Umklapp scattering. Additionally, the general agreement in the cutoff energy of higher plateaus between quantum simulations and our semi-classical model justifies the validity of our treatment to Umklapp scattering in the solid-phase HHG. The cutoff energy of higher plateaus (second and third) captured by our semi-classical model indicates that these plateaus are induced by Umklapp scattering processes. Our generalized three-step model with Umklapp scattering could be considered as a complementary model to the previously proposed band-climbing model in the sense that real-space trajectories are also incorporated [7].

4.1.4 Time-frequency Analysis

To further investigate the details of the HHG spectra and the validity of our semi-classical model with Umklapp scattering, we also perform time-frequency analysis, which is described in Chapter 2, for the signals from quantum simulations. The Gabor transformation, with a time window of which full width at half maximum is 1.78 fs, is applied to the current $J(t)$ from quantum simulations with the electric field amplitude $F_0 = 0.165$ V/Å. The result is described as the color map in Fig. 4.5, together with the predictions from our semi-classical model as the black dots. Each of the panels of Fig. 4.5 shows the contribution of electron-hole pairs of different numbers of scattering: Panel (a), (b), and (c) describe the emission energy and timing for electron-hole pairs with no scattering, single scattering, and double scattering, respectively.

In Fig. 4.5 (a) the electron-hole pairs undergo no scattering do not contribute to the second and third plateau. However, from Fig. 4.5 (b) and (c) singly-scattered and doubly-scattered electron-hole pairs have apparent contribution to the second plateau. Moreover, Fig. 4.5 (c) indicates doubly-scattered electron-hole pairs contribute to the third plateau. These results indicate that Umklapp scattering allows for higher energy emissions by opening up the tunneling channels to higher conduction bands. This again further confirms the scattering process is the origin of the formation of the high plateaus.

In addition, one could see that the quantum signals are reasonably reproduced by the semi-classical predictions. The information for actual emission timing and energy is a distinctive difference from the semi-classical model in previous studies [7] where electrons and holes recombine at any time. Note that the previous model considers only k-space trajectories and electrons and holes are assumed to be delocalized. Therefore these electron-hole pairs can recombine at any separation distance, resulting in photon

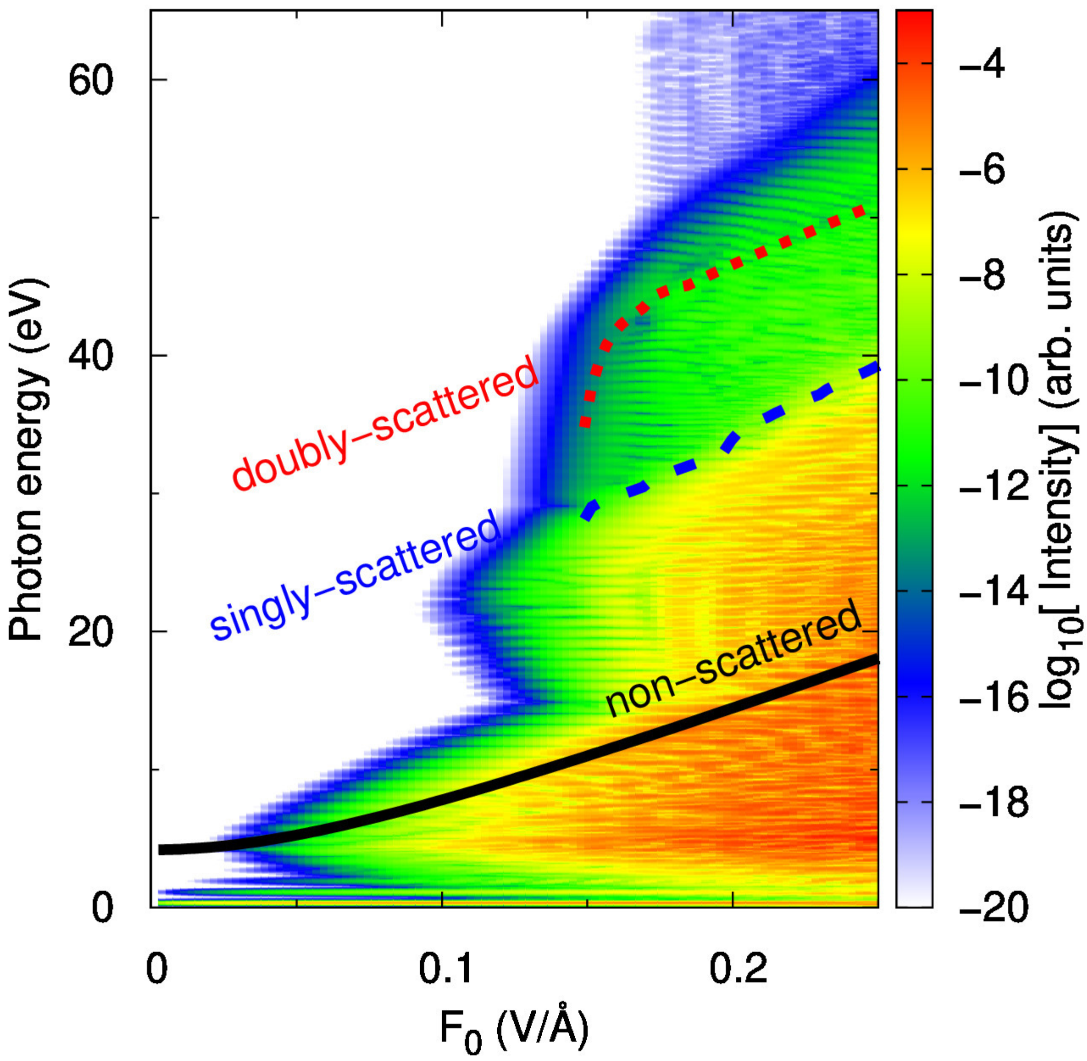

Figure 4.4: The color map shows the calculated HHG power spectra from the one-dimensional quantum simulations versus the electric field amplitude F_0 of the laser. The cutoff energy computed by our semi-classical model using the Kane's band is described as different lines: The cutoff from trajectories without scattering is shown as the black-solid line. The cutoff from trajectories with single scattering is described as the blue-dashed line. The cutoff from trajectories with double scattering is shown by the red-dotted line. This figure is taken from our publication [6].

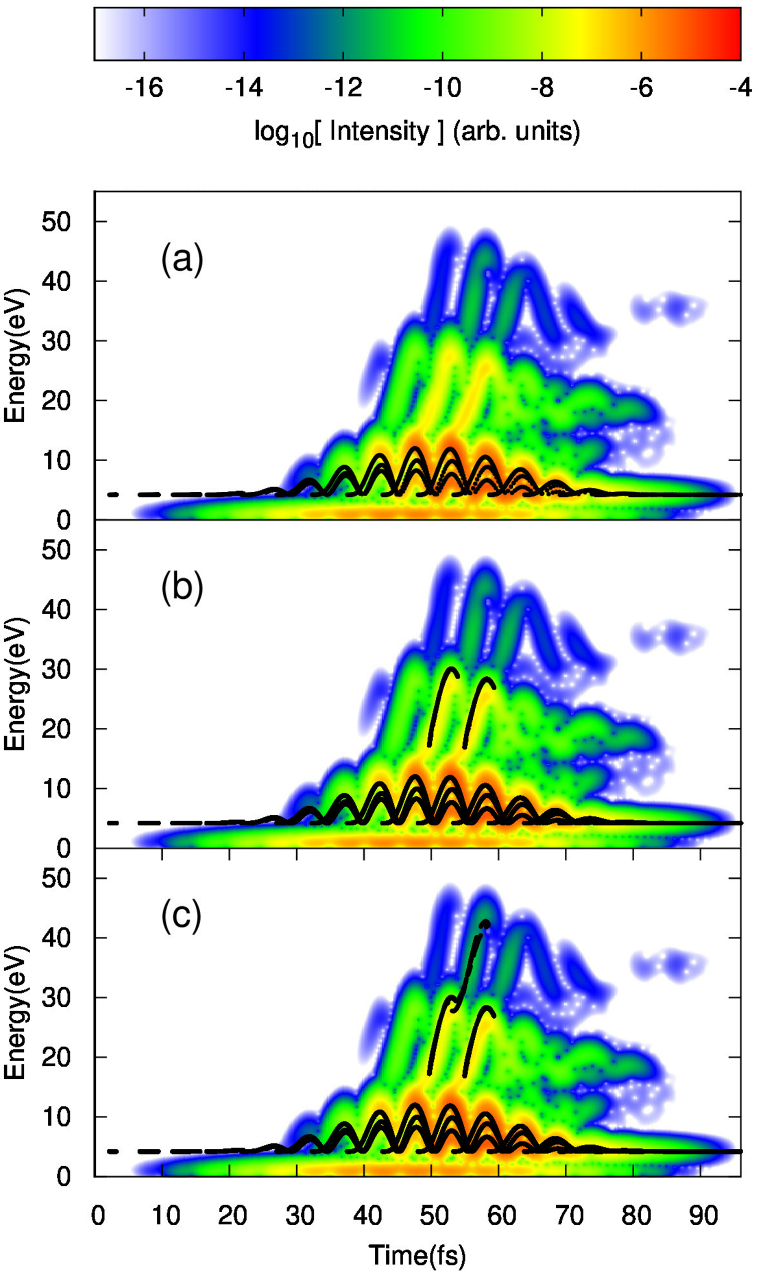

Figure 4.5: Time-frequency analysis of the HHG calculated from quantum simulations are shown as the color map. The emission energy and timing predicted from the generalized three-step model with Umklapp scattering are represented as black dots, and their contribution for no scattering, single scattering, and double scattering are indicated in panel (a), (b), and (c) respectively. This figure is taken from our publication [6].

emissions at any time. On the other hand, in our model which considers both real- and k-space trajectories, electrons and holes are treated like point particles(local). The recombination of an electron-hole pair is only allowed when they are right at the same place. And therefore photon emission only occurs at a certain time. Generally speaking, electrons and holes in the solids are not point particles localized to a point in both real and k space but are wave packets with finite spreading. The assumption of point particles in our model gives rise to the deviation between the quantum signal and the semi-classical predictions in Fig. 4.5. For example, the semi-classical prediction fails to capture the signals on the left side (around 40 to 50 fs) of the semi-classical predictions in the second plateau (around 15 to 35 eV).

We could further assess how local an electron-hole pair actually is by including the spreading of their wave-packets into the semi-classical model. This would allow for a quantitative measure of the spreading and verification of the assumption of point particles in the model. In addition to the examination of wave-packet spreading in real space, it is also worth investigating the spreading in k space. Within the semi-classical model it is assumed electrons are excited and tunnel to a conduction band only at the Γ point. This may not be realistic as, in principle, electrons in the region near the point could also become excited and tunnel to a conduction band. That is, electronic excitation is in general not localized at the Γ point but has a spreading near the point. As a quick summary, the finite spreading of the electron-hole wave packet in real space affects the constraint of the recombination for the pair, and the finite spreading of the tunneling region near the Γ point affects the excitation channels of the electron-hole pair.

The generalization of the semi-classical model for the spreading of electron-hole pairs in real and k space is straight-forward: For the spreading in real space, the condition for recombination in the semi-classical model is modified such that electrons and holes are allowed to recombine as long as they are within a specified distance $|\Delta x|$ instead of at exactly zero distance. As for the spreading in k space, the initial crystal momentum of an electron-hole pair now is not limited to the single Γ point but to a small region centered at the Γ point with a specified radius $|\Delta k|$. Beyond these modifications in each case, the semi-classical model remains unchanged.

In Fig. 4.6 the results from the semi-classical model with different constraints for recombination are shown: Recombination of an electron and a hole is allowed (a) only when they are at the same place in real space and (b) when their separation distance in real space is within 40 a.u. We could see that the relaxation for recombination constraint in the real space does not improve the semi-classical prediction qualitatively. This suggests the assumption that electrons and holes are like point particles works well in real space, at least for this specific quantum system. In Fig. 4.7, the semi-classical predictions for different excitation channels near Γ point are shown: In panel (a) excitation occurs exactly at the Γ point. In panel (b) excitation occurs within a radius of 0.1 a.u. centered at the Γ point. It is clear that the missing predictions on the left of semi-classical results in the second plateau mentioned earlier now appear. This indicates that non-zero spreading of excitation channels for electron-hole pairs in

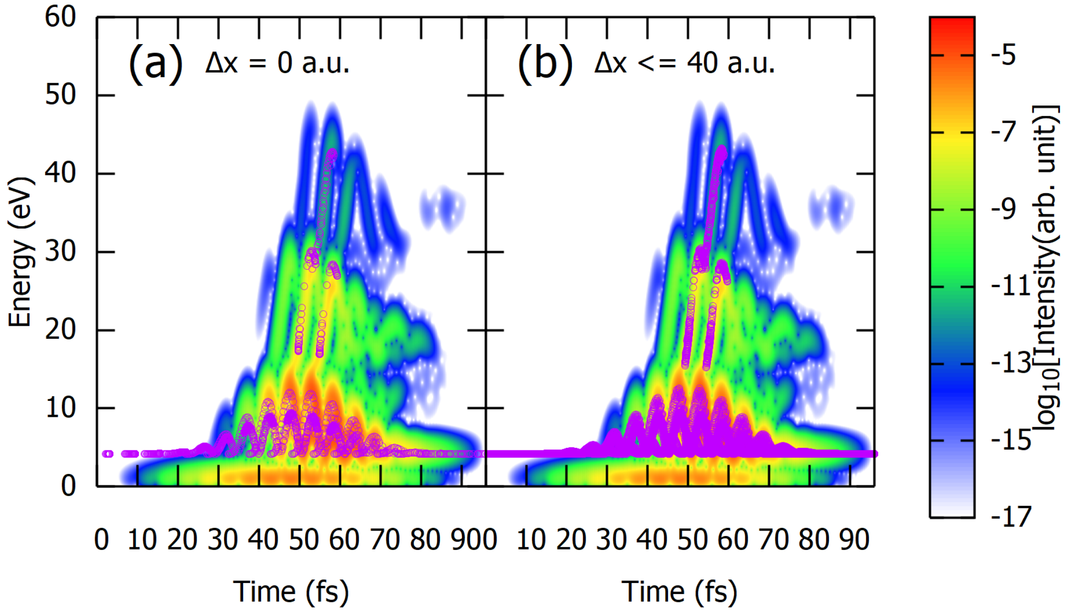

Figure 4.6: The comparison for semi-classical predictions for recombination occurring (a) at zero separation distance and (b) within a separation distance of 40 a.u. between an electron and a hole. The purple circles describe the semi-classical predictions and the color map describes the time-frequency analysis of HHG. The setup for quantum simulations is the same as Fig. 4.5.

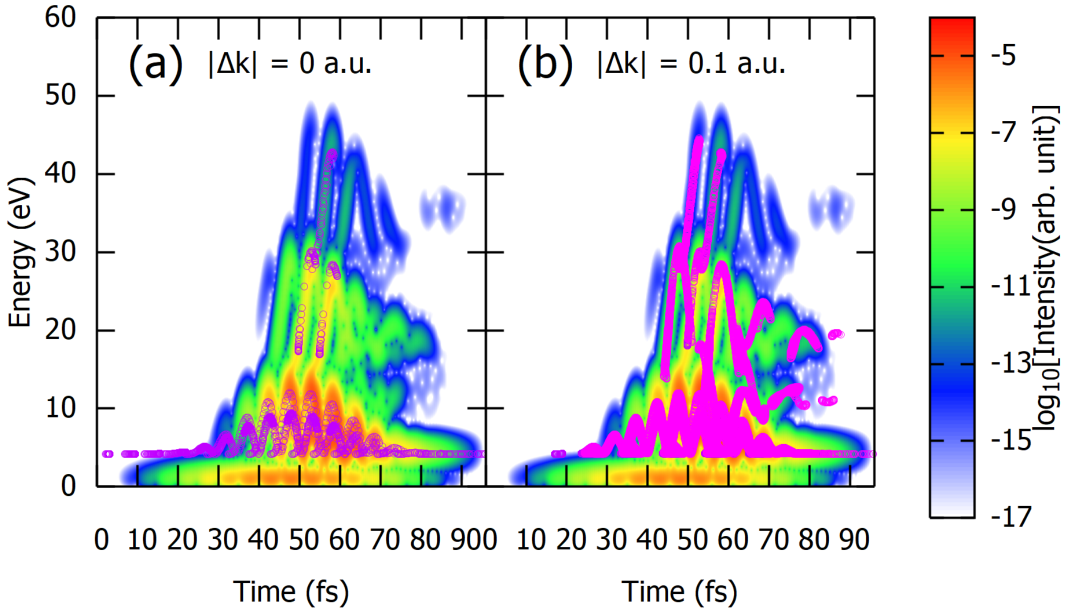

Figure 4.7: The comparison for semi-classical predictions for excitation occurring (a) at exactly Γ point and (b) in a region within 0.1 a.u. from Γ point. The purple circles describe the semi-classical predictions and the color map describes the time-frequency analysis of HHG. The setup for quantum simulations is the same as Fig. 4.5.

k space is important and should be taken into account when studying the dynamics of the solid-phase HHG.

4.1.5 Extension to General Scattering Effects in Solids

We have been studying Umklapp scattering based on the one-dimensional quantum simulations and found that Umklapp scattering plays an essential role in the solid-phase HHG. However, Umklapp scattering itself might not be enough in higher-dimensional systems to comprehensively describe the HHG in solids. In solid systems, an electron is not only subjected to Umklapp scattering but also a variety of other scattering mechanisms like scattering with impurity, defect, phonon, or other electrons. Generally speaking, it is very difficult to deal with these complicated scattering events microscopically. Furthermore, while there could only be forward- and backward-scattering in one-dimensional systems, electrons and holes might be scattered into many different angles in two- or three-dimensional systems, which effectively suppresses the recombination of the pairs in the future.

Here we propose a very simple modification inspired by the concept of mean-free-path to the generalized three-step model in order to account for the effects of general scattering in solid systems. The idea is quite simple: If an electron-hole pair has traveled a long distance in a crystal, it is in general more likely to be scattered, and its chance to recombine in the future would be small. To be more accurate, we made two assumptions. First, it is assumed that the chance of an electron-hole pair undergoing a general scattering event in solids would depend on the distance the pair has traveled. This is reasonable because a large travel distance typically indicates the electron-hole pair has explored a larger volume of the lattice. If the source of scatterings like impurity or defect is evenly distributed in a crystal, the pair with larger volume explored would have a higher chance to encounter a scattering event. Second, we assume the scattered electron-hole pair would have no chance to recombine after the scattering. This supposition should hold as a pair with scattering would have abrupt changes in trajectory so the electron and the hole would have a difficult time meeting each other. Not only that, even if they do eventually meet and emit a photon, this photon emission would be very unlikely to be coherent with photon emission from other electron-hole pairs as the emission timing is overwhelmed by scattering events. Therefore, the photon emission from electron-hole pairs undergoes a general scattering should be of little significance for the final macroscopic HHG.

One thing worth mentioning here is that one should not also apply the conclusion of the second assumption here to Umklapp scattering as they are intrinsically different in the sense of coherence. Note that Umklapp scattering discussed in Sec. 3.2 is triggered by the electron-hole pair passing a scattering point in the crystal-momentum space, and the motion of the pair is controlled by the external laser. This means the timing of Umklapp scattering will be controlled by the laser so the photon emissions for these scattered pairs will be coherent with the laser and thereby could be observed in the macroscopic HHG power spectrum.

For the actual implementation of the concept into the generalized three-step model, we first define the absolute travel length $l(t)$:

$$l(t) = \int_{t_{ex}}^{t} |v(t')| dt' \tag{4.9}$$

where $v(t)$ is the relative velocity of the electron-hole pair at time t. Also, we will set up a threshold of the absolute travel length l_{MFP}. In the second step of the generalized three-step model, we keep track of the absolute travel length $l(t)$ of an electron-hole pair over time. Once this length becomes larger than the threshold l_{MFP}, the electron-hole pair is considered to encounter a general scattering event and becomes scattered. The recombination and photon emission of this electron-hole pair after the scattering are then neglected (namely its trajectory is terminated). In practice, the values of l_{MFP} will be set to some tens of the lattice constant. We can see that, just like the mean-free path is the travel distance before any interaction, the threshold of the absolute travel length l_{MFP} is the travel distance before any scattering event. This is why our approach here is considered an analogy to the mean-free-path approximation.

The cutoff energy dependence on the wavelength of the laser field with l_{MFP} being 3, 5, and 7 nm are described in Fig. 4.8 as red-dashed, green-dotted, and blue-dashed-and-dotted curves. Also in the same figure, the result without scattering is shown by the black-solid curve, which is equivalent to the case of $l_{MFP} = \infty$. From Fig. 4.8, one

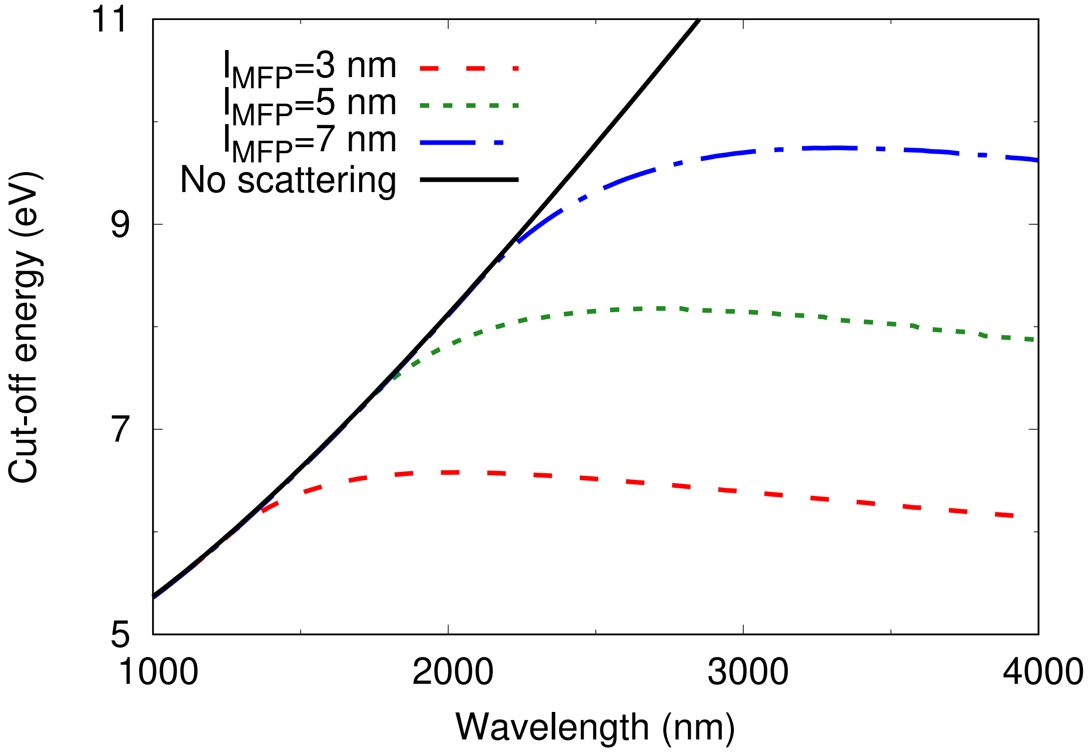

Figure 4.8: Wavelength dependence of the cutoff energy of HHG from the generalized three-step model with general scattering effects. The cutoff energy with l_{MFP} equal to 3, 5, and 7 nm are described as red-dashed, green-dotted, and blue-dashed-and-dotted lines. The result without scattering is also depicted as the black-solid line. The wavelength independence can be clearly observed in cases with finite l_{MFP}. This figure is taken from our publication [6].

can see that in the long-wavelength region the cutoff energy from the model with general scattering becomes essentially a flat line, suggesting that it is effectively independent of the wavelength of the laser. Within our model here, this wavelength independence could be understood as that electron-hole pairs having long travel enabled by long-wavelength laser are more likely to be scattered during the acceleration process. As recombination from these long-travel electron-hole pairs, which typically carry higher energy due to longer acceleration time, are suppressed by scattering, the highest emission energy gradually saturates with increased laser wavelength [6]. Such wavelength independence had already been observed in previous experimental studies. The reproduction of this feature also suggests the suppression of recombination resulted from general scattering effects in solids plays an important role in wavelength independence of the solid-phase HHG.

4.2 The Effect of a Static Electric Field on Solid HHG

4.2.1 Setup of the Parabolic Two-band System

For the the parabolic two-band model introduced in Sec. 2.2. The band gap E_g and reduced effective mass M_r of the parabolic band are set to 9 eV and 0.4 electron mass, respectively. These values are chosen specifically such that the resulting system gives clean spectra in time-frequency analysis. As for the laser, the electric field $\boldsymbol{E}(t)$ considered here is in the following form (with $\hat{z}$ being the unit vector in z direction):

$$\boldsymbol{E}(t) = \hat{z}E_0 \cos^4(\pi(\frac{t-\tau/2}{\tau}))\cos(\omega(t-\tau/2)) + \hat{z}E_s \tag{4.10}$$

with the oscillating amplitude $E_0 = 0.4$ V/Å, photon energy $\hbar\omega_0 = 0.5$ eV, and full pulse width $T = 60$ fs. The static amplitude E_s ranges from 0 to 0.4 V/Å. The electric field $\boldsymbol{E}(t)$ above is valid within the period $t \in [0, \tau]$ and is set to zero outside of the period.

For numerical simulations of the three-dimensional quantum system, the axis k_z, which is the corresponding axis of z axis in reciprocal space, is discretized with 4096 grid points. The axis k_r, which is the radial axis of k_z, is also discretized by 4096 grid points. The maximum crystal momentum in k_z and k_r direction are both set to 4 a.u. In the time propagation, the time step Δt is set to 0.08 a.u. and a total of 31200 time steps are propagated (total time is around 60.34 fs). As for the semi-classical calculations, the total number of trajectories within the full pulse duration is set to 3000 and the time step Δt_{RK} is set to 0.01 fs.

4.2.2 The HHG Spectrum under a Static Field

We will first examine the differences induced by a static field in a solid-phase HHG power spectrum. In Fig. 4.9, the spectra generated under different strength of the static field are shown. The results for static electric field E_s being 0, 0.04, 0.08, 0.12, 0.16, and 0.20 V/Å are described, respectively, as black, blue, light-blue, pink, red, and brown lines. From this figure, it is observed that, when the strength of the static field becomes stronger, the maximum emission energy for the HHG is also increased but the overall intensity with emission energy above band gap is lowered by the static field. Additionally, we perform time-frequency analysis to verify the applicability of the semi-classical model for the HHG under an additional static field. In the analysis, the Gabor transformation with a time window of which full width at half maximum is 1 fs is applied to the current obtained from quantum simulations. This result is given in Fig. 4.10, with the quantum result shown as the color map and semi-classical predictions as pink dots. The nice agreement between the results of quantum simulations and semi-classical predictions suggests the generalized three-step model is still applicable when a static field is appended to the system. As a result, we can facilitate the idea of classical trajectories to describe the dynamics of the HHG with a static field.

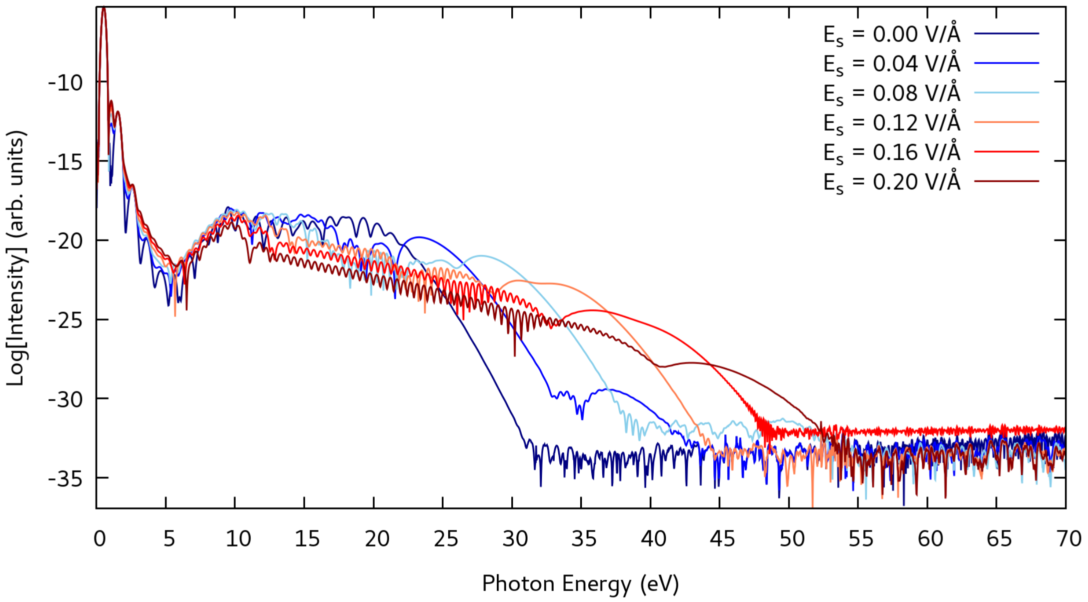

Figure 4.9: The power spectra of HHGs under an additional static electric field, with various colors indicating different static field strength. The blue, light-blue, pink, red, and brown lines are results with the static electric field E_s being 0.04, 0.08, 0.12, 0.16, and 0.20 V/Å, respectively. Also, the power spectrum of HHGs without an additional static field is represented as the black line.

Empowered by the semi-classical model, we could describe the two features observed in the HHG power spectrum, namely higher cutoff energy and lowered overall intensity beyond band gap energy, by some simple physical pictures. The higher maximum emission energy induced by the static field could be understood as the following: In the case with no static field, some high-energy electron-hole pairs are unable to recombine after the oscillatory laser changes its direction because the laser force in this altered direction is not strong enough to bring the pairs back together for recombination. However, in the case when an additional static field presents, if this static force is in the same direction

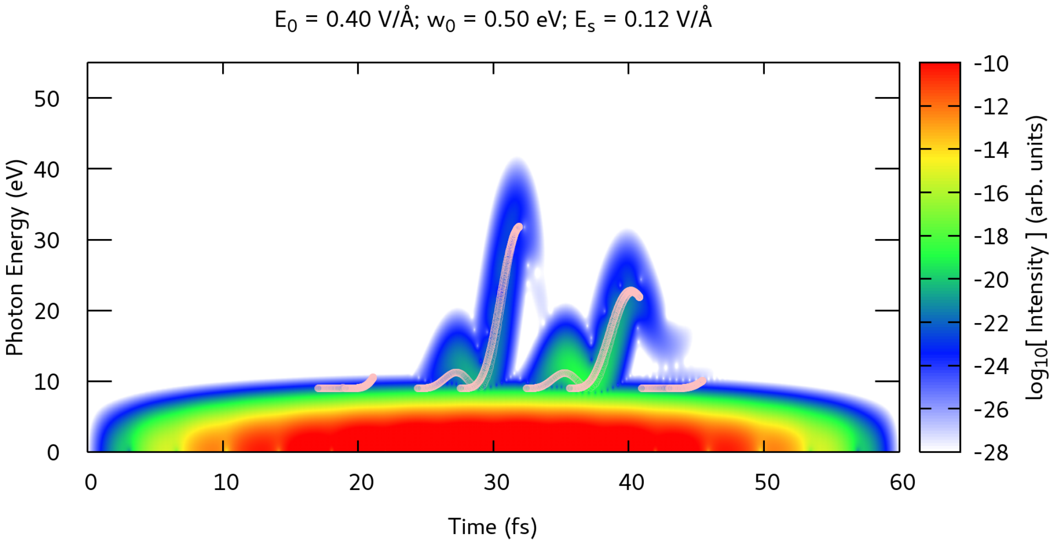

Figure 4.10: The time-frequency analysis of HHG (color map) and its semi-classical prediction(pink circles) with the electric field amplitude of the oscillatory laser $E_0 = 0.4$ V/Å and the electric field amplitude of the static field $E_s = 0.12$ V/Å.

as the altered oscillatory laser force most of the time, the total force would push the paired electron and hole toward each other. Therefore, these high-energy electron-hole pairs now have higher chances to recombine, emit high-energy photons, and extend the cutoff energy in the HHG power spectrum.

As for the lowered overall HHG intensity beyond band gap energy, it could be simply understood by the fact that in general the additional static field is trying to separate electrons and holes away from each other and thereby impedes recombination and lowers the emission intensity. In the extreme case when the strength ratio $E_s/E_0 = 1$, there cannot be any recombination at all within the semi-classical model because the total electric force exerting on the electron-hole pair is always pointing in one direction, meaning the electron and the hole are always being accelerated away from each other. That is to say, in order to have possible recombination, the oscillatory electric field should overcome the static electric field in some time windows. And it is the electron-hole pairs excited in these time windows that could possibly recombine in the future after the total electric force changes its direction. It is clear that these time windows will gradually diminish as E_s/E_0 increases from 0 and eventually disappear at $E_s/E_0 = 1$. Consequently, the possibility for recombination also decreases with the increasing static field, yielding a lower HHG intensity.

From the two discussions mentioned above, one can see that two mechanisms induced by the static field are competing with each other: Electron-hole recombination of some trajectories is made possible but overall the probability for electron-hole recombination is lowered. As a result, it is expected that the cutoff energy should not increase indefinitely with increasing static field but reach a maximum and decrease due to the overall lowered recombination probability. This is indeed observed in quantum simulations. In fig. 4.11 the color map describes the HHG power spectrum as a function of the static electric field amplitude and the purple lines describe the cutoff energy from the semi-classical model (the upper and lower cutoff will be discussed shortly). From this figure, we can see that with the increasing static electric field amplitude the cutoff energy increases from about 25 eV, reaching its maximum at around 40 eV near $E_s = 0.15$, and drops thereafter. Notice that the semi-classical model also captures such behavior and reasonably reproduces the quantum result quantitatively.

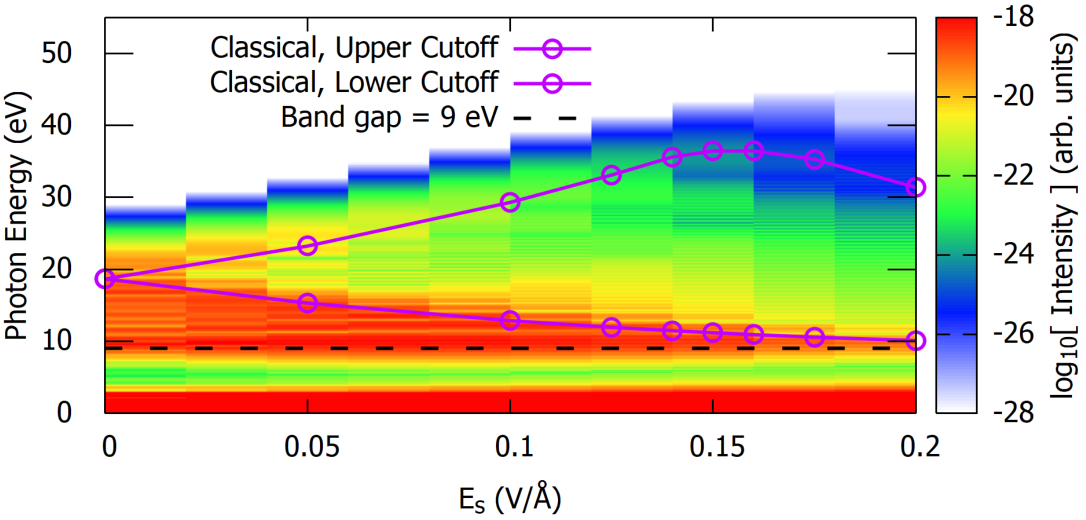

Figure 4.11: The power spectrum of the HHG as a function of the electric field amplitude of the static field E_s is shown as the color map. The observed upper and lower cutoffs from the semi-classical model are both shown as purple lines. Moreover, the band gap energy of the system $E_g = 9$ eV is denoted by the black-dotted line.

4.2.3 Splitting of the Cutoff by the Broken Symmetry

Under a static field, the single plateau in a solid-phase HHG power spectrum is split into two plateaus, creating a spectrum with two cutoffs as shown in Fig. 4.11. This splitting of the cutoff energy from one to two could be understood by the broken symmetry induced by the static field. To understand this consequence, let us first consider a conventional HHG in solids. In the absence of a static field, the intensity of a laser remains exactly the same over a time translation of half optical cycle. This symmetry in time ensures that, if an electron-hole pair is created at time t_{ex}, there will be another pair created at time $t'_{ex} = t_{ex} + T/2$ where T is the period of the oscillating field. This is simply because the system is excited by the field of the same intensity at the two different times. The trajectory $x(t)$ of the electron-hole pair created at time t_{ex} will be the opposite of the trajectory $x'(t)$ of the electron-hole pair created at time t'_{ex} because the opposite sign of the electric field between half cycle is the only difference between the two trajectories. That is, we have a simple relation $x'(t) = -x(t - T/2)$ between the two trajectories. Since the two trajectories are merely a shifted inversion of each other, they would also possess the same return time (time difference in recombination and excitation) and photon energy for their HHG. In another word, these two trajectories are degenerated in the sense of emitted photon energy.

Now with a static field applied to the system, the intensity of the laser, which consists of an oscillating and a static component, is no longer the same between each half cycle. This indicates the two trajectories $x(t)$ and $x'(t)$ mentioned above will no longer simply be shifted inversion of each other and the emitted photon energy coming from the two trajectories will no longer be the same. Each of the trajectories now will have its distinctive emission energy. In a nutshell, the degeneracy of the trajectories is removed by the static field through symmetry breaking. This could be made clear through the relation between the gained energy of electron-hole pairs from the laser and its return time described in Fig. 4.12. In this figure, the case without a static field is represented by the black-circle curve and the cases with a static field of 0.1 and 0.2 V/Å are described by the red- and blue-circle curves, respectively. By comparing the cases with and without a static field, we can easily see the static field split the curve from one (black) to two (red or blue), and the splitting is becoming larger and larger under a stronger static field. This directly shows that the static field removes the degeneracy in the energy of the photon emission.

The broken symmetry by a static field can also describe the different dependence of the cutoff energy on the strength of the static field. The two curves in the case with a static field in Fig. 4.12 corresponds to the different responses to the total electric field between half cycles. For example, let us consider the case with a static field $E_s = 0.1$ V/Å, namely the two red-circle curves in Fig. 4.12. Note that, when compared with the case without a static field (black-circle curve), one of the red curves has higher gained energy and the other has lower gained energy. This could be understood to some extent when the static field is not strong compared to the oscillating field. Assuming that electron-hole pairs are mainly created at the peak of the oscillating part of the laser, the pair will be accelerated more by the laser (consist of an oscillating and a static field) during the second step if the oscillating field is in the same direction of the static field. We address this as the enhanced acceleration. This results in a higher gained energy compared to the case without a static field. On the other hand, if an electron-hole pair is created at the time when the oscillating field is in the opposite direction of the static field, the pair will not experience much acceleration during the second step. This is addressed as the suppressed acceleration. As a result, the gained energy for this pair would be smaller compared to the case without a static field. Note that as the strength

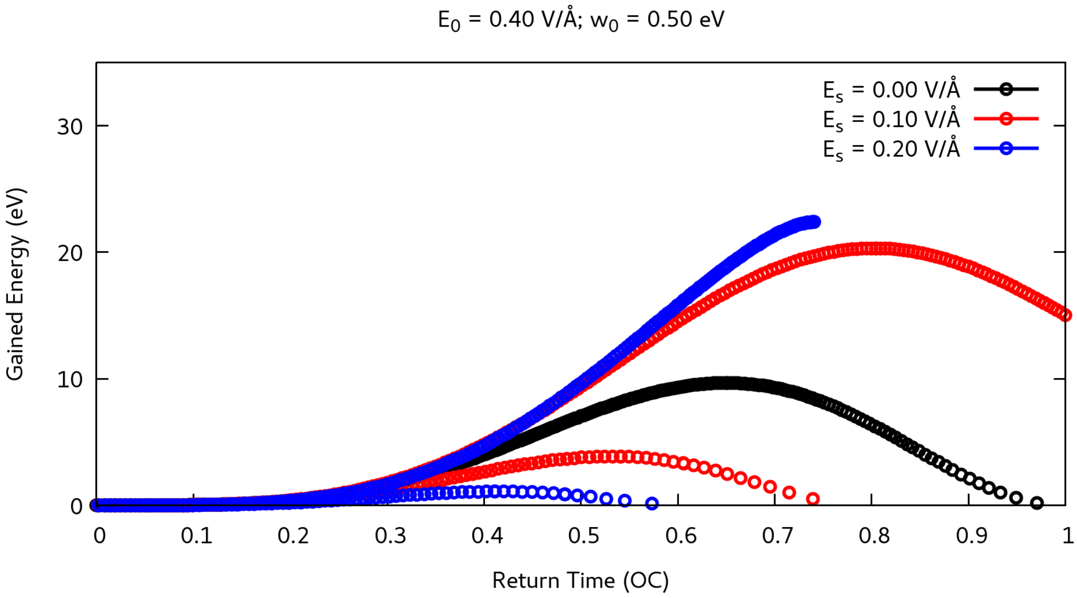

Figure 4.12: The energy gained by electron-hole pairs at recombination as a function of return time is shown. The results with the static electric field amplitude E_s being 0, 0.1, and 0.2 V/Å are described as black-, red-, and blue-circle curves, respectively. One can clearly observe the gained energy for the case without a static field splits from one curve to two curves when E_s is increased.

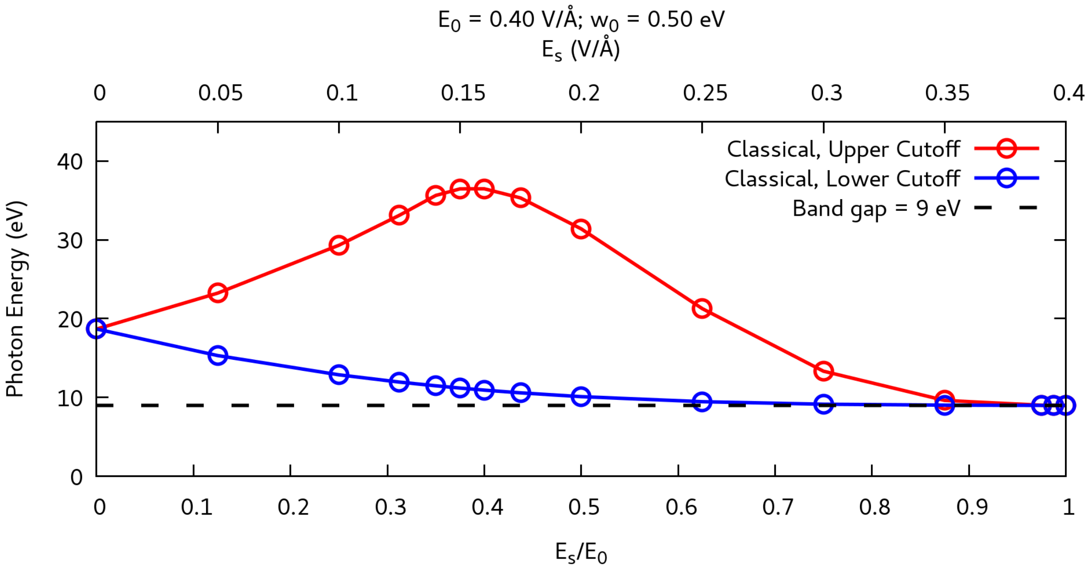

Figure 4.13: The cutoff energy predicted by the generalized three-step model as a function of the electric field strength ratio E_s/E_0 with $E_0 = 0.4$ V/Å. The upper and lower cutoffs are designated by the red and the blue lines. The band gap energy $E_g = 9$ eV is also shown for reference as black-dashed line.

of a static field increases, the degree of enhancement or suppression is also increased. The different response to the laser leads to a positive dependence of the cutoff energy (gained energy increases with a static field) for electron-hole pairs subjected to enhanced acceleration and negative dependence of the cutoff energy (gained energy decreases with a static field) for pairs with suppressed acceleration when the static field is weak. This behavior can be clearly observed from the cutoff energy predicted by the generalized three-step model in Fig. 4.13 with $E_s < 0.3$ V/Å. Our idea here is an analogy to the concept proposed in previous studies for gas-phase HHG under a weak static field [32].

Beyond a weak static field, we would have to apply some modification to the electron-hole pairs subjected to suppressed or enhanced acceleration. For the pairs with suppressed acceleration, their contribution to HHG becomes less important under a stronger static field. Note that pairs would be less likely to be created at the time when the oscillating field is in the opposite direction of the static field because the total laser intensity becomes smaller with the stronger static field. Also, even if such electron-hole pairs are created, the emitted photon energy would become smaller and approach band gap as the suppression of acceleration is larger with the stronger static field.

As for the electron-hole pairs with enhanced acceleration, we should incorporate the fact that the pairs cannot recombine and emit a photon if they are accelerated too much. Note that, with the stronger static field, the amount of time that the oscillating field changes sign and pushes the electrons and holes back together would become smaller, leading smaller chance of recombination. Therefore, for electron-hole pairs subjected to enhanced acceleration, the pairs created at the peak of the oscillating field will contribute less to HHG under the stronger static field. Since the electron-hole pairs with enhanced acceleration that are created when oscillating field peaks are less important, the main contribution to HHG now comes from electron-hole pairs with enhanced acceleration that are created at the time away from the peak oscillating field. The pairs created at this time will not be accelerated too much due to the shorter time of acceleration so they could actually recombine and contribute to HHG. The two mechanisms, namely more acceleration gives larger emission energy and electron-hole pair creation away from peak field to avoid too much acceleration, compete with each other and eventually yield a saturation in cutoff energy with the increasing static field. This saturated cutoff is indeed observed in Fig. 4.13.

We should emphasize that, in general, the energy of the emitted photon from electron-hole pairs depends on the electric field the pairs experience between the time of creation and recombination. The proposed physical picture here aims for a simple semi-classical description for the process but also at the same time captures the behavior of the cutoff dependence on a static field.

Chapter 5

Light Absorption of Core Electrons

In recent years, the development of free-electron laser (FEL) has created new opportunities for X-ray spectroscopy [44, 45]. The generation of high-energy photons in the energy range of the soft X-ray to the hard X-ray in FEL has been realized and demonstrate in various facilities like FLASH, FERMI, SCALA, and LCLS [46, 47, 48, 49]. One of new possibility in X-ray spectroscopy enabled by FEL is harmonic generation using a soft X-ray as a seed. In experiments, second harmonic generation from soft X-ray are observed and its intensity dependence on different laser parameters are measured [50, 51, 52]. The trend in developing harmonic generation with a soft X-ray motivates us to consider the prospect of HHG in solids from an input FEL in the soft X-ray regime. Specifically, we are interested in developing the theoretical framework modeling the HHG using a soft X-ray in solid systems.

There are several numerical and theoretical challenges in establishing a practical model for the dynamical process of HHG using a soft X-ray in solids, and one of the major challenges is the appropriate description for light absorption of core electrons. Due to the large photon energy of the X-ray FEL, it is the core electrons deep inside atoms rather than the valence electrons near Fermi level that are excited by the laser. To numerically describe these core electrons which concentrates in a tiny space near a nucleus, a high density of grid points is needed near the nucleus with the real-space grid representation. This leads to very high computational cost for simulations of such processes. Therefore, how efficient a numerical approach is also matters a lot in the choice of theoretical framework. In addition to the numerical challenge, there are also many theoretical difficulties to overcome for appropriately describing the solid-phase HHG using a soft X-ray. For instance, in TDDFT, which is an efficient *ab initio* model with effective electron-electron interaction [39], the reproduction of light-absorption for core-electrons is challenging with conventional approximations of the exchange-correlation functionals. In the conventional mean-field treatment, the occupation of core electrons is treated effectively in an averaged sense. Similarly, the core holes created from excitation of core electrons is also treated in the averaged sense. This means the number of core holes in a cell could be a fractional value, while in real world it is always an integer. Here it should be emphasized that we are talking about the number of core holes in one cell, not the number of core holes per cell calculated from the ratio of the number of core holes to the number of cells in a crystal. In the real world, a fractional value of, say 0.5, for the number of core holes per cell simply means (assuming one core electron per cell) half of cells have one core hole and the rest of the cells has no core hole. Therefore, in one cell the number of core holes is always an integer. However, in the mean-field approximation, a fractional value of 0.5 for the number of core holes per cell would mean every cell has one-half of core holes. This might be of an issue for accurate description for light absorption of core-electron because it has been well-known that the photon absorption in solids depends strongly on the number of the core holes under a high-intensity soft X-ray. The absorption of soft X-ray photons would gradually decreases with a stronger laser so the absorption eventually saturates. This phenomenon is typically know as saturable absorption or light-induced transparency.

In order to theoretically describe the solid HHG using a soft X-ray, we need to examine if the absorption of core electrons could be accurately captured in an efficient model. If a model successfully reproduces the saturable absorption of core electrons under soft X-ray, it would thereby serves as a possible candidate for simulating the solid-phase HHG using a soft X-ray. For our study in this chapter, we simulate a solid system of bulk aluminum by employing TDDFT with the adiabatic local density approximation and obtain the absorption coefficient at different intensity of a soft X-ray laser. Then a pulse propagation in an aluminum film in the classical limit is carried out by using the intensity-dependent absorption coefficient to see whether the model could reproduce the saturable absorption. It is found that TDDFT does successfully capture the phenomenon. Also, with a deeper examination on the process, it is also confirmed that the model reproduces the saturable absorption in accordance with the already-established mechanism. Our results here verify that TDDFT could be suitable for the theoretical framework describing solid-phase HHG using a soft-ray, at least for the very first step, namely excitation, of the process.

This chapter is composed of the following: In the first section we introduce the saturable absorption and its mechanism behind. Then we discuss the setup of the system and theoretical framework in the second section. Specifically, the microscopic model TDDFT for computing absorption coefficients and the macroscopic model for propagation of a soft X-ray pulse are discussed. In the last section, the result of saturable absorption and correction with some real-world effects are presented.

5.1 Saturable Absorption in Aluminum and its Mechanism

Saturable absorption is the behavior of decreased light absorption under a laser of increased intensity. This phenomenon could make a material which is originally opaque to a laser gradually become transparent when the laser intensity becomes stronger, and therefore is sometimes addressed as light-induced transparency. Saturable absorption of a soft X-ray in aluminum has been well-studied and the mechanisms behind the saturation are also described by a simple model in the previous study [53].

It is proposed that the core electrons which are responsible for absorbing the incoming high-energy photon could be depleted by the high-intensity soft X-ray since the thermal relaxation of excited electrons is not fast enough to supply electrons back to vacancies in core energy levels. When these core electrons are all excited, there are simply no energy receiver for incoming photons, leading to saturable absorption of the light. At the same time, during the excitation of core electrons, the attractive force between core electrons and their parent ion core is also modified, leading to the shift of the core energy levels and rendering absorption of high-energy photon unavailable. The idea of this modified attractive force is that, when core electrons gradually become excited and move away from the parent ion, the electronic shielding formed by the negatively-charged core electrons on the positively-charged parent ion will also become weaker. This means the attractive force from the parent ion acting on the remaining bounded electrons will become larger with the excitation of core electrons. That is, the remaining electrons are now more tightly bounded. Generally speaking, core electrons will experience a stronger increase in attractive force compared to electrons in conduction bands when the shielding is attenuated, because core electrons are more closer to the ion core and thereby more sensitive to the weaken shielding. The energy shift of core levels (2p orbitals) and the conduction band are schematically shown in Fig. 5.1 (a) and (b). As a result, once many core electrons are excited, it would take more energy to move the remaining core electrons to the conduction band at Fermi surface. With the energy shift, the energy of incoming photons of the soft X-ray now is no longer sufficient to excite the more-bounded core electrons, leading to saturable absorption. This idea is also illustrated schematically in Fig. 5.1 (c) and (d).

In our examination of core absorption, if saturable absorption is indeed reproduced, we should also verify whether the phenomenon is induced by the mechanism described above to ensure the reproduction is not merely a coincidence.

5.2 Theoretical Framework

Here we will consider a setup in the experiment [8], namely directing a soft X-ray towards a thin film of aluminum and measuring its transmission. Our theoretical framework would involve a microscopic simulation based on TDDFT [39] and a macroscopic calculation of electronic wave propagation in aluminum based on electrodynamics in the classical limit. We perform microscopic simulations to measure the absorption coefficient under a soft X-ray with different laser intensities. And Then we use this intensity-dependent absorption coefficient to calculate attenuation in intensity macroscopically for a soft X-ray pulse propagating in the Al film. Therefore, the soft X-ray pulse penetrating the Al film could be obtained and its transmission through the film can then be calculated.

In the procedures mentioned above, we have made several assumptions. First, it is assumed that, when the laser pulse penetrates through the Al film, the change of laser intensity due to absorption over hundreds of lattice sites is tiny. This is equivalent to

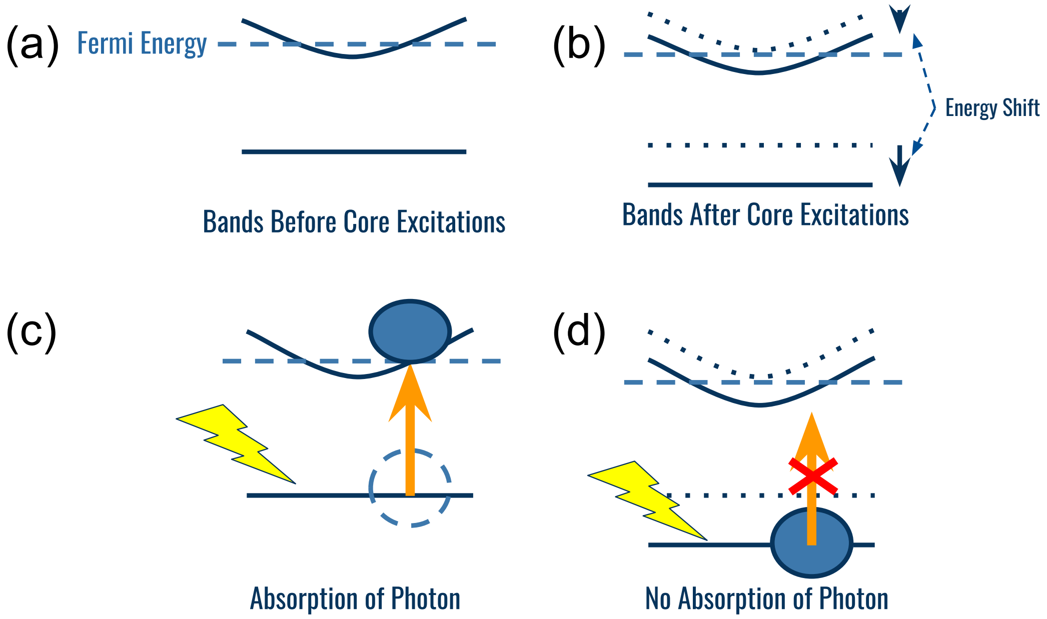
(a)
Fermi Energy
Bands Before Core Excitations
(b)
Energy Shift
Bands After Core Excitations
(c)
Absorption of Photon
(d)
No Absorption of Photon

Figure 5.1: A schematic view for the mechanism of saturable absorption under a soft X-ray in aluminum. The conduction band is represented by a parabola and the core energy level for 2p orbitals is described by a flat line. Also, an incoming X-ray photon is depicted by the yellow lightning. The energy bands (a) before and (b) after excitation of core electrons are shown in the upper section. In (a) the positive core ion is electronically shielded by core electrons. In (b), the electronic shielding of the core ion is attenuated since some core electrons are excited, and the energy bands are now bounded more tightly, which is indicated by the energy shift of the bands. The interaction between photon and a core electron (c) before and (d) after the bands are shifted is also described in the lower section. (c) Before the energy shift, core electrons can absorb the soft X-ray photon and be excited to the Fermi surface. (d) After the energy shift, the photon energy of the soft X-ray is not large enough to make the excitation possible.

cutting the Al film into many even-thinner slices with a thickness of several hundreds of the lattice constant, and assume the soft X-ray is hardly absorbed within each slice. Note that the cut is made in the way such that the soft X-ray has normal incidence on each slice. The assumption allows us to perform the microscopic simulations under an electric field with fixed maximum amplitude. This approximation would be reasonable as long as the thickness of the slice is made small to guarantee little absorption within the slice. Second, within each slice we apply dipole approximation for the laser field to ease the computational cost. This is valid since the wavelength of the soft X-ray used in our study is still much larger than the lattice constant of aluminum. Finally, we treat each slice of the film as a bulk aluminum in the microscopic simulation. The rationale is that, although the slice is quite thin, the thickness is still in the scale of several hundred cells so the light absorption is not sensitive to the two surfaces.

5.2.1 Time-dependent Density Functional Theory

For the microscopic simulation, we employ *ab initio* simulations based on TDDFT, which involves mapping of an interacting many-electron system to many non-interacting single-electron systems [39]. If conventional approximations are applied, the model could be seen as a mean-field approach in the sense that the complicate electron-electron interaction is treated as an average potential depending solely on the density of electrons. In this model, the dynamics of the wavefunction of an electron $\psi(\boldsymbol{r};t)$ is governed by the time-dependent Kohn-Sham equation:

$$\frac{\partial}{\partial t}\phi(\boldsymbol{r};t) = H_0 + H_H + H_{xc} \tag{5.1}$$

where H_0, H_H, and H_{xc} are single-electron Hamiltonian, Hatree potential, and exchange-correlation potential, respectively. The single-electron Hamiltonian contains kinetic energy in the velocity gauge with vector potential $\boldsymbol{A}(t)$ and potential energy from the lattice ions $U(\boldsymbol{r})$:

$$H_0 = \frac{(\boldsymbol{P} - q\boldsymbol{A})^2}{2M} + U \tag{5.2}$$

with P the momentum operator and M and q the electron mass and charge (sign included). The Hartree potential describes the energy from classical Coulomb interaction between the current electron and other electrons:

$$H_H = \int_{\boldsymbol{r}'} \frac{q^2 n(\boldsymbol{r}')}{|\boldsymbol{r} - \boldsymbol{r}'|} d\boldsymbol{r}' \tag{5.3}$$

with $n(\boldsymbol{r})$ then density of all electrons. For the exchange-correlation potential $H_{xc} = H_x + H_c$, we take the local-density approximation so the exchange part of the potential H_x is taken from the homogeneous electron gas [54]:

$$H_x = -\frac{3}{4}\Big[\frac{3n(\boldsymbol{r})}{\pi}\Big]^{\frac{1}{3}} \tag{5.4}$$

and the correlation part H_c is given in term of a parametrization by Perdew and Wang [55].

The vector potential $\boldsymbol{A}(t)$ of the laser pulse used for calculating absorption coefficient admits the form:

$$\boldsymbol{A}(t) = \frac{F_0}{\omega_0}\cos^2(\frac{\pi}{\tau}(t-\frac{\tau}{2}))\cos(\omega_0 t)\hat{x} \tag{5.5}$$

where F_0 is the maximum electric field amplitude, $\tau = 30$ fs is the total pulse length, $\hbar\omega_0 = 85.5$ eV is the photon energy of the soft X-ray, and $\hat{x}$ is a unit vector in the positive-x direction. Outside the time domain $0 \leq t \leq \tau$ the vector potential is set to zero. The energy flux, or fluence Φ, for the pulse can be calculated by:

$$\Phi = \epsilon_0 c \int_0^\tau \left[F_0\cos^2(\frac{\pi}{\tau}(t-\frac{\tau}{2}))\sin(\omega_0 t)\right]^2 dt \tag{5.6}$$

with ϵ_0 the electric permittivity of vacuum and c the light speed. In this calculation of fluence we use long-pulse approximation ($\tau \gg \frac{2\pi}{\omega_0}$) for the electric field. Note that the photon energy considered here is different from the experiment [8], because the absorption spectrum of bulk aluminum from our theoretical simulation has a different absorption edge so we shift our photon energy such that the same distance from the edge is achieved. See Fig. 5.3.

The numerical simulation of the TDDFT is carried out by the program Octopus [56]. In the simulation, electrons of an Al atom in the 1s and 2s orbitals are treated as frozen electrons not participating the photon absorption. The lattice constant for the cubic cell of Al is set to 4.0485 Å. The spacing for grids in real space is set to 0.15 Å, and the number of grid points in the crystal-momentum space is set to 27 in each dimension. For time propagation, the time step is set to 0.02 Å.

5.2.2 Calculation of Transmission

The calculation of transmission of soft X-ray through the Al film is carried out by propagating a classical wave in the aluminum film with a fluence-dependent absorption coefficient from the microscopic simulations. We first perform TDDFT simulations under a soft X-ray pulse and measure the excess energy density ρ_{ex} of bulk aluminum, which is the increment in total energy of electrons per unit volume after the pulse. This quantity could also be interpreted as the absorbed energy per unit area per penetration depth of the advancing pulse. Therefore, by definition, we can calculate the absorption coefficient a by:

$$a = -\frac{1}{\phi(0)}\frac{d\phi(z)}{dz} = \frac{1}{\phi(0)}\rho_{ex} \tag{5.7}$$

where $\phi(z)$ is the energy flux, or fluence, at a penetration depth z of the pulse. Here we assume the pulse is propagating in the positive-z direction and the Al film starts at $z = 0$ and ends at $z = L$ with $L = 53$ nm the thickness of the film.

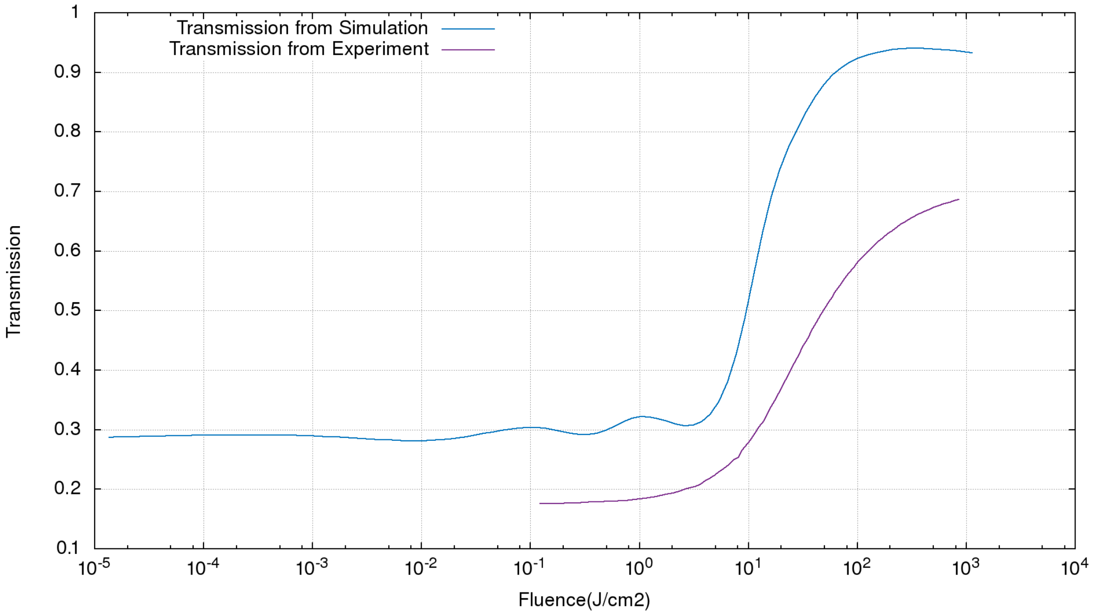

Figure 5.2: Comparison of the transmission as a function of laser fluence between our theoretical calculation (blue curve) and the experimental data (purple curve) taken from the study [8]. Note that, since only the laser intensity is altered in the pulse and the laser fluence is proportional to the intensity, the axis of fluence can be seen as the axis of intensity.

By sampling the absorption coefficients at different intensities (or fluence) of the soft X-ray pulse from microscopic simulations, we can form the absorption coefficients as a function of fluence $a(\phi)$ by fitting the sampling points with cubic splines. Then the fluence at different penetration depth can be solved by numerical integration of Eq. 5.7. Numerically, we calculate the fluence at the next step $\phi(z + \Delta z)$ from the fluence at current step $\phi(z)$ by:

$$\phi(z + \Delta z) = \phi(z) - \phi(0)a(\phi(z))\Delta z. \tag{5.8}$$

Finally, the transmission T is calculated as the ratio of the fluence before and after the Al film, namely $T = \frac{\phi(L)}{\phi(0)}$.

5.3 Absorption of Core Electrons

5.3.1 Saturable Absorption

The calculated transmission of a soft X-ray at different laser fluence (or intensity) is given in Fig. 5.2 as the blue curve, together with the experimental data (purple curve) for comparison. From this figure, it is clear that our approach not only reproduces the

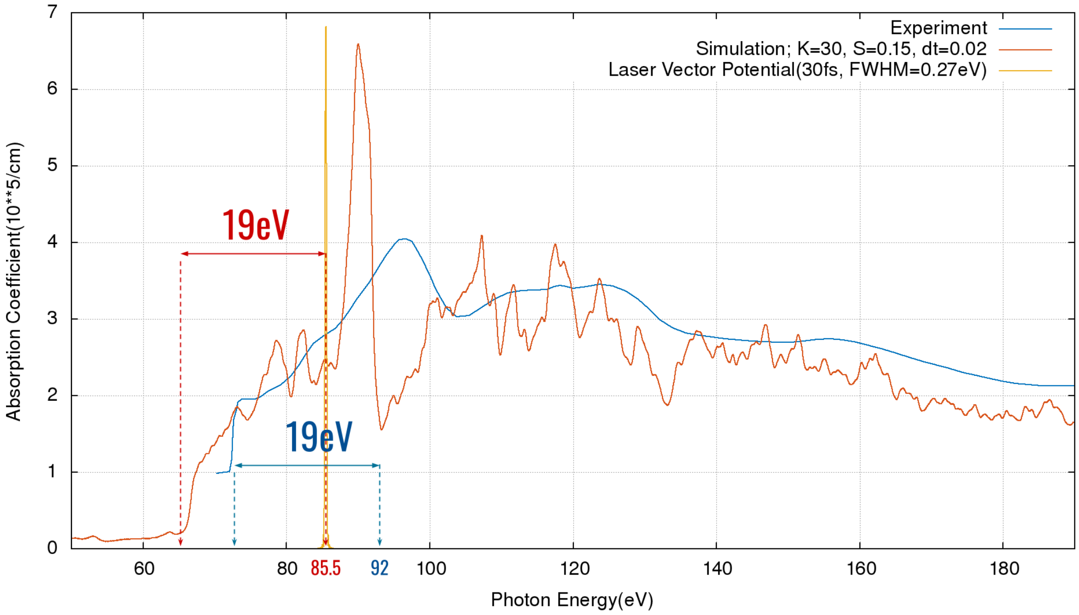

Figure 5.3: The absorption spectrum of aluminum near the $L_{II,III}$ absorption edge from theoretical calculation (red curve) and experimental data (blue curve) taken from the previous study [58]. The vector potential of the soft X-ray used in this chapter is also shown as a sharp yellow peak to illustrate its position in the absorption spectrum. The FWHM of the laser is around 0.27 eV. Additionally, we also mark the energy difference of 19 eV between the absorption edge and the laser in the case of our simulation and the experiment. We select a soft X-ray with photon energy of 85.5 eV instead of 92 eV used in the experiment because it has the same distance from the edge in the absorption spectrum.

behavior qualitatively but also gives comparable values to the actual experimental data. Most importantly, the transmission of the soft X-ray pulse exhibits clear increment when the laser intensity is increased. This suggests that the Al film becomes more transparent when subjected to a stronger soft X-ray and therefore the saturable absorption is indeed reproduced.

To examine the fundamental reason behind the increasing transmission under strong X-ray, we also calculate the absorption spectrum of bulk aluminum. The absorption spectrum can be obtained by sending a kicks (a Dirac delta function in time for the electric field) to the bulk aluminum system and measuring the current density responding to the kick [57]. In Fig. 5.3, the absorption spectrum of bulk aluminum near $L_{II,III}$ absorption edge is shown. The experimental data is also plotted in the same figure for ease of comparison. Despite some differences in the position of peaks, the absorption spectrum from the TDDFT simulation with a kick reasonably capture the overall structure of the experimental spectrum. Note that the photon energy of the soft X-ray is well above the absorption edge for this absorption spectrum from aluminum in the ground state. With

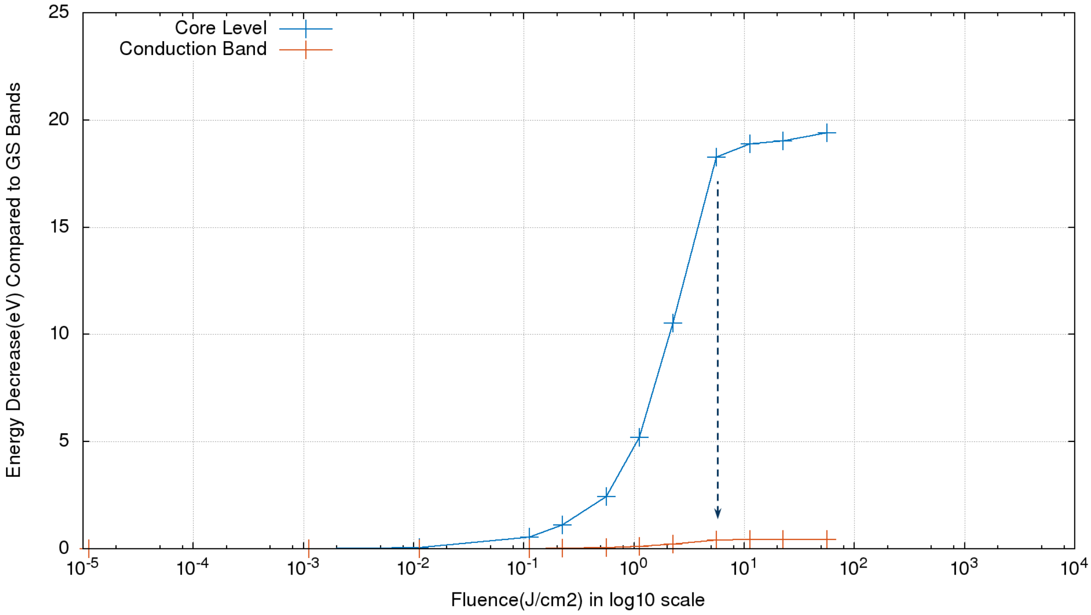

Figure 5.4: The decrease in energy as a function of fluence for the core level (blue curve) and a conduction band (red curve) compared to their original energy in the ground state. The arrow indicates the fluence around 5 J/cm^2 where the core level has huge energy shift. Note that at this large energy shift in the core level the energy shift in the conduction band is negligible. This makes the photon energy of the soft X-ray off-resonance and thereby saturable absorption occurs.

this kick technique for calculating absorption spectra, we measure the spectrum of the bulk aluminum after the application of the soft X-ray pulse at different pulse intensities. It is found that the general structure of the absorption spectrum remain roughly the same at different laser intensities, but the structure is shifted to region of higher energy. The shift could be made more clear by calculating the energy bands after the application of the soft X-ray pulse. In Fig. 5.4, the change in energy for the core level and the conduction band compared to their ground-state counterparts are described by the blue curve and red curve, respectively. From the figure, it is clear that the core-level energy is much more sensitive to the change of laser fluence compared to the conduction band energy. In the high fluence region (fluence larger than 5 J/cm^2), the core level has shifted down in energy by around 20 eV while the conduction band only shifts down by less than 1 eV. This indicates that the energy difference between the core level and the Fermi surface would increase by around 19 eV, or equivalently the $L_{II,III}$ absorption edge shift up in energy by around 19 eV. With this shift, the photon energy of the soft X-ray is no longer above the absorption edge, and therefore the photon can no longer be absorbed. This is the microscopic description for the saturation in absorption and the increase in transmission under stronger soft X-ray.

As a quick summary, the behavior of saturable absorption of a soft X-ray in aluminum is indeed reproduced by the our theoretical framework that combines microscopic TDDFT simulations and macroscopic calculation of classical wave propagation. The success comes from the proper description of the attenuated absorption coefficient under a stronger soft X-ray. Also, by calculation of the energy structure after the pulse, the core energy levels exhibit a large negative shift, leading to an overall shift of the absorption spectrum to a higher energy region and rendering photon absorption unavailable. The mechanism responsible for saturable absorption thus aligns with the description proposed by previous study [53]. This could serve as an evidence for that TDDFT can accurately describe the dynamical process of photon absorption of core electrons in aluminum under a soft X-ray.

5.3.2 Corrections to Transmission from Theoretical Calculation

In this final section of the chapter, we would like to briefly consider some real-world effects in experiments to improve the quality of the transmission from our theoretical calculations. For example, in experiment the laser intensity at the focal spot will not be uniform over the tiny shined area. We could assume a simple Gaussian distribution of the laser intensity in the focal spot to estimate this effect. In Fig. 5.5, we have calculated the transmission averaged over the focal spot (red curve), together with the one without focal-spot average (blue curve) and the one from the experiment (purple curve) for comparison. We can see that the transmission as a function of fluence indeed becomes more closer to the experimental data. In addition to the effect of focal-spot average, we could also consider the oxidation of the aluminum film in real experiments. Typically speaking, the surface of the aluminum film will inevitably suffers from oxidation due to the very dilute oxygen remaining in a gas chamber. The oxidized compound, namely Al_2O_3, has a different absorption coefficient and could lead to some variation of the overall transmission. To assess the effect of the surface oxidation, we add a 10 nm aluminum oxide layer on the front and back side of the 53 nm Al film (so the thickness of the film is totally 73 nm) and the absorption coefficient of the aluminum oxide is set to 3.95×10^5/cm for the soft X-ray. This absorption coefficient is assumed to remain constant under various laser fluence. We show the transmission of such a surface-oxidized Al film (red curve) in Fig. 5.6, together with the one without surface oxidation (blue curve) and the one from the experiment (purple curve). It is clear that the overall transmission is decreased, because the surface oxide layer keeps absorbing the soft X-ray irrespective of the laser intensity. From this result, one could say such surface oxidation does make a big difference so special care should be taken for observing saturable absorption in aluminum.

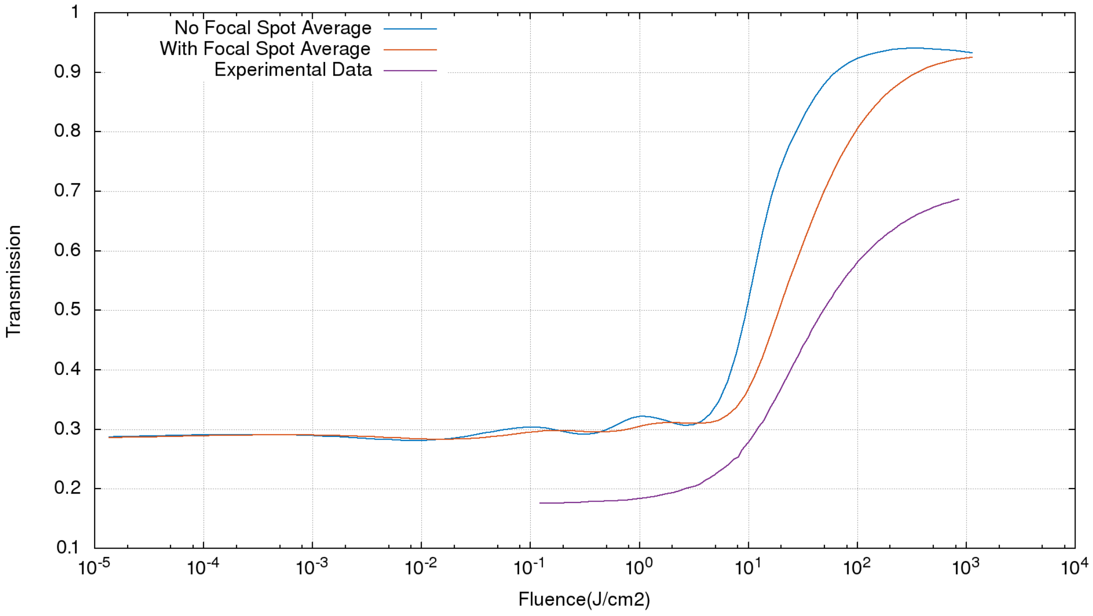

Figure 5.5: Transmission as a function of laser fluence from theoretical calculation for the case with focal-spot average (red curve) and the case without focal-spot average (blue curve). Transmission from the experimental data is also shown as the purple curve for comparison.

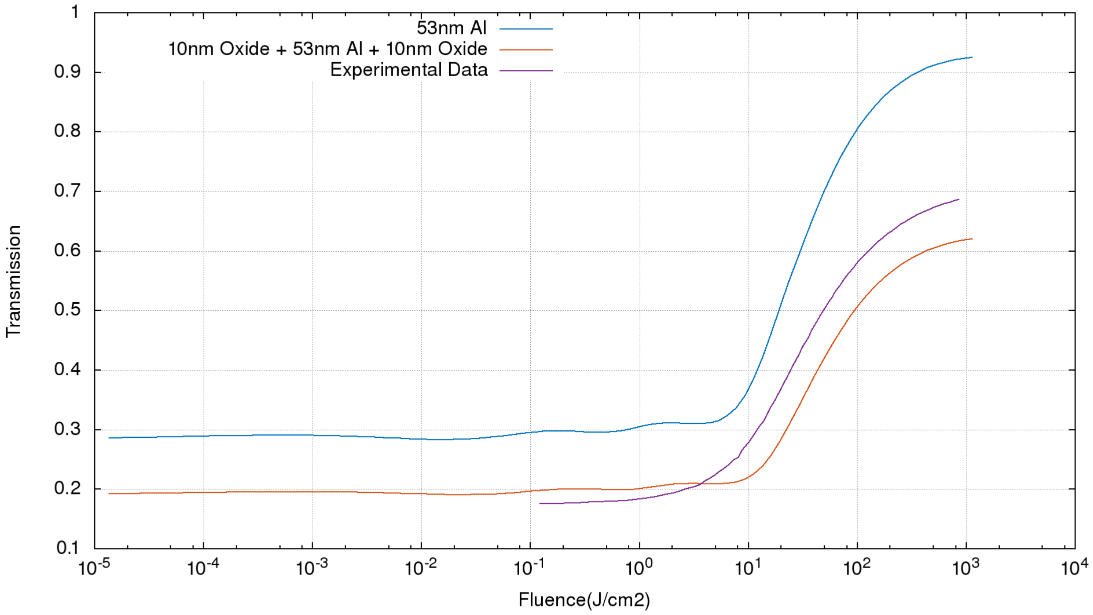

Figure 5.6: Transmission as a function of laser fluence from theoretical calculation for the case with surface oxidation (red curve) and the case without surface oxidation (blue curve). Transmission from the experimental data is also shown as the purple curve for comparison.

Chapter 6

Conclusion and Outlook

The development of HHG in gaseous systems over the years has demonstrated the powerful applications and extensive potential of harmonic generation as a tool for physical investigation. The extension of HHG to the realm of solid systems and the corresponding revamped HHG applications are thus highly anticipated and widely studied in the community of strong-field physics. This motivates our studies for HHG in solids in the aspect of its dynamics. Specifically, we aim to investigate the corresponding change of dynamics as a consequence of scattering effects and a static field. Furthermore, the realization of X-ray FEL in recent years creates even more potential for HHG in solids because harmonic generation based on a soft X-ray has now become achievable. Considering the complexity and novelty of this new field, any theoretical approach describing the dynamical processes of HHG from a soft X-ray should be proposed with intensive prudence and robust foundation. Therefore, we have also investigated the applicability of the *ab initio* approach based on TDDFT in light absorption of core electrons, which is a key process for HHG using a soft X-ray. In this final chapter, our results for each topic mentioned above are summarized and their corresponding outlook is discussed.

In the study of scattering effect on solid-phase HHG, we extended the generalized three-step model through the incorporation of Umklapp scattering, which was carried out by branching classical trajectories in the model whenever a scattering event occurred. The results of the extended semi-classical model were compared with those from quantum simulations of a one-dimensional quantum system. It was shown that the features of multiple plateaus in the HHG spectrum from quantum simulations were reasonably captured by the extended semi-classical model. The contribution of scattered trajectories was also identified clearly through time-frequency analysis for each plateau. Therefore, we have concluded the multi-plateau in HHG power spectra from a solid system is a direct consequence of Umklapp scattering, which opens up more emission channels for created electron-hole pairs. Additionally, in order to deal with general scattering effects in solids, we have also proposed a simple modification to the generalized three-step model by the concept of the mean-free path. It was shown that the wavelength independence of cutoff energy observed in experiments is reproduced, and thereby we have conclude that the mechanism for such wavelength independence is the general scattering in solid systems. Despite of the strong evidence proposed, special attention should be paid when comparing the results of our theoretical studies on scattering effects with those from real-world experiments. One clear discrepancy here is the missing multiple plateaus in experiments using common semi-conductors as targets. In theoretical simulations, if infinite numerical accuracy is granted, one could in principle have infinite many plateaus since there is always non-zero probability for electrons excited to infinitely higher bands. This is of course meaningless in reality as the probability of the excitation is so low so the corresponding signal will be overwhelmed by noise or is simply beyond the accuracy of experimental measurement. In addition, as mentioned in Chapter 4, higher dimensionality of a system may also lead to lower probability of recombination for electron-hole pairs. This could diminish the signal of multiple plateaus already at the theoretical level. How important these factors are in real-world systems remains to be answered in the future.

As for the investigation on the effect of a static field on solid-phase HHG, we have found that one single plateau in a HHG power spectrum splits into two plateaus with their corresponding cutoff depends differently with respect to the static field. The lower cutoff decreases gradually to the band gap of the system with increasing strength of the static field. On the other hand, the higher cutoff increases with the increasing static field, saturates at a maximum, and then decreases gradually to the band gap. The two different behaviors are described by the broken dynamical symmetry of the system due to the additional static field. We should point out here that our theoretical investigation assumes the target remain intact under the application of the laser and a static field. However, when an oscillating field and the static field align in the same direction, the strength of the total electric field could be very large and damages the target material. Therefore, in real-world experiments, one may not be able to extend the HHG plateau, which is important for the synthesis of ultra-short pulses, by a large margin through by tuning the static field to attain the maximum energy for the higher cutoff. Whether this is a real issue would be another interesting question in solid-phase HHG waiting to be answered.

On the topic of verifying the applicability of the theoretical approach for HHG from a soft X-ray, we have employed TDDFT with the adiabatic local density approximation to describe the light absorption for core electrons in an Al film under a soft X-ray. Our results have revealed that absorption coefficients calculated from the model do lead to the well-known saturable absorption. Also, it is confirmed that the model accurately reproduced the the correct physical mechanism that induced the saturable absorption. As a result, our study here could be another supporting evidence for *ab initio* simulations using TDDFT to describe HHG in solids under a soft X-ray. In spite of the excellent reproduction of the phenomenon, we should still be very cautious about connecting our theoretical results with those from real-world experiments. There are some mechanisms which might affect the light absorption of core electrons but they are neglected in our model. For example, Auger decay might also take a part in the process of light absorption and increase the rate of de-excitation. This leads to the higher core-electron population under a soft X-ray and thereby higher overall light absorption. It would be important to investigate these kind of mechanisms which could not be completely ruled out from the question to further ensure the absorption process is reproduced by TDDFT in a reliable way.

The major contribution of our theoretical works discussed in the thesis to the community of solid-phase HHG lies in the investigation of scattering effects on the HHG power spectrum. The incorporation of Umklapp scattering into the generalized three-step model provides a systematic and procedural approach for handling the scattering effect in the semi-classical description of the HHG. The code for this extended semi-classical model is also publicly available [59]. Additionally, to the author's knowledge, it is the first time that the wavelength independence of cutoff energy of the HHG could be described by such a simple model with general scattering effects. As for the other projects, our theoretical observation on the behavior of split cutoffs would suggest a new possibility of synthesizing ultra-short pulse by utilizing the larger plateau region. Moreover, the success in reproduction of saturable absorption of core electrons suggests *ab initio* simulations based on TDDFT with the conventional mean-field approximation could serve as a good candidate for describing HHG using a soft X-ray in bulk aluminum.

Looking forward, there are a lot of interesting follow-up research for the topics presented in this thesis. For the influence of scattering for HHG in solids, it would be tempting to study the effect microscopically through *ab initio* simulations of three-dimensional systems so one could tell the importance of the scattering effects in scenarios more closer to real experiments. It might even allow people to answer why the higher plateaus shown in theoretical simulations are missing in the real world and establishes a more accurate understanding of the scattering effects in solid-phase HHG. On the topic of adding a static field, it would be of high interest to derive an analytical estimation or even an explicit formula for the higher and lower cutoff in HHG spectra as a function of a static field, because many applications of HHG depend on the cutoff energy. As mentioned earlier, physicists have been synthesizing ultra-short pulse from HHG in the plateau region. One might be able to create an even-shorter ultra-short pulse using the larger plateau region induced by a static field. For this application, it would be crucial to know the actual dependence of the higher and lower cutoff energy and the maximum energy of the higher cutoff achievable in a system. Finally, for HHG using a soft X-ray, it would be interesting to study the HHG directly through TDDFT and see if the generalized three-step model could be applied to this special scenario. Naturally, modification to the semi-classical model is expected since excitation rate is no longer the same in each optical cycle due to shifting core levels. Establishing a new semi-classical model analogous to the three-step model could advance the adaptation of applications in gas-phase HHG to HHG using a soft X-ray. Considering that the energy and time scale of an X-ray is so different from the infrared laser commonly used in HHG, exciting applications at a whole new level, like sub-attosecond ultra-short pulse, may come even closer to reality.

Our works in this thesis are an attempt to expand the current knowledge of light-matter interaction, and broaden our view in the microcosm populated with electrons and atoms. The physical community of strong-field physics is making strides in this exciting adventure, and hopefully our works presented here push the foot for another step on the road. At this rate, I believe the development of HHG would continue to enable the creation of even stronger and sharper illuminating pulses that enlighten the darkness beyond the front line of human knowledge.

Appendix A

Proof of the Equation

In this appendix, we will prove the equation utilized in the derivation of the simple two-band parabolic model discussed in Chapter 2. This equation is (for $m \neq n$):

$$\int_{\Omega_C} u^*_{m\boldsymbol{K}(t)}(\boldsymbol{r}) \frac{\partial}{\partial \boldsymbol{K}(t)} u_{n\boldsymbol{K}(t)}(\boldsymbol{r}) d\boldsymbol{r} = \frac{-\hbar}{E_{m\boldsymbol{K}(t)} - E_{n\boldsymbol{K}(t)}} \int_{\Omega_C} u^*_{m\boldsymbol{K}(t)}(\boldsymbol{r}) \frac{-i\hbar\nabla}{M} u_{n\boldsymbol{K}(t)}(\boldsymbol{r}) d\boldsymbol{r} \tag{A.1}$$

which is actually a special case of the general relation:

$$\begin{aligned}\frac{\partial E_{n\boldsymbol{K}(t)}}{\partial \boldsymbol{K}(t)} \delta_{mn} = & \frac{\hbar}{\Omega_C} \int_{\Omega_C} u^*_{m\boldsymbol{K}(t)}(\boldsymbol{r}) \frac{-i\hbar\nabla}{M} u_{n\boldsymbol{K}(t)}(\boldsymbol{r}) d\boldsymbol{r} + \delta_{mn} \frac{\boldsymbol{K}(t)\hbar^2}{M} \\ & + [E_{m\boldsymbol{K}(t)} - E_{n\boldsymbol{K}(t)}] \frac{1}{\Omega_C} \int_{\Omega_C} u^*_{m\boldsymbol{K}(t)}(\boldsymbol{r}) \frac{\partial}{\partial \boldsymbol{K}(t)} u_{n\boldsymbol{K}(t)}(\boldsymbol{r}) d\boldsymbol{r}\end{aligned} \tag{A.2}$$

with $m \neq n$.

This could be shown true by starting with $\boldsymbol{K}(t)$ derivative of Eq. 2.20 and the followings:

$$\frac{\partial}{\partial \boldsymbol{K}(t)} [E_{n\boldsymbol{K}(t)} u_{n\boldsymbol{K}(t)}(\boldsymbol{r})] = \frac{\partial}{\partial \boldsymbol{K}(t)} [H^{[\boldsymbol{K}(t)]} u_{n\boldsymbol{K}(t)}(\boldsymbol{r})] \tag{A.3}$$

$$\frac{\partial E_{n\boldsymbol{K}(t)}}{\partial \boldsymbol{K}(t)} u_{n\boldsymbol{K}(t)}(\boldsymbol{r}) + E_{n\boldsymbol{K}(t)} \frac{\partial u_{n\boldsymbol{K}(t)}(\boldsymbol{r})}{\partial \boldsymbol{K}(t)} = \hbar \frac{-i\hbar\nabla + \hbar\boldsymbol{K}(t)}{M} u_{n\boldsymbol{K}(t)}(\boldsymbol{r}) + H^{[\boldsymbol{K}(t)]} \frac{\partial u_{n\boldsymbol{K}(t)}(\boldsymbol{r})}{\partial \boldsymbol{K}(t)}. \tag{A.4}$$

Then we multiple $u_{m\boldsymbol{K}(t)}\boldsymbol{r}$ on both sides and integrate over one cell in real space:

$$\begin{aligned}&\frac{\partial E_{n\boldsymbol{K}(t)}}{\partial \boldsymbol{K}(t)}\frac{1}{\Omega_C}\int_{\Omega_C} u^*_{m\boldsymbol{K}(t)}(\boldsymbol{r})u_{n\boldsymbol{K}(t)}(\boldsymbol{r})d\boldsymbol{r}+\frac{E_{n\boldsymbol{K}(t)}}{\Omega_C}\int_{\Omega_C} u^*_{m\boldsymbol{K}(t)}(\boldsymbol{r})\frac{\partial u_{n\boldsymbol{K}(t)}(\boldsymbol{r})}{\partial \boldsymbol{K}(t)}d\boldsymbol{r}\\
&=\frac{\hbar}{\Omega_C}\int_{\Omega_C} u^*_{m\boldsymbol{K}(t)}(\boldsymbol{r})\frac{-i\hbar\nabla+\hbar\boldsymbol{K}(t)}{M}u_{n\boldsymbol{K}(t)}(\boldsymbol{r})d\boldsymbol{r}+\frac{1}{\Omega_C}\int_{\Omega_C} u^*_{m\boldsymbol{K}(t)}(\boldsymbol{r})H^{[\boldsymbol{K}(t)]}\frac{\partial u_{n\boldsymbol{K}(t)}(\boldsymbol{r})}{\partial \boldsymbol{K}(t)}d\boldsymbol{r}\\
&=\frac{\hbar}{\Omega_C}\int_{\Omega_C} u^*_{m\boldsymbol{K}(t)}(\boldsymbol{r})\frac{-i\hbar\nabla}{M}u_{n\boldsymbol{K}(t)}(\boldsymbol{r})d\boldsymbol{r}+\frac{\hbar^2\boldsymbol{K}(t)}{M}\frac{1}{\Omega_C}\int_{\Omega_C} u^*_{m\boldsymbol{K}(t)}(\boldsymbol{r})u_{n\boldsymbol{K}(t)}(\boldsymbol{r})d\boldsymbol{r}+\\
&\qquad\frac{E_{m\boldsymbol{K}(t)}}{\Omega_C}\int_{\Omega_C} u^*_{m\boldsymbol{K}(t)}(\boldsymbol{r})\frac{\partial u_{n\boldsymbol{K}(t)}(\boldsymbol{r})}{\partial \boldsymbol{K}(t)}d\boldsymbol{r}.\end{aligned}\tag{A.5}$$

Note that

$$\frac{1}{\Omega_C}\int_{\Omega_C} u^*_{m\boldsymbol{K}(t)}(\boldsymbol{r})u_{n\boldsymbol{K}(t)}(\boldsymbol{r})d\boldsymbol{r}=\delta_{mn}$$

so we simply have:

$$\begin{aligned}&\delta_{mn}\frac{\partial E_{n\boldsymbol{K}(t)}}{\partial \boldsymbol{K}(t)}+\frac{E_{n\boldsymbol{K}(t)}}{\Omega_C}\int_{\Omega_C} u^*_{m\boldsymbol{K}(t)}(\boldsymbol{r})\frac{\partial u_{n\boldsymbol{K}(t)}(\boldsymbol{r})}{\partial \boldsymbol{K}(t)}d\boldsymbol{r}\\
&=\frac{\hbar}{\Omega_C}\int_{\Omega_C} u^*_{m\boldsymbol{K}(t)}(\boldsymbol{r})\frac{-i\hbar\nabla}{M}u_{n\boldsymbol{K}(t)}(\boldsymbol{r})d\boldsymbol{r}+\delta_{mn}\frac{\hbar^2\boldsymbol{K}(t)}{M}+\frac{E_{m\boldsymbol{K}(t)}}{\Omega_C}\int_{\Omega_C} u^*_{m\boldsymbol{K}(t)}(\boldsymbol{r})\frac{\partial u_{n\boldsymbol{K}(t)}(\boldsymbol{r})}{\partial \boldsymbol{K}(t)}d\boldsymbol{r}.\end{aligned}\tag{A.6}$$

By collect similar terms, Eq. A.2 is retained.

Bibliography

[1] A. Baltuška et al. “Attosecond control of electronic processes by intense light fields”. en. In: *Nature* 421.6923 (Feb. 2003). Number: 6923 Publisher: Nature Publishing Group, pp. 611–615. ISSN: 1476-4687. DOI: 10.1038/nature01414. URL: https://www.nature.com/articles/nature01414 (visited on 01/08/2021).

[2] J. Itatani et al. “Tomographic imaging of molecular orbitals”. en. In: *Nature* 432.7019 (Dec. 2004). Number: 7019 Publisher: Nature Publishing Group, pp. 867–871. ISSN: 1476-4687. DOI: 10.1038/nature03183. URL: https://www.nature.com/articles/nature03183 (visited on 01/08/2021).

[3] Eleftherios Goulielmakis et al. “Real-time observation of valence electron motion”. en. In: *Nature* 466.7307 (Aug. 2010). Number: 7307 Publisher: Nature Publishing Group, pp. 739–743. ISSN: 1476-4687. DOI: 10.1038/nature09212. URL: https://www.nature.com/articles/nature09212 (visited on 01/08/2021).

[4] G. Vampa et al. “Theoretical Analysis of High-Harmonic Generation in Solids”. In: *Phys. Rev. Lett.* 113 (7 Aug. 2014), p. 073901. DOI: 10.1103/PhysRevLett.113.073901. URL: https://link.aps.org/doi/10.1103/PhysRevLett.113.073901.

[5] G. Vampa et al. “Semiclassical analysis of high harmonic generation in bulk crystals”. In: *Phys. Rev. B* 91 (6 Feb. 2015), p. 064302. DOI: 10.1103/PhysRevB.91.064302. URL: https://link.aps.org/doi/10.1103/PhysRevB.91.064302.

[6] Chang-Ming Wang et al. “Role of electron scattering on the high-order harmonic generation from solids”. In: *Phys. Rev. Research* 2 (3 Aug. 2020), p. 033333. DOI: 10.1103/PhysRevResearch.2.033333. URL: https://link.aps.org/doi/10.1103/PhysRevResearch.2.033333.

[7] Takuya Ikemachi et al. “Trajectory analysis of high-order-harmonic generation from periodic crystals”. In: *Phys. Rev. A* 95 (4 Apr. 2017), p. 043416. DOI: 10.1103/PhysRevA.95.043416. URL: https://link.aps.org/doi/10.1103/PhysRevA.95.043416.

[8] Bob Nagler et al. “Turning solid aluminium transparent by intense soft X-ray photoionization”. In: *Nature Physics* 5.9 (2009), p. 693.

[9] Theodore H Maiman. “Stimulated optical radiation in ruby”. In: *nature* 187.4736 (1960), pp. 493–494.

[10] Theodore H Maiman. “Stimulated optical emission in fluorescent solids. I. Theoretical considerations”. In: *Physical Review* 123.4 (1961), p. 1145.

[11] M Ferray et al. “Multiple-harmonic conversion of 1064 nm radiation in rare gases”. In: *Journal of Physics B: Atomic, Molecular and Optical Physics* 21.3 (Feb. 1988), pp. L31–L35. DOI: 10.1088/0953-4075/21/3/001. URL: https://doi.org/10.1088/0953-4075/21/3/001.

[12] P. B. Corkum. “Plasma perspective on strong field multiphoton ionization”. In: *Physical Review Letters* 71.13 (Sept. 1993). Publisher: American Physical Society, pp. 1994–1997. DOI: 10.1103/PhysRevLett.71.1994. URL: https://link.aps.org/doi/10.1103/PhysRevLett.71.1994 (visited on 03/28/2020).

[13] M. Lewenstein et al. “Theory of high-harmonic generation by low-frequency laser fields”. en. In: *Physical Review A* 49.3 (Mar. 1994), pp. 2117–2132. ISSN: 1050-2947, 1094-1622. DOI: 10.1103/PhysRevA.49.2117. URL: https://link.aps.org/doi/10.1103/PhysRevA.49.2117 (visited on 12/21/2019).

[14] G. Steinmeyer et al. “Frontiers in Ultrashort Pulse Generation: Pushing the Limits in Linear and Nonlinear Optics”. en. In: *Science* 286.5444 (Nov. 1999). Publisher: American Association for the Advancement of Science Section: Special Reviews, pp. 1507–1512. ISSN: 0036-8075, 1095-9203. DOI: 10.1126/science.286.5444.1507. URL: https://science.sciencemag.org/content/286/5444/1507 (visited on 01/13/2021).

[15] Thomas Brabec and Ferenc Krausz. “Intense few-cycle laser fields: Frontiers of nonlinear optics”. In: *Rev. Mod. Phys.* 72 (2 2000), pp. 545–591. DOI: 10.1103/RevModPhys.72.545. URL: https://link.aps.org/doi/10.1103/RevModPhys.72.545.

[16] Ferenc Krausz and Misha Ivanov. “Attosecond physics”. In: *Rev. Mod. Phys.* 81 (1 2009), pp. 163–234. DOI: 10.1103/RevModPhys.81.163. URL: https://link.aps.org/doi/10.1103/RevModPhys.81.163.

[17] Thomas Gaumnitz et al. “Streaking of 43-attosecond soft-X-ray pulses generated by a passively CEP-stable mid-infrared driver”. In: *Opt. Express* 25.22 (2017), pp. 27506–27518. DOI: 10.1364/OE.25.027506. URL: http://www.opticsexpress.org/abstract.cfm?URI=oe-25-22-27506.

[18] M. Uiberacker et al. “Attosecond real-time observation of electron tunnelling in atoms”. en. In: *Nature* 446.7136 (Apr. 2007). Number: 7136 Publisher: Nature Publishing Group, pp. 627–632. ISSN: 1476-4687. DOI: 10.1038/nature05648. URL: https://www.nature.com/articles/nature05648 (visited on 01/14/2021).

[19] Shambhu Ghimire et al. “Observation of high-order harmonic generation in a bulk crystal”. In: *Nature physics* 7.2 (2011), pp. 138–141.

[20] Shambhu Ghimire and David A Reis. “High-harmonic generation from solids”. In: *Nature Physics* 15.1 (2019), pp. 10–16.

[21] T. T. Luu et al. “Extreme ultraviolet high-harmonic spectroscopy of solids”. en. In: *Nature* 521.7553 (May 2015). Number: 7553 Publisher: Nature Publishing Group, pp. 498–502. ISSN: 1476-4687. DOI: 10.1038/nature14456. URL: https://www.nature.com/articles/nature14456 (visited on 03/31/2020).

[22] G. Vampa and T. Brabec. “Merge of high harmonic generation from gases and solids and its implications for attosecond science”. en. In: *Journal of Physics B: Atomic, Molecular and Optical Physics* 50.8 (Mar. 2017). Publisher: IOP Publishing, p. 083001. ISSN: 0953-4075. DOI: 10.1088/1361-6455/aa528d. URL: https://doi.org/10.1088%2F1361-6455%2Faa528d (visited on 03/28/2020).

[23] Mengxi Wu et al. “High-harmonic generation from Bloch electrons in solids”. In: *Phys. Rev. A* 91 (4 Apr. 2015), p. 043839. DOI: 10.1103/PhysRevA.91.043839. URL: https://link.aps.org/doi/10.1103/PhysRevA.91.043839.

[24] Mengxi Wu et al. “Multilevel perspective on high-order harmonic generation in solids”. In: *Phys. Rev. A* 94 (6 Dec. 2016), p. 063403. DOI: 10.1103/PhysRevA.94.063403. URL: https://link.aps.org/doi/10.1103/PhysRevA.94.063403.

[25] C. R. McDonald et al. “Interband Bloch oscillation mechanism for high-harmonic generation in semiconductor crystals”. In: *Physical Review A* 92.3 (Sept. 2015). Publisher: American Physical Society, p. 033845. DOI: 10.1103/PhysRevA.92.033845. URL: https://link.aps.org/doi/10.1103/PhysRevA.92.033845 (visited on 03/31/2020).

[26] Georges Ndabashimiye et al. “Solid-state harmonics beyond the atomic limit”. In: *Nature* 534.7608 (2016), pp. 520–523.

[27] Matthias Hohenleutner et al. “Real-time observation of interfering crystal electrons in high-harmonic generation”. In: *Nature* 523.7562 (2015), pp. 572–575.

[28] D. Golde, T. Meier, and S. W. Koch. “High harmonics generated in semiconductor nanostructures by the coupled dynamics of optical inter- and intraband excitations”. In: *Phys. Rev. B* 77 (7 2008), p. 075330. DOI: 10.1103/PhysRevB.77.075330. URL: https://link.aps.org/doi/10.1103/PhysRevB.77.075330.

[29] Daniel Golde et al. “Microscopic theory of the extremely nonlinear terahertz response of semiconductors”. In: *physica status solidi (b)* 248.4 (2011), pp. 863–866. DOI: https://doi.org/10.1002/pssb.201000840. eprint: https://onlinelibrary.wiley.com/doi/pdf/10.1002/pssb.201000840. URL: https://onlinelibrary.wiley.com/doi/abs/10.1002/pssb.201000840.

[30] Olaf Schubert et al. “Sub-cycle control of terahertz high-harmonic generation by dynamical Bloch oscillations”. In: *Nature photonics* 8.2 (2014), pp. 119–123.

[31] G Vampa et al. “Linking high harmonics from gases and solids”. In: *Nature* 522.7557 (2015), pp. 462–464.

[32] Guangjiu Zhao et al. “Attosecond pulse generation by applying a weak static electric field to a few-cycle pulse”. In: *New Journal of Physics* 13.9 (2011), p. 093035. DOI: 10.1088/1367-2630/13/9/093035. URL: https://doi.org/10.1088/1367-2630/13/9/093035.

[33] Carles Serrat and Jens Biegert. “All-Regions Tunable High Harmonic Enhancement by a Periodic Static Electric Field”. In: *Phys. Rev. Lett.* 104 (7 2010), p. 073901. DOI: 10.1103/PhysRevLett.104.073901. URL: https://link.aps.org/doi/10.1103/PhysRevLett.104.073901.

[34] . “High-order harmonic generation in the presence of a static electric field”. In: *Phys. Rev. A* 72 (3 2005), p. 033407. DOI: 10.1103/PhysRevA.72.033407. URL: https://link.aps.org/doi/10.1103/PhysRevA.72.033407.

[35] Bingbing Wang, Xiaofeng Li, and Panming Fu. “The effects of a static electric field on high-order harmonic generation”. In: *Journal of Physics B: Atomic, Molecular and Optical Physics* 31.9 (3 1998), pp. 1961–1972. DOI: 10.1088/0953-4075/31/9/012. URL: https://doi.org/10.1088/0953-4075/31/9/012.

[36] Bogdan Borca et al. “Static-Electric-Field-Induced Polarization Effects in Harmonic Generation”. In: *Phys. Rev. Lett.* 85 (4 2000), pp. 732–735. DOI: 10.1103/PhysRevLett.85.732. URL: https://link.aps.org/doi/10.1103/PhysRevLett.85.732.

[37] Shunsuke A. Sato et al. “Role of intraband transitions in photocarrier generation”. In: *Phys. Rev. B* 98 (3 2018), p. 035202. DOI: 10.1103/PhysRevB.98.035202. URL: https://link.aps.org/doi/10.1103/PhysRevB.98.035202.

[38] T. Pfeifer, C. Spielmann, and G. Gerber. “Femtosecond x-ray science”. en. In: *Reports on Progress in Physics* 69.2 (3 Jan. 2006). Publisher: IOP Publishing, pp. 443–505. ISSN: 0034-4885. DOI: 10.1088/0034-4885/69/2/R04. URL: https://doi.org/10.1088%2F0034-4885%2F69%2F2%2Fr04 (visited on 03/28/2020).

[39] Erich Runge and E. K. U. Gross. “Density-Functional Theory for Time-Dependent Systems”. In: *Phys. Rev. Lett.* 52 (12 1984), pp. 997–1000. DOI: 10.1103/PhysRevLett.52.997. URL: https://link.aps.org/doi/10.1103/PhysRevLett.52.997.

[40] Nicolas Tancogne-Dejean et al. “Impact of the Electronic Band Structure in High-Harmonic Generation Spectra of Solids”. In: *Phys. Rev. Lett.* 118 (8 2017), p. 087403. DOI: 10.1103/PhysRevLett.118.087403. URL: https://link.aps.org/doi/10.1103/PhysRevLett.118.087403.

[41] J. B. Krieger and G. J. Iafrate. “Time evolution of Bloch electrons in a homogeneous electric field”. In: *Physical Review B* 33.8 (3 Apr. 1986), pp. 5494–5500. DOI: 10.1103/PhysRevB.33.5494. URL: https://link.aps.org/doi/10.1103/PhysRevB.33.5494 (visited on 12/21/2019).

[42] E.O. Kane. “Zener tunneling in semiconductors”. In: *Journal of Physics and Chemistry of Solids* 12.2 (3 1960), pp. 181–188. ISSN: 0022-3697. DOI: https://doi.org/10.1016/0022-3697(60)90035-4. URL: https://www.sciencedirect.com/science/article/pii/0022369760900354.

[44] Primoz Ribic and G. Margaritondo. "Status and prospects of X-ray free-electron lasers (X-FELs): a simple presentation". In: *Journal of Physics D-applied Physics - J PHYS-D-APPL PHYS* 45 (3 May 2012), p. 033407. DOI: 10.1088/0022-3727/45/21/213001. URL: https://link.aps.org/doi/10.1103/PhysRevA.72.033407.

[45] Iwao Matsuda and Yuya Kubota. "Recent Progress in Spectroscopies Using Soft X-ray Free-electron Lasers". In: *Chemistry Letters* 50.7 (3 July 2021). Publisher: The Chemical Society of Japan, pp. 1336–1344. ISSN: 0366-7022. DOI: 10.1246/cl.200881. URL: https://www.journal.csj.jp/doi/full/10.1246/cl.200881 (visited on 07/05/2021).

[46] W. Ackermann et al. "Operation of a free-electron laser from the extreme ultraviolet to the water window". en. In: *Nature Photonics* 1.6 (3 June 2007). Bandiera_abtest: a Cg_type: Nature Research Journals Number: 6 Primary_atype: Research Publisher: Nature Publishing Group, pp. 336–342. ISSN: 1749-4893. DOI: 10.1038/nphoton.2007.76. URL: https://www.nature.com/articles/nphoton.2007.76 (visited on 07/05/2021).

[47] E. Allaria et al. "Tunability experiments at the FERMI@Elettra free-electron laser". en. In: *New Journal of Physics* 14.11 (3 Nov. 2012). Publisher: IOP Publishing, p. 113009. ISSN: 1367-2630. DOI: 10.1088/1367-2630/14/11/113009. URL: https://doi.org/10.1088/1367-2630/14/11/113009 (visited on 07/05/2021).

[48] Tetsuya Ishikawa et al. "A compact X-ray free-electron laser emitting in the sub-ångström region". en. In: *Nature Photonics* 6.8 (3 Aug. 2012). Bandiera_abtest: a Cg_type: Nature Research Journals Number: 8 Primary_atype: Research Publisher: Nature Publishing Group Subject_term: Free-electron lasers;X-rays Subject_term_id: free-electron-lasers;x-rays, pp. 540–544. ISSN: 1749-4893. DOI: 10.1038/nphoton.2012.141. URL: https://www.nature.com/articles/nphoton.2012.141 (visited on 07/05/2021).

[49] P. Emma et al. "First lasing and operation of an ångstrom-wavelength free-electron laser". en. In: *Nature Photonics* 4.9 (3 Sept. 2010). Bandiera_abtest: a Cg_type: Nature Research Journals Number: 9 Primary_atype: Research Publisher: Nature Publishing Group Subject_term: Free-electron lasers;X-rays Subject_term_id: free-electron-lasers;x-rays, pp. 641–647. ISSN: 1749-4893. DOI: 10.1038/nphoton.2010.176. URL: https://www.nature.com/articles/nphoton.2010.176 (visited on 07/05/2021).

[50] Sharon Shwartz et al. "X-Ray Second Harmonic Generation". In: *Physical review letters* 112 (3 Apr. 2014), p. 163901. DOI: 10.1103/PhysRevLett.112.163901. URL: https://link.aps.org/doi/10.1103/PhysRevA.72.033407.

[51] R. K. Lam et al. "Soft X-Ray Second Harmonic Generation as an Interfacial Probe". In: *Physical Review Letters* 120.2 (3 Jan. 2018). Publisher: American Physical Society, p. 023901. DOI: 10.1103/PhysRevLett.120.023901. URL:

https://link.aps.org/doi/10.1103/PhysRevLett.120.023901 (visited on 07/05/2021).

[52] Sh. Yamamoto et al. "Element Selectivity in Second-Harmonic Generation of ${\mathrm{GaFeO}}_{3}$ by a Soft-X-Ray Free-Electron Laser". In: *Physical Review Letters* 120.22 (3 June 2018). Publisher: American Physical Society, p. 223902. DOI: 10.1103/PhysRevLett.120.223902. URL: https://link.aps.org/doi/10.1103/PhysRevLett.120.223902 (visited on 07/05/2021).

[53] Keisuke Hatada and Andrea Di Cicco. "Modeling saturable absorption for ultra short X-ray pulses". In: *Journal of Electron Spectroscopy and Related Phenomena* 196 (3 2014). Advances in Vacuum Ultraviolet and X-ray Physics, The 38th International Conference on Vacuum Ultraviolet and X-ray Physics (VUVX2013), University of Science and Technology of China, pp. 177–180. ISSN: 0368-2048. DOI: https://doi.org/10.1016/j.elspec.2014.02.012. URL: https://www.sciencedirect.com/science/article/pii/S0368204814000656.

[54] P. A. M. Dirac. "Note on Exchange Phenomena in the Thomas Atom". In: *Mathematical Proceedings of the Cambridge Philosophical Society* 26.3 (3 1930), 376–385. DOI: 10.1017/S0305004100016108. URL: https://link.aps.org/doi/10.1103/PhysRevA.72.033407.

[55] J. P. Perdew and Alex Zunger. "Self-interaction correction to density-functional approximations for many-electron systems". In: *Phys. Rev. B* 23 (10 1981), pp. 5048–5079. DOI: 10.1103/PhysRevB.23.5048. URL: https://link.aps.org/doi/10.1103/PhysRevB.23.5048.

[56] Nicolas Tancogne-Dejean et al. "Octopus, a computational framework for exploring light-driven phenomena and quantum dynamics in extended and finite systems". In: *The Journal of chemical physics* 152.12 (3 2020), p. 124119. DOI: 10.1103/PhysRevA.72.033407. URL: https://link.aps.org/doi/10.1103/PhysRevA.72.033407.

[57] K. Yabana et al. "Real-time, real-space implementation of the linear response time-dependent density-functional theory". In: *physica status solidi (b)* 243.5 (3 2006), pp. 1121–1138. DOI: https://doi.org/10.1002/pssb.200642005. eprint: https://onlinelibrary.wiley.com/doi/pdf/10.1002/pssb.200642005. URL: https://onlinelibrary.wiley.com/doi/abs/10.1002/pssb.200642005.

[58] Christian Gähwiller and Frederick C. Brown. "Photoabsorption near the $L_{\mathrm{II,III}}$ Edge of Silicon and Aluminum". In: *Phys. Rev. B* 2 (6 1970), pp. 1918–1925. DOI: 10.1103/PhysRevB.2.1918. URL: https://link.aps.org/doi/10.1103/PhysRevB.2.1918.

Code References

[43] Shunsuke Sato. *Parabolic two-band model Analyzer for Nonlinear electron Dynamics in Attosecond phenomena (PANDA)*. URL: `https://github.com/shunsuke-sato/two_band_model/tree/dev_static_field_draco`.

[59] Chang Ming Wang. *Semi-classical model with Umklapp scattering for high-order harmonic generation in solids*. URL: `https://gitlab.com/wcmphysics/trajectoryanalysissolid/-/tree/release`.

Acknowledgments

This thesis and my PhD would not be possible without the great help from many people.

First of all, not enough of my appreciation could be made to Prof. Dr. Angel Rubio's supervision and patience over the time of my PhD. His passion for research and kindness in dealing with people inspire me not only in the aspect of scientific research but also in the way of life. I must also thank him for his great assistance in the final year when writing my thesis.

Then, I would also like to express my appreciation to Prof. Dr. Nina Rohringer for her co-supervision in this PhD program.

In addition, I would like to thank Prof. Dr. Shunsuke Sato for his tremendous guidance and close supervision. His incredible physical intuition always amazes me, and many ideas in this thesis are built upon his impressive physical instinct. The publication of our paper and my thesis would be impossible without his great help. Also, I am very grateful for his immeasurable patience during the supervision. In times I struggled with the scientific goals we set up, his patient waiting and reminders kept me pushing forward to the finish line of my PhD.

Many of my thanks should be said to Dr. Massimo Altarelli for his fruitful discussion and suggestions in the project of X-ray absorption. The open and welcome atmosphere formed around him steady my nerve during the hard time studying the subject.

I must express my gratitude to Dr. Nicolas Tancogne-Dejean for his close supervision during the project of X-ray absorption. His infinite energy and passion for research also have a huge influence on me.

I acknowledge the great help from Prof. Dr. Kazuhiro Yabana and many insightful discussions with him. One of many great memories during the PhD would not be there without Guillaume who has traveled a lot with me in Germany. Also, I enjoy the relaxing discussions with my office mate Henning not only in the knowledge

about computer hardware but also the politics and culture of Germany. Together with many other friends, I want to say thanks to you all.

Most importantly, I would like to thank my family for their great support during the years of my PhD. I simply cannot imagine how more difficult my PhD would have been without their caring and love.

Declaration on Oath

Hiermit erkläre ich an Eides statt, dass ich die vorliegende Dissertationsschrift selbst verfasst und keine anderen als die angegebenen Quellen und Hilfsmittel benutzt habe.

I hereby declare, on oath, that I have written the present dissertation by my own and have not used other than the acknowledged resources and aids.

Hamburg, 9th August, 2021

Chang-Ming Wang

Unterschrift — Signature